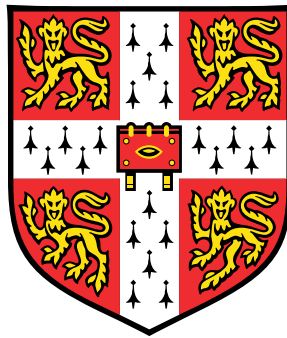


# Space filling by growing sheets

A new approach to the structure of cement's abundant hydration product



**Merlin Aragon Etzold**

Department of Chemical Engineering  
BP-Institute for Multiphase Flow  
University of Cambridge

This dissertation is submitted for the degree of  
*Doctor of Philosophy*

Darwin College

February 2015



I would like to dedicate this thesis to my family, who have been very supportive during the past 3.5 years.



## **Declaration**

I hereby declare that except where specific reference is made to the work of others, the contents of this dissertation are original and have not been submitted in whole or in part for consideration for any other degree or qualification in this, or any other university. This dissertation is my own work and contains nothing which is the outcome of work done in collaboration with others, except as specified in the text and Acknowledgements. This dissertation contains fewer than 65,000 words including appendices, bibliography, footnotes, tables and equations and has fewer than 150 figures.

Merlin Aragon Etzold  
February 2015



## Acknowledgements

I would like to thank the European Commission via the Marie-Curie program to fund the TRANSCEND project and for generous support. The research leading to these results has received funding from the European Union Seventh Framework Programme (FP7 / 2007-2013) under grant agreement 264448.

I would like to thank the following individuals and groups for their support during my Ph.D.

1. My supervisor Alex Routh. Thank you for giving me this opportunity, your patience and generosity, and for your ongoing faith in my abilities to complete this work despite my own doubts.
2. Peter McDonald for suggesting to work on the sheet model, his advice in applying it to cement, and for suggesting to see the sheet model as a group of models.
3. Ellis Gartner for the discussions about the sheet model and a few other things.
4. Dave Faux for advice in finding an efficient kinetic Monte Carlo algorithm.
5. Sergey Churakov for hosting me for two weeks in the Paul-Scheerer institute and teaching me how to use MPI. My gratitude goes also to his group for making me feel very welcome, particularly Luis Pegado.
6. Timo Michelsen for his advice regarding the software development aspects of the sheet growth algorithm.
7. Robert Farr for pointing out that my base growth model is actually an Eden process.
8. The BPI-Crowd and -Staff for providing a good working environment.
9. The students being involved in the C-S-H student workshop.
10. The students of the TRANSCEND-network and their supervisors.

11. Those people who I asked for advice and proof reading of the earlier versions of this thesis, who are:
  - Mary Wood
  - Felicity Bartholomew
  - Caren Otto
  - Agata Gajewicz
  - Becky Welbourn
  - Thomas Bohne
  - Wei Jin Gun
  - Arnaud Muller
  - Jade Rolph
12. My friends in Cambridge, who have always laughed with me, listened when necessary, offered a shoulder to cry on, and treated me with food if the two other approaches failed. Soon this document will be submitted, and I will be back!
13. Jade Rolph for being (a) great (girl-friend), particularly during the three month preceding the submission of this thesis.
14. My parents for just being great and always being supportive during the last 3.5 years.

## Abstract

In this thesis, different model structures for the meso-structure (between 1 and 100 nm) of calcium-silicate-hydrate (C–S–H) in cement paste are discussed. C–S–H is the most important solid phase of Portland cement concrete, which is by mass the most-produced artificial material worldwide. The meso-structure of C–S–H has paramount influence, controlling many technical properties of concrete.

The meso-structure of C–S–H in cement is the subject of a long-standing debate, which is reviewed in this thesis. Two different views exist in the cement community: the first view describes the meso-structure of C–S–H as an aggregate of colloidal particles of diameter 5 nm. The second proposes C–S–H, on this length scale, as a continuous but highly disordered sheet structure. The idea of a colloidal aggregate is more popular and considerable efforts have been spent on modelling it. The idea of a sheet structure has been widely discussed but never investigated as a numerical model.

In this thesis, the particle view is investigated from the perspective of transport through such structures. The idea of a colloidal model has been rationalised as a dense random spherocylinder packing, with particles of diameter 5 nm. The aspect ratio of these particles has been used to tune the solid volume fraction. The transport properties of the structures were characterised using lattice Boltzmann schemes for permeability and diffusivity. This assumes macroscopic fluid dynamics within the pores. The results show that the use of random particle packings as structural models can not explain the low transport properties attributed to C–S–H.

Subsequently, the sheet model was investigated. A fundamental study of space filling by growing sheets was conducted, focussing on the growth kinetics. A new numerical platform able to describe three-dimensional sheet structures was developed. The evolution of time is described by a kinetic Monte-Carlo scheme. A growth model based on the two-dimensional Eden process was used as a base model for the growth of sheets in three-dimensional space. Further growth steps were defined, which can be combined with sheet growth into a variety of growth models. These steps allow the growing sheets to sample three-dimensional space, forming layered structures, and also permit a change of the growth direction of the sheet. The growth kinetics of these models were studied and the resultant structures visualised.

Some of these models and their resultant structures are potential structures for the meso-structure of C–S–H.

Based on the sheet growth algorithm, a numerical model was developed to describe the formation of C–S–H in hydrating cement paste. Sheets were grown by making assumptions used for the model as realistic to the cement system as possible. It is also shown how the properties of the computational sheet structures can be related to experiments on C–S–H and cement paste, namely,  $^1\text{H-NMR}$  (relaxometry), growth kinetics, micrographs, small-angle scattering data and the permeability. The latter was computed using lattice Boltzmann schemes. The simple sheet growth model led to structures whose properties are consistent with a range of such experimental observations made on C–S–H in cement paste, despite issues in explaining the low permeabilities reported. These results make a strong point in favour of the sheet hypotheses for the meso-structure.

## Note on nomenclature

This work is very heavy in nomenclature. This is due to the description of the different numerical methods used in this work. The literature, in which each of these methods is described, has a standard nomenclature for each of the methods used in this work. For example, in the lattice Boltzmann literature,  $\tau$  denotes the relaxation time, and in the literature about kinetic Monte Carlo methods the same symbol denotes the time between two events. The author of this thesis preferred to use a notation consistent with the respective literature, so the meaning of a particular symbol can be context dependent.

The complete list of symbols and abbreviations used can be found at the end of this thesis on page 135.



# Table of contents

<b>Note on nomenclature</b>	<b>xi</b>
<b>Table of contents</b>	<b>xiii</b>
<b>1 Introduction</b>	<b>1</b>
1.1 National economic and environmental impact of cement and concrete . . .	3
1.2 Concrete - a multi-scale material . . . . .	3
1.3 Current research challenges within the field of cementitious materials . . .	4
1.4 Summary . . . . .	5
<b>2 Literature Review</b>	<b>7</b>
2.1 Introduction . . . . .	7
2.2 Portland Cement: the underlying chemistry . . . . .	8
2.3 Cement hydration . . . . .	12
2.3.1 Overview about cement paste . . . . .	12
2.3.2 Time-resolved cement hydration . . . . .	13
2.4 Experimental techniques used to study C–S–H . . . . .	16
2.4.1 Electron microscopy . . . . .	16
2.4.2 Small-angle scattering . . . . .	20
2.4.3 Nuclear magnetic resonance ( <sup>1</sup> H-NMR) . . . . .	22
2.5 Proposed models for the meso-structure of C–S–H . . . . .	23
2.5.1 The Powers-Brownyard model (1940s) . . . . .	23
2.5.2 Wittmann model (1970s) . . . . .	23
2.5.3 The Feldman-Sereda model (1970s) . . . . .	25
2.5.4 The Daimon-Model (1976) . . . . .	26
2.5.5 The Jennings models (2000s) . . . . .	26
2.6 Discussion and Conclusions . . . . .	28

<b>3</b>	<b>Methods</b>	<b>31</b>
3.1	Introduction . . . . .	31
3.2	Kinetic Monte Carlo methods . . . . .	31
3.2.1	Derivation of the Gillespie algorithm . . . . .	32
3.3	Small-angle neutron scattering prediction . . . . .	34
3.3.1	The Schmidt-Rohr scheme for scattering curve prediction . . . . .	36
3.4	Characterisation of transport properties of random structures . . . . .	37
3.4.1	Lattice Boltzmann . . . . .	38
3.4.2	Lattice Boltzmann for the Navier-Stokes equations . . . . .	40
3.4.3	Lattice Boltzmann diffusivity scheme . . . . .	43
3.4.4	Conversion between the lattice and the real world . . . . .	45
3.4.5	Implementation . . . . .	45
3.4.6	Verification . . . . .	45
3.5	Conclusions . . . . .	51
<b>4</b>	<b>Simple particle model for the transport properties of C–S–H</b>	<b>53</b>
4.1	Introduction . . . . .	53
4.1.1	Transport properties of C–S–H in cement paste . . . . .	54
4.1.2	Building a model for the meso-structure of C–S–H . . . . .	56
4.2	Methods . . . . .	59
4.2.1	Spherocylinder packing . . . . .	59
4.2.2	Computation of transport properties . . . . .	64
4.2.3	Scattering curve prediction . . . . .	64
4.3	Results . . . . .	64
4.3.1	Spherocylinder Packings . . . . .	64
4.3.2	Scattering pattern of spherocylinder packings . . . . .	65
4.3.3	Permeability of spherocylinder packings . . . . .	67
4.3.4	Diffusivity of spherocylinder packing . . . . .	68
4.4	Discussion . . . . .	69
4.5	Conclusion . . . . .	70
<b>5</b>	<b>Filling of three-dimensional space by two-dimensional growing sheets</b>	<b>71</b>
5.1	Introduction . . . . .	71
5.2	Background . . . . .	73
5.2.1	The Eden model and its properties . . . . .	73
5.2.2	Models of space filling and anisotropic growth . . . . .	74
5.3	The sheet growth model . . . . .	77

---

5.3.1	Model elements . . . . .	77
5.3.2	Combinations of model elements . . . . .	77
5.3.3	Theory of sheet growth . . . . .	81
5.3.4	How the models are studied . . . . .	85
5.4	Numerics . . . . .	86
5.4.1	Kinetic Monte Carlo scheme . . . . .	86
5.4.2	Implementation details . . . . .	89
5.5	Results . . . . .	90
5.5.1	Single sheet growth . . . . .	90
5.5.2	Growth of a sheet crystal: sheet growth and layering . . . . .	93
5.5.3	Sheet growth and bifurcation . . . . .	94
5.5.4	Space filling by growing sheets with continuous nucleation . . . . .	97
5.5.5	Sheet growth and layering: space filling by sheet crystals . . . . .	101
5.5.6	Space filling by sheet growth with bifurcation . . . . .	107
5.6	Discussion and Conclusion . . . . .	107
<b>6</b>	<b>A sheet model for the meso-structure of calcium-silicate-hydrate in cement</b>	<b>113</b>
6.1	Introduction . . . . .	113
6.2	Application of the sheet growth model to C-S-H . . . . .	116
6.3	Methods . . . . .	118
6.3.1	Pore space characterisation . . . . .	118
6.3.2	Prediction of small-angle scattering curves . . . . .	119
6.4	Results . . . . .	121
6.4.1	Growth morphologies . . . . .	121
6.4.2	Model kinetics . . . . .	122
6.4.3	Model porosity . . . . .	124
6.4.4	Scattering . . . . .	127
6.4.5	Permeability . . . . .	128
6.5	Discussion of the model . . . . .	129
6.6	Conclusion . . . . .	130
<b>7</b>	<b>Conclusions and future work</b>	<b>133</b>
7.1	Conclusion . . . . .	133
7.2	Future work . . . . .	134
	<b>Nomenclature</b>	<b>135</b>

**References**

**145**

# Chapter 1

## Introduction

Concrete is the most-produced artificial material. Including natural materials, concrete is second only to drinking water. Eleven billion tons of concrete were produced in 2007, giving an idea of the unique impact this material has on daily life, the global economy and the environment.

The work presented in this thesis concerns cement. Concrete is a matrix of, ideally, inert aggregates, which are held together by a glue. In most cases, this glue is Portland cement. A brief introduction to concrete is given in Section 1.2.

When cement powder is mixed with water it hardens. Concrete and cement are well-understood from an engineering perspective; more than 150 years of use give extensive experience to draw from. Nevertheless, the physico-chemical details of the hardening of cement and the resultant chemical products have remained the subject of an intense debate among researchers. The importance of resolving the debate has been recognised: "One of the most important, long-standing needs in cement science is a quantitative understanding on the atomic to 100 nm scale and how the structures on this scale control the mechanical, transport and chemical properties of hydrated cement paste." [1]. This thesis contributes to this debate by focussing on the meso-structure of calcium-silicate-hydrate (C–S–H)<sup>1</sup>. The growth of C–S–H within the pore space of freshly placed concrete eventually leads to the hardening of the material.

The study of the meso-structure of C–S–H in hardened cement is difficult for a number of reasons. Cement paste is a highly complex multi-component system, so it is difficult to measure the properties of C–S–H alone. The meso-scale of C–S–H is too small to be easily accessible by electron microscopy, and due to the disorder it is also hard to study by scattering methods.

---

<sup>1</sup>Be aware of cement chemist's shorthand, C–S–H is for calcium oxide - silica - hydrogen oxide (water). More details in Chapter 2.

This thesis is organised as follows: in the remainder of this chapter, the global impact of concrete is discussed in Section 1.1 and a brief introduction into concrete is given in Section 1.2. This thesis started as a project to investigate moisture transport through C–S–H on the meso-scale. The literature review given in Chapter 2 shows that the spatial arrangement of solids on this length scale is a matter of ongoing debate, with two models dominating the discussion. One side is a colloidal model, assuming calcium-silicate-hydrate to be assembled by 5 nm-particles with a layered structure [2–4]. The other side is the sheet model proposed by Feldman-Sereda [5–7], which describes calcium-silicate-hydrate also as a layered structure. The highly disordered layers are extended over a larger length scale. Moisture transport through C–S–H was studied from the colloidal viewpoint. A particle packing with the appropriate particle radii was used as the structural model, and lattice Boltzmann was used to calculate the transport properties of such a structure. The study is reported in Chapter 4, and it turned out that the simple model failed to explain transport properties attributed to C–S–H. At this point, it was understood by the author that the more interesting problem would be the study of the meso-structure of C–S–H itself. Since only a single author, Gartner [8], has proposed concepts of how sheet structures may form, the author changed the focus of the thesis.

A new computer model describing two-dimensional growth was developed and used to study different models for space-filling by growing sheets. The different models were rationalised in a hierarchy of models, which are included in Chapter 5. Before the exploration of sheet growth, the computer model of growing sheets was used to build an initial model of growth of calcium-silicate-hydrate sheets, which is described in Chapter 6. The properties of the resultant sheet structures were calculated and compared against experimental data, obtained for cement paste.

Having been part of the EU-funded TRANSCEND project, the author of this thesis was in the fortunate position to be able to participate in the NANOCEM<sup>2</sup> network, which allowed him to have frequent discussions with other researchers working on cement. In Chapter 7, the results of the thesis are reviewed in the light of these discussions, and some suggestions for further work are elaborated.

---

<sup>2</sup>[www.nanocem.org](http://www.nanocem.org)

## 1.1 National economic and environmental impact of cement and concrete

In 2007, the annual world-wide production of concrete was 11 billion tons [9]. The cement used to make the concrete has the largest environmental footprint of the components in concrete. In order to produce this amount of concrete, approximately 1.7 billion tons of cement was produced in 2004, contributing approximately 5 % to 8 % of mankind's carbon dioxide emission. It is important to note that the specific carbon dioxide emission of concrete is actually low. Its impact is caused by the large quantities produced [1, 10]. More recently, Schneider et al. estimated the global cement production as 2.8 billion tons per year, with some potential to reach 4 billion tons annually [11].

Concrete is the base for most modern building activities. Thus, it contributes directly and indirectly towards the cost of any civil engineering. One can get a feeling for the global economic impact of concrete by considering expenses for infrastructure. In the Western world, a clear need for renewal and renovation of ageing infrastructure has been identified. The United Kingdom spent £41 billion on infrastructure between 2005-2010, and increased this amount to £45 billion in the period 2011-2013. In Germany, approximately 6000 road bridges are flagged for urgent repair or even replacement [12]. Germany's infrastructure spending is comparable to Britain's, allocating approximately € 23.6 billion in the federal budget for 2013 [13]. In the United States, the American Society of Civil Engineers reports considerable need for infrastructure repairs [14]. To meet this demand, the United States are debating the GROW AMERICA Act, a pledge to spend \$302 billion over four years to improve the transport system [15]. In Asia, the need for investment has been estimated as 800 billion dollars annually until 2020 [16].

This short overview highlights an important aspect of cement research: improved materials do not only pay off once during the first building phase, they also decrease the need for repairs and therefore the overall life-cycle cost.

## 1.2 Concrete - a multi-scale material

Reinforced concrete is a complex multi-scale composite. The main length scales are outlined in Figure 1.1. The reinforcement bars are on the largest length scale, with a characteristic length of centimetres and more. Concrete itself is strong in resisting compressive stress, but less so for tensile stress. This is the function of the steel bars. The reinforcement bars are embedded in concrete, which is a matrix of aggregates glued together by cement. The particle size distribution of aggregates, which ranges from centimetres down to less

than a millimetre, is optimised to fill space as effectively as possible. The aggregates are glued together by cement. In the vicinity of the aggregates, the cement matrix is disturbed by the presence of the aggregate. This region is referred to as interfacial transition zone (ITZ) and is of importance for durability [17]. Fresh cement paste can be seen as a loose packing of cement particles with water between them. The cement grains have typical sizes between 1 and 100  $\mu\text{m}$ . As cement hydration proceeds, new products form between the cement grains. The most abundant of these products is calcium-silicate-hydrate (C-S-H). On the meso-scale, the arrangement of matter in space is still a matter of discussion, but a characteristic size of 5 nm can be identified [2, 18].

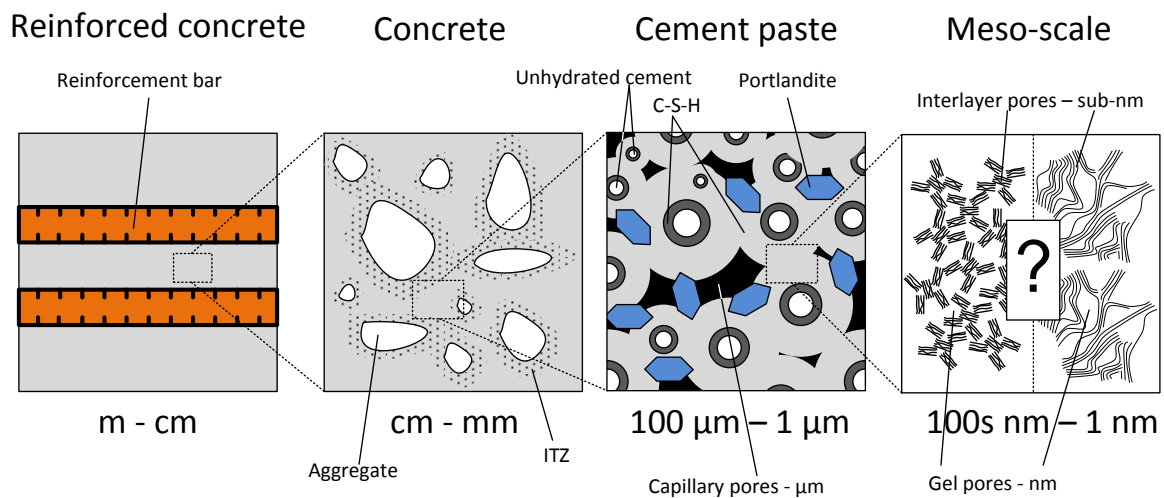


Fig. 1.1 Relevant length scales in concrete. This thesis focusses on the spatial arrangement of solids in the hydration products on the meso scale. Abbreviations: C-S-H: calcium-silicate-hydrates, ITZ: interfacial transition zone. Note that two hypotheses are currently discussed for the arrangement of solids in the meso scale. Inspired by Bernard et al. [19]

This work focusses on the structure of the dominant new product forming between cement grains, the calcium-silicate-hydrate.

### 1.3 Current research challenges within the field of cementitious materials

Scrivener and Kirkpatrick list three major barriers to innovation in concrete technology. These are: (i) the need to *guarantee structural safety*, (ii) the *empirical knowledge base* about the physico-chemical processes and (iii) the need to keep the *cost low* [1]. The second barrier can only be lifted by increasing fundamental research activity.

As part of the general desire to decrease mankind's carbon dioxide emission, it is desirable to reduce the environmental footprint of cementitious materials [20]. This is difficult for two reasons: first, it is generally assumed that process optimisation of cement production has already been maximised, and second, concrete is already a highly efficient and low-carbon dioxide material [1]. Changing the composition of the cement allows one to change the process conditions during cement production, which can lead to considerable energy savings and hence reduced carbon dioxide emission [10, 11]. Low-carbon cements can also be created through increasing the replacement of Portland cement clinker with secondary cementitious materials (SCM) beyond today's typical values.

The empirical knowledge regarding the long-time performance of newly introduced materials is necessarily limited. Civil engineering structures have typical projected lifetimes between 50 years and 150 years. The resultant need to understand the long-term performance of cementitious materials leads to the second important research area in this field, which is to understand the fundamental mechanisms of concrete corrosion. Understanding concrete durability is directly linked to decreasing the carbon dioxide output: in order to predict the lifetime of a new low-CO<sub>2</sub> concrete, fundamental understanding of the mechanisms that deteriorate its performance is needed. All corrosion processes in concrete, such as chloride ingress, alkali silica reaction or carbonatisation, depend on the state of water within the material. Therefore, moisture transport in concrete and cement is of great interest [21].

This project was initially part of an effort to understand moisture transport in concrete. Appreciating that concrete is a multi-scale material, multiple students were assigned in the EU project TRANSCEND<sup>3</sup> to the different length scales. Both modelling as well as complementary experiments were employed; this thesis is the result of one of the modelling projects.

## 1.4 Summary

Concrete is a material of unique importance for mankind with a huge environmental impact. Concrete gains its strength due to the reaction of its most important constituent, cement, with water. The meso-structure of the dominant reaction product, the calcium-silicate-hydrates, is the focus of this thesis.

---

<sup>3</sup>Transport in concrete which is eco-friendly and innovative.



# Chapter 2

## Literature Review

"The more I read the papers, the less I understand."

- *Ira Gershwin*. Taken from [22]. Certainly true for the field of cement.

"Don't raise this question in your thesis".

- Advice given to the author concerning the question whether the meso-structure of C–S–H is best described as a packing of colloidal particles or as a quasi-continuous sheet structure.

The fundamentals of cement chemistry and cement hydration are reviewed. Subsequently, selected experimental findings for calcium-silicate-hydrate (C–S–H) in Portland cement are discussed and the most important models for the meso-structure of C–S–H are introduced. The two dominant models, the disordered sheet structure and the particle aggregate, are discussed and the research decisions made justified.

### 2.1 Introduction

This chapter has two purposes. It should serve as an introduction to the fascinating field of Portland cement based hydraulic binders, aiming at a technical person without any specific previous knowledge. The second, and primary, purpose is to take a detailed look at the meso-structure of the calcium-silicate-hydrates, that is, the structure on a length scale of approximately 1 nm to hundreds of nano metres. The major hypotheses proposed since the late 1940s are reviewed and subsequently critically discussed.

The current "sociological climate in the field"<sup>1</sup> is that two different meso-structure models are discussed. These are essentially those which have been proposed already in the

---

<sup>1</sup>The author of this thesis has to leave the fame for this amazing expression to Mansfield and Klushin [23].

1890s, with provisions to include new results obtained with better experimental techniques. The first colloidal hypotheses for cement was proposed by Michaëlis, and this dominant school of thought proposes the meso-structure to be best described as an aggregation of colloidal particles with a diameter of 5 nm [3, 4]. A second school of thought describes the meso-structure as an extended and disordered sheet structure [5–8], which can probably be seen as a highly disordered version of le Chatelier’s crystallite hypothesis [24]. Both ideas are compared and arguments for and against the two models discussed. This is used to justify the decision to study growing sheet structures.

## 2.2 Portland Cement: the underlying chemistry

Portland cement is mainly produced from the oxides of calcium and silicon. Aluminium oxide and iron oxide are contained within the raw material as well. These oxides are mostly obtained by using limestone and clays as the raw materials for cement production. Depending on local availability, other materials can be used. Furthermore, secondary fuels introduced in the process can provide a contribution to the cement composition, for example calcium from ground bones. The raw materials are fired at up to 1450 °C in a rotary kiln, which is part of the more complex cement plant [25].

The resultant product is called the cement clinker<sup>2</sup> and comprises different constituents, which are called the clinker phases. The most important clinker phases are summarised in Table 2.1 with their abbreviation in cement chemistry notation<sup>3</sup>. The most abundant clinker phases are alite<sup>4</sup> and belite, with alite being the fastest reacting phase and thus responsible for early strength development [24]. Modern cements may contain other substances as well. The standard EN 197-1 also allows the use of latent hydraulic materials such as granulated blast furnace slag, siliceous or calcareous fly ash, silica fume and other materials. These materials are called supplementary cementitious materials (SCM). Since SCM are waste materials from other processes and replace cement clinker, they reduce the environmental foot print of the material.

As the cement powder is mixed with water, the water dissolves the cement grains. New

---

<sup>2</sup>The word clinker has its origin in the time when cement was produced in batches. The feed was inserted into the oven in brick-like pieces, which were also referred to as clinker [26].

<sup>3</sup>Cement chemistry is centred around a few metal oxides, which are commonly written in shorthand as: C - calcium oxide, S - silicon dioxide, H - water, A - aluminium oxide, F - iron oxide, M - magnesium oxide,  $\bar{S}$  sulphur trioxide.

<sup>4</sup>Alite and belite are traditional names used for the two main clinker phases before their chemical composition was known. Today, they are sometimes used to distinguish between synthetic clinker phases of high purity made of reagent grade materials and those being produced in a cement kiln which build many of the other atoms present into their crystal lattice.

Compound	Composition	wt-%
alite (tricalcium silicate)	C <sub>3</sub> S	65
belite (dicalcium silicate)	C <sub>2</sub> S	13
calcium aluminate ferrite	C(A,F)	8
tricalcium aluminate	C <sub>3</sub> A	11
free lime	C	1.2
free magnesium oxide (periklas)	M	1

Table 2.1 Main clinker phases of Portland cement. The given mass fractions are the average values for Portland cements produced in Germany [24].

Reaction	Name
$C_3S + (3 - a + b)H \longrightarrow C_aSH_b\downarrow + (3 - a)CH\downarrow$ $C_2S + (2 - a + b)H \longrightarrow C_aSH_b\downarrow + (2 - a)CH\downarrow$	C–S–H, portlandite (CH)
$C_3A + 3\bar{C}\bar{S} + 32H \longrightarrow C_6A\bar{S}_3H_{32}$ $C_3A + \bar{C}\bar{S} + 12H \longrightarrow C_4A\bar{S}H_{12}$ $C_3A + CH + 18H \longrightarrow C_4AH_{19}$	ettringite tetracalc. monosulfoaluminate hyd. tetra calcium aluminate hydrate
$C_2(A,F) + CH + 3\bar{C}\bar{S} + 31H \longrightarrow C_6(A,F)\bar{S}_3H_{32}$ $C_2(A,F) + CH + \bar{C}\bar{S} + 11H \longrightarrow C_4(A,F)\bar{S}H_{12}$ $C_2(A,F) + 2CH + 17H \longrightarrow 4C(A,F)H_{19}$	aluminate ferrite monosulfate hyd.

Table 2.2 Simplified schematic of reactions and major hydrate phases occurring during the hydration of Portland cement [24].

substances precipitate from the pore solution, called the hydrate phases. A simplified set of reactions describing the reactions of the main clinker phases is shown in Table 2.2. These reactions are not independent from each other. The composition of the products formed is also variable. C–S–H and some of the other phases can incorporate other ions present. The possible reactions of the aluminate phases depend on the availability of sulphate. This is of technical relevance for controlling the initial setting of cement pastes [25].

The minority of the hydrate phases are crystalline and have a defined stoichiometry. The most important hydrate phase is calcium-silicate-hydrate (C–S–H). The notation C<sub>a</sub>SH<sub>b</sub> or C–S–H indicates that it is a non-stoichiometric phase.

The detailed atomic structure of the calcium-silicate-hydrate is still the subject of an intense debate. It is, however, well established that C–S–H is chemically related to the minerals tobermorite and jennite [24, 27]. Tobermorite has a sum formula C<sub>5</sub>S<sub>6</sub>H<sub>8</sub> for the 14 Å-modification. It has a layered structure, which is shown in Figure 2.1 [24, 28].

A single tobermorite crystal consists of layers of calcium oxide. On both sides of these layers, parallel chains of silica tetrahedra are bound. These occur in a dreierketten structure. Two of every three silica tetrahedra are bound to the calcium oxide, whilst every third silica

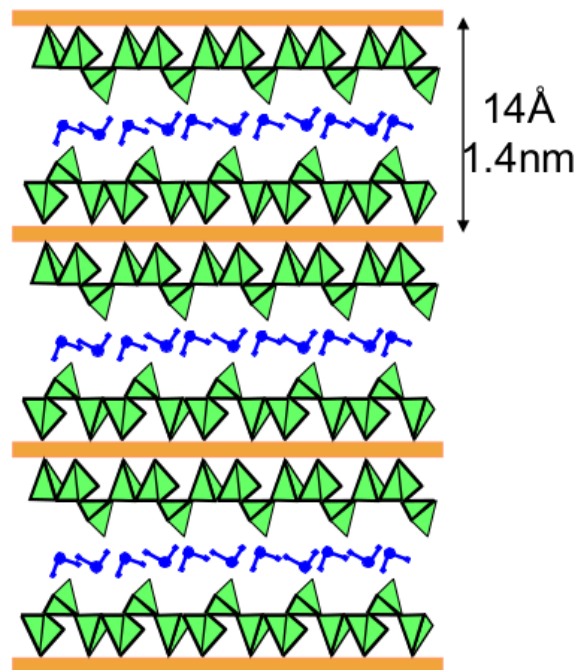


Fig. 2.1 Schematic of the crystal structure of 14 Å-tobermorite. It consists of calcium oxide layers (brown) with a basal spacing of 14 Å. On both sides of the calcium oxide layers, infinite chains of silica tetrahedra (green) are bound. The chains consist of silica dimers, which are connected by a bridging tetrahedron. The water between the layers is the interlayer water [29].

tetrahedron takes a bridging position. The space between the layers contains the interlayer water. The layer spacing of tobermorite can change as a result of heat treatment, which removes some of the interlayer water. 14 Å-, 11.3 Å- and 9.3 Å-modifications were reported [28]. The shape of the crystals reflects the plate-like atomic structure [27].

The calcium-to-silicon ( $Ca/Si$ ) atomic ratio in tobermorite is  $Ca/Si = 0.83$ , whilst the typical  $Ca/Si$  for C–S–H in Portland cement systems approaches  $\sim 1.7$  [27, 30]. The composition of C–S–H may vary within a single sample and over time. SCMs decrease  $Ca/Si$  down to 1.2. Despite its variability, it shows reproducible phase behaviour [29].

Models for the atomic structure of C–S–H are typically based on the tobermorite structure. The calcium-to-silicon ratio can be increased from 0.83 towards 1.7 by substituting bridging silica with protons or assuming the presence of extra calcium ions in the interlayer space. A well known example for such a model is the Richardson-Groves model [27, 31, 32]. Pellenq et al. employed atomistic modelling techniques to study a C–S–H-like

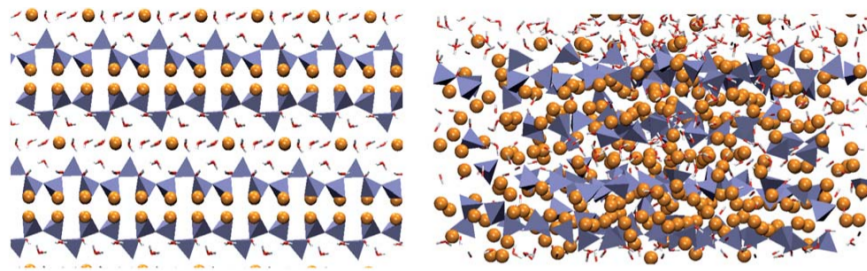


Fig. 2.2 Contrasting drawing of the atom positions in tobermorite (left) and glassy C–S–H (right). Note the short-range disorder in the glassy C–S–H, which still retains some elements of the layered structure. Reproduced with permission from [33].

structure with a calcium-to-silicon ratio of 1.7. The resultant structure is called glassy and shown in Figure 2.2. Glassy C–S–H is highly disordered on a short range, but still some features of crystalline tobermorite, such as the layered structure [34]. The work was strongly criticised by Richardson for ignoring elementary geometrical considerations [35].

Despite the ongoing debate about the details, there seems to be general agreement about the atomic structure [29]. Most of the models for the meso-structure of C–S–H in hydrated cement paste discussed below assume the existence of a tobermorite-like sheet structure.

For the sake of completeness, it is mentioned that the source of cohesion in cement paste is an important research topic on its own right. Gmira et al. identify two different types of forces relevant for cement paste. A short-range attractive force with significant iono-covalent contribution bridges the interlayer space (sub nm). Ionic correlation forces, with a range of a few nanometers, act over a longer distance and involve bound and mobile

calcium ions. Such ions are present in the water-filled spaces [36].

## 2.3 Cement hydration

Cement sets and hardens after mixing with water. Typical cement pastes contain water and cement in a weight ratio,  $w/c$ , of 0.4 to 0.8 by weight [24]. In comparison, standard testing for mortars<sup>5</sup> according to EN 196-1 is carried out at  $w/c = 0.5$ .

In this section, the focus lies on the hydration of alite paste. This is a common model system used to study the fundamentals of the hydration reaction [22, 37, 38].

### 2.3.1 Overview about cement paste

Anhydrous cement has an approximate bulk density of  $3.15 \text{ g cm}^{-3}$ . This means that at a water-to-cement ratio of 0.4, the volume fraction of water is approximately 56 %. The particle sizes of the cement grains are between 1 and  $100 \mu\text{m}$ . When cement paste, the mixture of water and anhydrous cement, is placed in a mould, it settles as a loose packing of particles. The water-filled interstitial space between the cement grains are the so-called capillary pores. The initial situation is sketched in Figure 2.3-left.

When the water reacts with the cement paste, the reaction products precipitate first within the capillary pore space as shown schematically in Figure 2.3-right. For the alite system, these are the amorphous C–S–H phases growing from the surface of the cement grains [39], and bulky crystalline Portlandite crystals growing in the pore space. The C–S–H growing during the early phases is identified by electron microscopists as the outer product (op). Later, growth of a second, much denser, morphology of C–S–H is observed at the location of the former cement grain, which is referred to as inner product C–S–H (ip).

It is important to note at this point that in uncracked cement paste, three water environments are identified in current views on cement paste:

1. The *capillary pores* with sizes in the order of micrometres are located between the cement grains and shrink gradually as hydration proceeds. Muller et al. have proposed that for mature pastes these remain only as ca. 8 nm voids *Muller:2013*.
2. The *gel pores* with sizes of a few nanometres. These pores are located within the amorphous calcium-silicate-hydrates formed during cement hydration. Their name originates from Powers, who called the amorphous C–S–H precipitate a gel [2]. The gel pores are just filled with a pore solution in equilibrium with the surrounding phases.

---

<sup>5</sup>A mortar is a mixture of cement, aggregates smaller than 4 mm, and water.

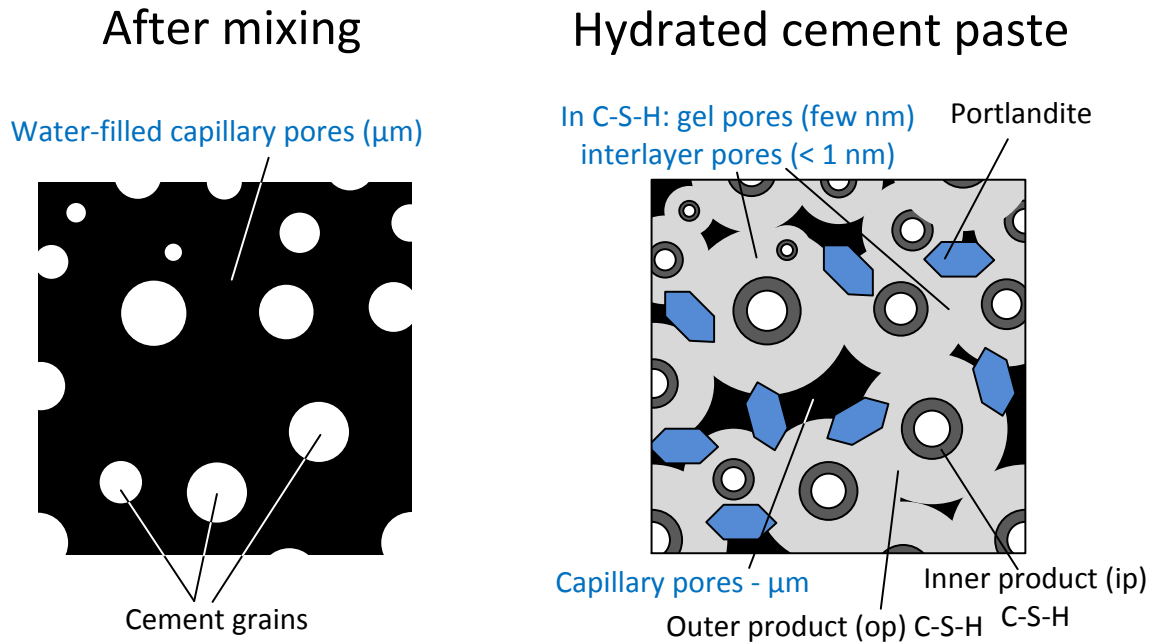


Fig. 2.3 Two-dimensional schematic of hydrating alite paste. Left: immediately after mixing, a loose packing of alite grains fills space. Right: as hydration proceeds, the capillary pore space is gradually filled up by hydration products. The water-filled spaces are marked by blue labels.

3. The *interlayer spaces/pores* are water-filled spaces with a size of an order of 1 nm. They are commonly attributed to be located between tobermorite-like sheets [4–6, 40].

### 2.3.2 Time-resolved cement hydration

Cement paste sets and hardens by a through-solution reaction: the cement grains dissolve, and as soon as solubility thresholds have been exceeded, the hydration products precipitate in the capillary pore spaces. The chemistry of this process has already been discussed in the previous section.

The progress of the hydration reaction can be monitored using a number of techniques. Among the most-common is isothermal calorimetry. Figure 2.4 shows the heat flux curve of an alite paste. Five distinct periods of reaction are often observed. Four of these are shown in the Figure 2.4 [38]. The fifth is the slow reaction, which occurs over years [37].

#### Initial reaction and period of slow reaction

The initial burst of heat, labelled as the initial reaction, is caused by the wetting of the anhydrous cement. Since the surface oxygen atoms of tricalcium silicate are highly basic,

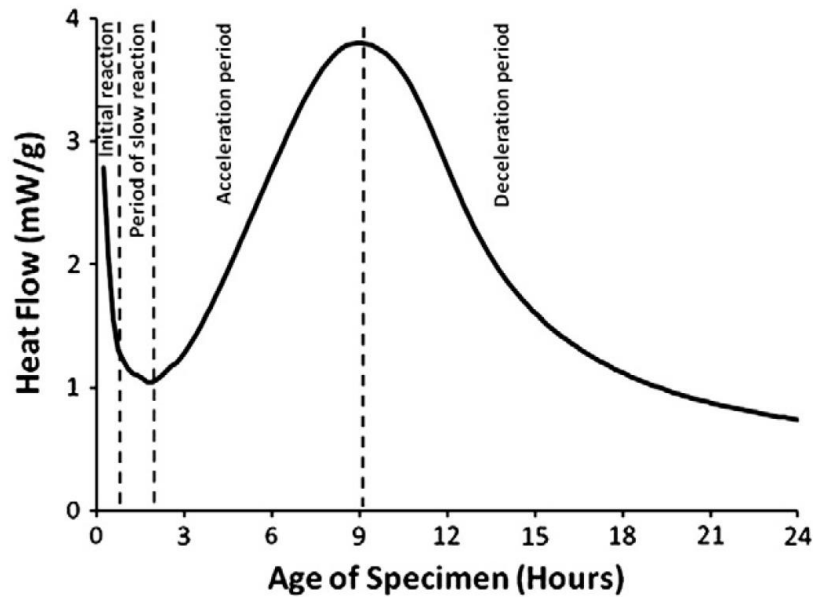


Fig. 2.4 Typical isothermal calorimetry data for the hydration of alite (impure tricalcium silicate). The hydration reaction is commonly separated into the four periods shown [22, 24, 37] and a fifth period, which is the slow maturing of the sample beyond the time scale shown in this Figure. Reproduced with permission from Bullard et al. [38].

their protonation releases a considerable amount of heat [22]. The reaction then slows down drastically. Garrault and Nonat showed that for pure alite this correlates with a rapid decrease of the concentration of dissolved silica (deprotonated silicic acid) [41]. Their curves for the concentration of silica are shown in Figure 2.5. This was interpreted, together with atomic force microscope analysis, as showing that C–S–H nuclei form during the period of initial reaction. It is followed by a minimum in the heat flow curve, which is referred to as the period of slow reaction or dormant period. In Portland cement, the system appears to be dormant, whilst for hydrating alite paste it is debated whether this period is actually just the onset of the subsequent nucleation and growth regime. Nevertheless, the reason for the deceleration of the reaction has been subject of an on-going debate [22, 37, 38].

### Acceleration period

After about three hours after mixing, the acceleration period begins. This period exhibits nucleation and growth kinetics of hydrates (in alite: C–S–H and portlandite) from nuclei that form either at the beginning of the acceleration period or even earlier during hydration [38, 41, 42].

The hydration rate of cement is defined as  $\partial\alpha/\partial t$ .  $\alpha$  denotes the degree of reaction, which is the fraction of cement consumed by the reaction. The growth rate is found to scale

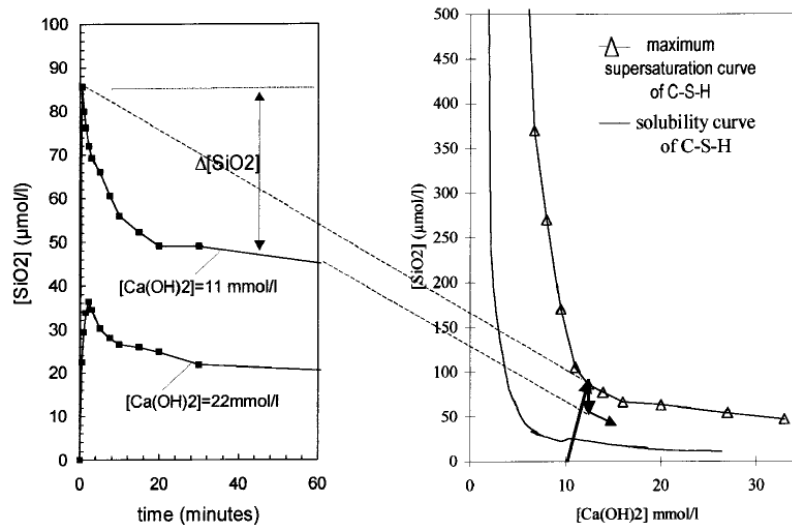


Fig. 2.5 Development of the silica concentration during the first hour of hydration of tricalcium silicate at a  $w/c = 50$ . The calcium hydroxide concentration in the solution was kept constant. The right curve shows the curve of super saturation and of maximum super saturation (nucleation curve) of C–S–H. Reproduced with permission from Garrault and Nonat [41].

as  $\partial\alpha/\partial t \sim \alpha^{1-1/n}$ . The growth exponent  $n$  is equivalent to that one defined by the KJMA<sup>6</sup> equation. Exponents between two and larger than three were reported for fits during the early acceleration period [37], indicating that early cement hydration follows conventional crystal growth kinetics.

The detailed mechanisms of the C–S–H growth depend on the accepted model for the meso-structure [3, 8, 18]. Their discussion is, therefore, proposed towards the end of this chapter.

### Deceleration period

The end of the nucleation and growth period is marked by a decrease in the reaction rate. Three different hypotheses for this slow-down are currently proposed [38]. The capillary pore space may be filled up by the outer product. The subsequent processes, either or both densification of the outer product and formation of the inner product, may be much slower. Ongoing space filling may eventually lead to a depercolated capillary pore space. Thus, reaction sites may become disconnected from water reservoirs by the developing micro structure. Lastly, small cement particles are dissolved quickly, thus reducing the surface

<sup>6</sup>The Kolmogorov-Johnson-Mehl-Avrami equation is a classic model for space filling by growing objects and discussed in some detail in the introduction to Chapter 5.

available for the further dissolution of reactants. A fourth opinion is expressed by Garrault et al., who observed a decrease in reaction rate when tricalcium silicate was hydrated in suspension. They explain the onset of the deceleration period as the progressive formation of a layer of hydration product on the cement grains. This hinders the diffusion of calcium and silica towards the reaction sites at the perimeter of the hydrate layer [41–44].

Space filling as the classical reason for the slow-down of the reaction has been considered in some detail. A review is given by Dolado and van Breugel [45], and some notable results are cited here. Bishnoi and Scrivener simulated alite hydration kinetics with the modelling platform  $\mu ic$  [46]. Being unable to fit the observed kinetic curves, they modified the simulation by assuming a progressive slowing down of the hydration, due to either diffusion control or the formation of a low-density product which densifies as the reaction progresses. The latter hypothesis was able to fit the observed reaction kinetics [46]. Scherer et al. used a nucleation and growth model to fit chemical shrinkage<sup>7</sup> curves for different cements. Whilst the fit was successful, the occurrence of the peak was observed for low degrees of hydration. He pointed out that if that result were real, it would mean the formation of a low density product, densifying later [47]. However, Scherer also points out that the type of equation used to fit hydration data are generally able to fit a wide range of curves, which may or may not be physical [48]. Nevertheless, the formation of a low-density product has also been observed in micrographs [39], and has also been measured by NMR [40].

Despite these efforts, the nucleation and growth period is still poorly understood [38].

## 2.4 Experimental techniques used to study C–S–H

Cement paste has been studied using a wide range of techniques, many of which focus on C–S–H. Important techniques are sorption measurements, pycnometry, electron microscopy, small-angle scattering, nano indentation, and <sup>1</sup>H-NMR. In this section, three of the most commonly used techniques are reviewed; the still cited pycnometry and sorption data from Feldman and Sereda will be discussed when their model is introduced. Thus, a section about sorption and pycnometry is not included here.

### 2.4.1 Electron microscopy

Electron microscopy has proven to be a powerful tool to obtain information about the spatial arrangement of cement hydration products [27, 39]. One particular problem of the method

---

<sup>7</sup>Chemical shrinkage is the volume reduction during cement hydration. It is also used to monitor cement hydration.

is the human tendency to be uncritical with visual information. Particularly with a highly inhomogeneous system, such as hydrated cement paste, this introduces the danger of over-interpreting the micrographs. The sample preparation requires at least partial drying, and sometimes sputtering or polishing. This may alter the nano and micro structure. Even environmental scanning electron microscopy techniques (ESEM) require some drying, which may effect the observed morphology [49]. It is also difficult to obtain a meaningful statistical representation of a sample with only a few images. Despite these problems, in this section, some selected images acquired with different electron microscopy techniques for different samples are presented and the main structural features discussed.

### **Early age morphology and surface seed density of C–S–H seeds**

Figure 2.6 shows selected micrographs of alite and tricalcium silicate surfaces after short hydration times, typically less than 2.5 h. For all three cases, the surface is relatively blank with only isolated spots of hydration products formed. This was also observed by Garrault and Nonat with atomic force microscopy [41]. Bazzoni et al. estimated the number of spots, which are interpreted as nuclei for the hydration product, as about  $33 \mu\text{m}^{-2}$  for tricalcium silicate paste as shown in Figure 2.6a [50]. A comparable value of  $16 \mu\text{m}^{-2}$  was found by counting, by the author of this thesis, in Figure 2.6b, which shows data for an impure tricalcium silicate. This suggests that typical seed densities are in that order of magnitude. This agrees well with model fits obtained by Scherer [47].

The clusters of C–S–H formed in Figure 2.6b and c appear to have a complicated morphology, even slightly crystalline. In the literature the expression "sheaf-of-wheat morphology" is used [51].

### **Micrographs of C–S–H found in mature cement paste**

Electron microscopy techniques have been used frequently to characterise mature cement pastes and synthetic C–S–H [27, 54]. Selected micrographs obtained for different systems are shown in Figure 2.7.

Figures 2.7a and c both show hydrated tricalcium silicate at a relatively advanced age (3 months and eight years). The dominant morphological features are the same. The product surrounding the cement grain, typically referred to as outer product [27], is less dense and has a fibrillar morphology. The inner product forming at the location of the cement grain is dense, probably because of direct conversion. Rößler et al. showed that the fibril grown in the outer product, presented in Figure 2.7(a-right), has crystalline features [55]. The more recent SEM micrograph of tricalcium silicate hydration in Figure 2.7b was taken after about

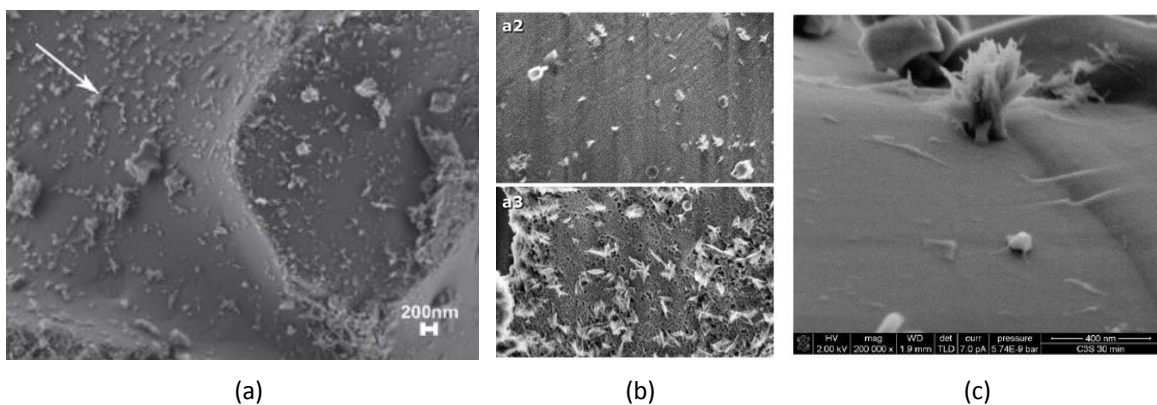


Fig. 2.6 (a) Scanning electron microscopy (SEM) image of pure tricalcium silicate powder hydrated for 2 h. The arrows indicate small clumps of C–S–H/hydration product forming on the surface. The surface concentration these clumps was taken as the C–S–H seed density and was counted as  $33 \mu\text{m}^{-2}$ . Reproduced with permission from [50]. (b) SEM micrograph of alite clinker hydrated for 1.3 h (above) and for 2.5 h (below) at a water-to-cement ratio of one. Note how the morphology of the individual clumps develop into more complex clusters and the opening of edge pits. The surface concentration of the clumps was counted by the author of this thesis as about  $16 \mu\text{m}^{-2}$  from the lower picture. Reproduced with permission from [52]. (c) SEM micrograph of clean surface of pure tricalcium silicate after 0.5 h hydration. A large C–S–H cluster is seen in the background. Reproduced with permission from [53].

seven hours and shows that the surface of the cement grain is covered by an open structure assembled by fibrils or sheets, which seems to be much more disordered compared to Figures 2.7a and c. Figure 2.7d shows a micrograph of a mature sample of Portland cement. The morphology is described as "fine fibrillar" and is much denser than the morphology observed for younger samples.

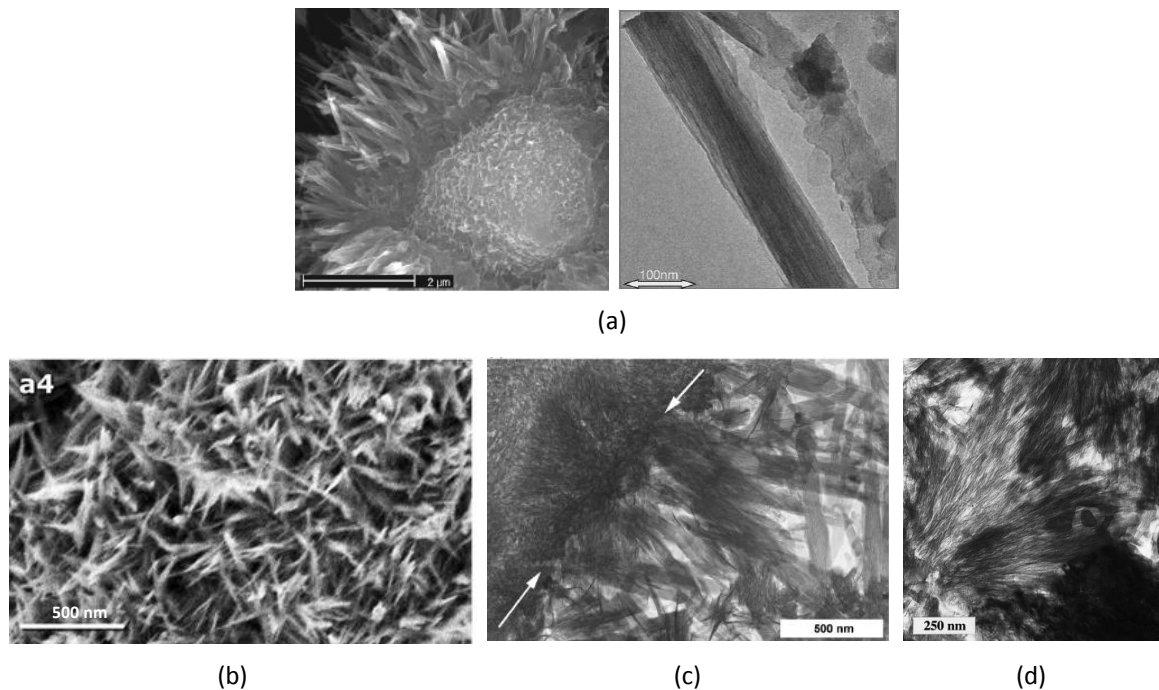


Fig. 2.7 (a) ESEM micrographs of a tricalcium silicate grain with minor impurities after three months of hydration at a water-to-cement ratio of 0.5. (a-left) A fibrillar structure is seen surrounding the grain. The grain itself is relatively featureless. The enlargement (a-right) shows one of these fibrils in TEM [55]. (b) Same conditions as in Figure 2.6b, but after 7 h hydration time. The surface of alite is no longer visible and covered by an open structure of hydration products [52]. (c) Popular TEM micrograph from Richardson showing an alite paste with water-cement-ratio 0.4, hydrated for eight years. The dense region in the left-upper corner of the micrograph is classified as inner product, the arrows indicate the boundary towards the outer product, which is fibrillar [27]. (d) TEM micrograph of a region in a mature Portland cement sample in the presence other hydration products. The C–S–H in the centre shows a dense morphology known as fine fibrillar [54].

## 2.4.2 Small-angle scattering

### Specific surfaces

Specific surfaces of porous samples can be obtained from small-angle scattering using the Porod method. This requires knowledge of the scattering contrast between pore fluid and solid phases present. Early work used estimated scattering contrasts [56]. More recent work used the contrast matching method to measure the scattering contrast directly. This allowed conclusions concerning the composition of C–S–H in cement paste. It was also concluded that the surfaces of the interlayer space between the tobermorite-like layers C–S–H are not seen by the scattering. [57]. This implies that there is considerable disorder on a short-range scale, smearing out the contrast. By combining SAXS and SANS measurements with contrast matching in different fluids, a C–S–H sum formula of  $C_{1.7}SH_{1.8}$  and a density of  $2.604 \text{ Mg m}^{-3}$  were derived from the measurements [9]. The development of the specific surface measured by SANS with hydration time and degree of hydration shows that the increase of surface ends after the first day of hydration. However, hydration still progresses further. It was concluded that an early age morphology of C–S–H, visible to neutrons, is formed, which is followed by the formation of a second C–S–H morphology, whose surface is invisible to neutrons [57].

### Spatial arrangement of solids from SAS

The scattering intensity is related to the Fourier transform of the autocorrelation of the scattering length density distribution. Thus, spatial information can be obtained from the dependence of the intensity on the  $q$  vector. However, since a given autocorrelation does not lead to a unique structure, the interpretation of this data is model-dependent. A recent small-angle scattering curve is shown in Figure 2.8 [30]. The details of the curve, interpreted by the slope of the graph, are shown in the Figure and explained below.

Early small-angle neutron scattering experiments were analysed assuming that scattering would be caused by circular pores of a size range between 1 and 10 nm [56]. Later experiments found a range in which the intensity decayed as approximately  $q^{-2.5}$  before entering the Porod regime. This was interpreted using a model of a volume fractal of a particle packing. The fractal packing of particles with a diameter of *ca.* 5 nm extends towards about 100 nm. The fractal dimension was 2.5–2.7 [18]. It was proposed that the fractal structure is formed via a diffusion limited aggregation mechanism which would lead to similar fractal exponents. A wide range of different cement systems was studied, and a second power law decay was found with  $q^{-3.2}$  to  $q^{-3.7}$ . This is interpreted as a surface fractal on the cement grain surface [30, 58]. Different studies have shown that the application of a fractal particle

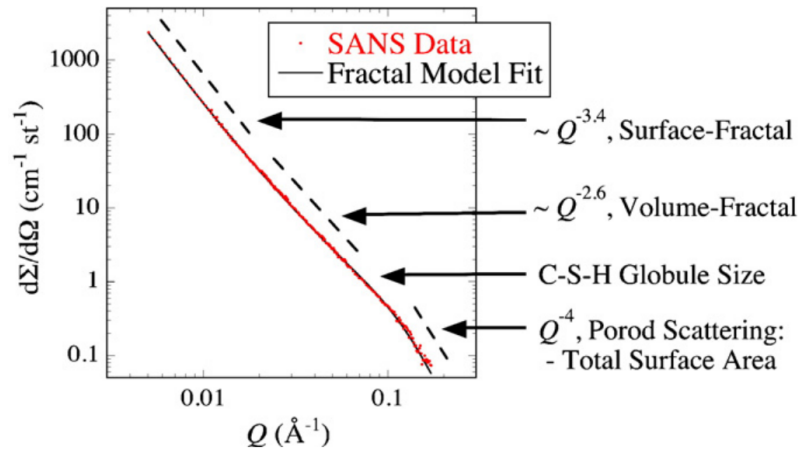


Fig. 2.8 Typical small-angle neutron scattering curve for cement. The labels of the regions and the interpretations are as in the original. Reproduced with permission from Allen et al. [30].

model leads to 5 nm particle aggregates. Their properties, like the local packing fraction, etc., change in a predictable manner, supporting the proposal of a drying colloidal aggregate [59]. De-calcification by leaching of cement samples decreased the slope in the volume fractal regime towards  $q^{-2}$ . This was interpreted as a structural change towards sheets, since the form factor of discs decays as  $q^{-2}$  [59]. The specific surface area, measured by neutrons, doubled. This was interpreted, within the bounds of the Jennings' model [3], as high density (HD)-C–S–H being converted into low density (LD)-C–S–H.

Surprisingly, few small-angle studies were found by this author for synthetic C–S–H. Recently, Chian et al. studied synthetic C–S–H samples using SANS. They observed an interlayer peak, which suggests that also the surface of the interlayer should be visible to the neutrons. The data was analysed with a new model based on the second generation of Jennings' model [4]. The base particle is a stack of discs with a distribution of radii, a variable number of repeat layers and layer spacing. Their packing in space was described by a fractal model. The radii of the observed particles was between 6 nm and 10 nm, and the interlayer spacing depended on the water content of the sample. They noted that despite the successful fitting of their results with a particle model the larger radii could also be interpreted towards a more continuous sheet structure [60].

Brisard and Levitz studied the numerical simulation of small-angle scattering of particle packings and how to exclude domain size effects. With this background, they discussed potential particle models for C–S–H. They dismissed simple particle packings of spheres and discs due to the presence of a correlation peak, as also found by the author of this thesis (see Chapter 4). Diffusion and reaction limited structures were excluded due to the relatively

low solid fractions obtainable. Instead a particle packing with a power-law size distribution was proposed, which may form by a packing limited growth mechanism [61, 62].

### 2.4.3 Nuclear magnetic resonance ( $^1\text{H-NMR}$ )

Proton relaxometry measurements are one of the most interesting methods employed to study cement paste and the meso-structure of C–S–H. The method can be explained with some simplifications as follows: the magnetisation of the spins is tipped in the xy-plane, and the loss of coherence between the rotating spin vectors is measured. In smaller pores, the dominant loss mechanism is due to interactions between the hydrogen and the pore wall. The system can be modelled by the relaxation-diffusion equation, describing the motion of the spins in the pore space [63]. The surface relaxation can be described using a first-order process consuming the coherence between the spins on pore walls as boundary conditions. The data is often analysed using inverse Laplace transform to obtain the decay time of the eigenmodes from the NMR signal [64]. If the decay of magnetisation is much slower than the diffusion process, only a single Eigenmode is seen, analogous to a first-order reaction in a well-mixed system; this situation is assumed for cement. Since the pores in cement are very small, layers of structured water molecules at the surface of the pores become relevant [65]. As a magnetic method, NMR measurements become increasingly difficult in the presence of paramagnetic impurities.

Proton relaxometry has been used to study cement pastes since the late 1970s [66]. Only selected later results are reviewed here. McDonald et al. conducted experiments on progressively dried white cement paste. Two distinct water environments were identified and were assigned as interlayer pores and gel pores in a Feldman-Sereda style sheet model. The emptying of these pores and the formation of water surface layers was also studied. From the relaxation time, the width of the interlayer space was estimated as 1.5 nm and the larger pores were found to be about 4.1 nm in size, assuming an infinite planar pore. The overall sheet porosity is estimated as 47 % [6]. This work was continued by Muller et al. Refined experimental procedures allow them to quantify the fraction of water bound in solid hydrate phases, such as portlandite and ettringite. Three mobile water environments were identified in mature samples: water in the interlayer space with a width of about 0.85 nm, water in the pores with 2.5 nm width and water larger pores which were termed interhydrate pores with a height of 8 nm. The 8 nm pores are the remains of the capillary pores. In all cases, the pore shape was again assumed to be an infinite slit pore. Their analysis allows them to calculate the density of the C–S–H units consisting of interlayer water and layers as  $2.65 \text{ g cm}^{-3}$  for white cement paste cured under water after 28 d. The data provided also allows one to compute the solid volume fraction of C–S–H,  $\varphi_s$ , and the pore volume fractions for in-

terlayer  $\varphi_{il}$  and gel pore space  $\varphi_g$  [40]. The same authors also measured a pore-resolved sorption isotherm with NMR, which allowed them to quantify the progressively emptying of different pore spaces [67]. NMR relaxometry can potentially also be used to quantify the exchange between the different water environments [68].

## 2.5 Proposed models for the meso-structure of C–S–H

In this section, the most important models for the structure of the calcium-silicate-hydrates are reviewed. The question of the structure is almost as old as Portland cement itself. In 1887 le Chatelier proposed a crystal theory, and in 1893 Michaëlis proposed the first colloidal theory [24, 27]. Twenty years later, the C–S–H structure was still the subject of an intense debate [69]. This debate is ongoing until today.

### 2.5.1 The Powers-Brownyard model (1940s)

The Powers-Brownyard model is schematically shown in Figure 2.9a. It describes cement paste as space filled by Portlandite, some minor hydrates, capillary pores and the cement gel. The capillary pores are large pores between the hydration products. Powers noted that these pores may depercolate under some conditions. Thus, the capillary pores may be only connected via the pores in the cement gel. The dominant cement gel is assembled by particles with a diameter of about 4.5 nm (8.6 atomic units in the original publication) [2]. The space within these particles is called *gel porosity* and is on average 0.8 nm wide [2]. The specific surface area is about  $700 \text{ m}^2 \text{ g}^{-1}$  (of solid) as measured by water sorption using the Brunnauer-Emmet-Teller (BET) technique. The gel porosity is defined as the space accessible to water, but not nitrogen. In contrast, nitrogen can only access the capillary pores. Powers does not specify the kind of cohesive force within the gel, but speculates it may be a mixture of van der Waals forces and chemical cross-linking between the particles. The lowest end of the porosity of hydrated cement paste is given as about 26%. Powers identifies two types of water: evaporable water, contained in capillary and gel pores, and non-evaporable water being part of the structure of the gel particles. The permeability of the gel is assigned a measured value of  $7 \times 10^{-23} \text{ m}^2$ . [2, 24]. As Powers notes: "Most of the research needed in this field is yet to be done." [2].

### 2.5.2 Wittmann model (1970s)

The Wittmann model describes the hydration product as xerogel [24]. The average particle radius is assumed to be about 10 nm. Water interacting with the structure decreases the

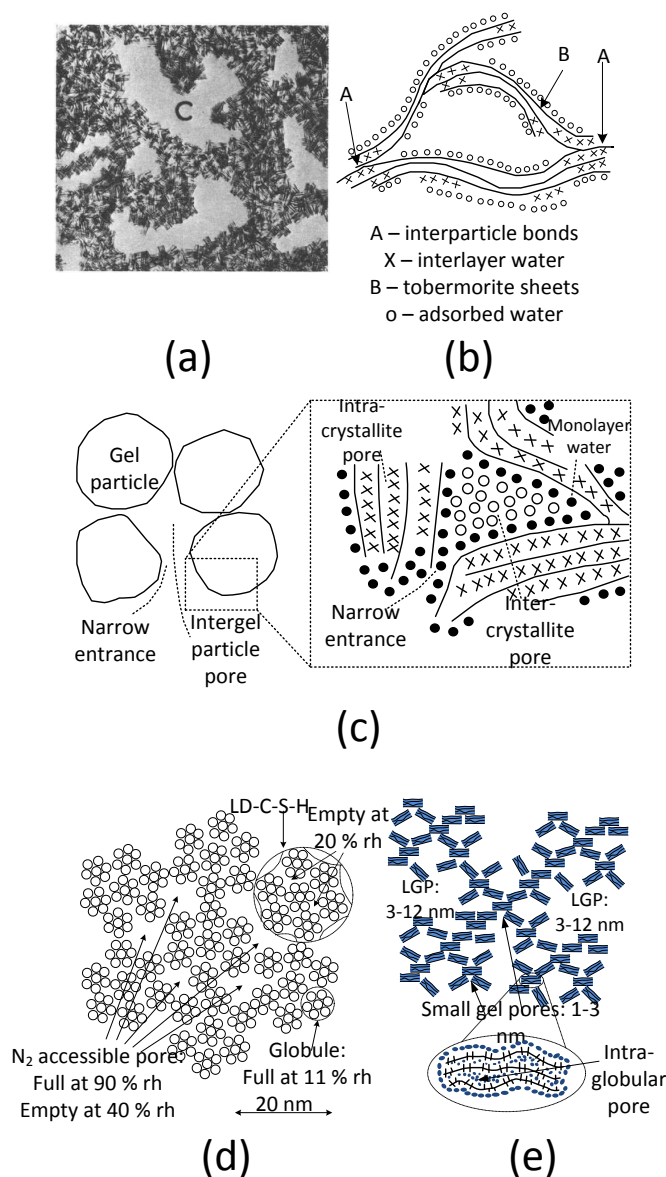


Fig. 2.9 Overview of most of the C–S–H models proposed since the 1950s. A scale can be added to models (b–e) by assuming that the layer-to-layer distance is about 1 nm. (a): the Powers model (reproduced with permission from [2]), (b) the Feldman-Sereda model (redrawn from [70]), (c) the Daimon model (redrawn from [71]). (d) Jennings’ model from 2000 (redrawn from [3]), (e) Jennings’ model from 2008. The enlargement shows the internal structure of each particle. The abbreviation LGP denotes large gel pores (redrawn from [4]).

surface energy, which in turn influences the mechanical properties [72]. The author of this thesis found accessing further literature difficult. This model does not seem to play too much role nowadays, because some of its ideas have been included in Jennings' model [3].

### 2.5.3 The Feldman-Sereda model (1970s)

The Feldman-Sereda (F-S) model is the result of studies of the interaction between water and cement paste. Adsorption isotherms regarding the water-uptake and the macroscopic swelling/contraction during drying and rewetting were investigated, as well as density and mechanical properties measured as a function of the relative humidity the cement was equilibrated with. The chemical similarity of the the C–S–H phases with tobermorite was also realised.

BET experiments on cement paste with nitrogen and water as adsorbent gave very different results for the specific surface of D-dried<sup>8</sup> cement paste. It was also found that the sorption isotherm of water shows hysteresis, even for relatively low relative humidities: this means that the adsorption of water in cement paste at this humidity-range is not reversible. Therefore, the assumptions behind the BET method to determine the specific surface by vapour adsorption become invalid. The solid density of C–S–H, measured by helium pycnometry, also changes depending on the relative humidity at which the sample was equilibrated. If the samples were progressively dried, the density changed spontaneously. A corresponding change of mechanical properties was observed at this point.

Feldman and Sereda explain these observations by describing C–S–H as a disordered arrangement of tobermorite-like sheets, as shown in Figure 2.9b. The space sandwiched between the sheets is the interlayer space and accessible to helium, water, and to molecules of similar properties as water such as methanol. The response of cement paste to changes in relative humidity is explained by gradual removal of water from the interlayer space and eventually by collapse of the sheet structure, as the interlayer space is empty. Some of these changes seem to be reversible. Feldman and Sereda include the larger spaces between the layers in the capillary pore space, a notion which has changed over time (see below). The interlayer space is not seen as a pore space and the water is seen as part of the structure. Cohesive forces between the layers with and without the presence of water are postulated [5, 70, 74] (see also Figure 2.9b). Many authors consider the Feldman-Sereda model today as a model of spatially extended sheets, whilst the author of this thesis did not find any comment on that in the manuscripts he has read.

The model has been developed further. McDonald, Rodin and Valori's interpretation of

---

<sup>8</sup>D-drying refers to equilibrating the sample with the water vapour pressure at  $-79^{\circ}\text{C}$ , which is about  $6.7 \times 10^{-2} \text{ Pa}$  [73].

the water populations measured by NMR has led to the extension of the model towards gel pores [6]. Other authors speculated about the spatial extent of the sheet structure, towards larger structures. Gartner proposed a mechanism for cement hydration based on the growth of sheets [8] and presents X-ray microscopy images to support his point [51]. Scrivener and Nonat propose an extended sheet structure behaving like a colloid [7]. Today's interpretation of the F-S model seems to be the second-most popular model for the meso-structure of C-S-H, where it is seen as a quasi-continuous, highly disordered, sheet structure.

#### 2.5.4 The Daimon-Model (1976)

The author of this thesis finds the Daimon model [71] of particular interest because it combines elements of most of the other models discussed here. The structure of the cement gel is seen as relatively large particles whose size is not specified. The size of the *intergel particle pores* is given as 16 nm to 100 nm, indicating particles of at least the same size. Inside, the particles have a structure similar to McDonald's perception of the Feldman-Sereda model. Disordered tobermorite-like layers surround larger pores, which are called inter crystallite pores and have a size range between 0.6 nm to 1.6 nm. This notion seems to be similar to the modern concept of gel pores located between disordered aligned layers of tobermorite [6]. Surprisingly, it has a relatively low number of citations.

#### 2.5.5 The Jennings models (2000s)

The most recent C-S-H model is the Jennings model [3, 4]. The development of the ideas for this model actually started in the mid-nineties, when Tennis and Jennings proposed a new model to predict the composition of hydrated cement paste. Using a set of literature known reactions and associated Avrami-style kinetic constants, they approximated the density for saturated C-S-H as  $1760 \text{ kg m}^{-3}$  and for D-dried C-S-H as  $2860 \text{ kg m}^{-3}$ . The different densities and surface areas obtained by water and nitrogen (see in the section about the Feldman-Sereda model) were explained by introducing two different types of C-S-H. The first type being accessible to nitrogen and water, the other one only to water. The ratio between these two types of C-S-H was found by fitting to hydration data [75]. This idea was then developed, with some model extensions towards the concept of high-density (HD) and low-density (LD) C-S-H, where the densities were again obtained by fitting experimental data for cement hydration [76]. It is assumed that the LD-C-S-H is formed as low-density outer product in the capillary pores, whilst the HD modification forms later.

Jennings' first colloid model, schematic shown in Figure 2.9d, is an attempt to give the Jennings-Tennis model a simple physical basis. Based on the density values obtained for C-

S–H with empty pore volumes, a C–S–H base unit with a radius of about 1.5 nm is defined. This base unit may be similar to a tobermorite elementary cell. The base units are packed in globules with a packing density of 82 %, assuming that the base units may not be spherical, enabling the high packing fraction [77]. The globule radius is 2.5 nm, taken from neutron scattering results. These globules then form HD and LD-C–S–H with densities obtained from the Jennings-Tennis model. This leads to a packing density of 87 % for the HD form, assuming again that the globules may be squashed, and of 72 % for LD-C–S–H. Its packing is either described as an imperfect colloidal crystal, or the high packing fraction is justified by assuming non-spherical particles. It is assumed that the LD-C–S–H again forms clusters with a radius of 10 nm, which was probably concluded from sorption experiments with larger molecules. It is assumed that the resultant hierarchical packing leads to different pore sizes on different levels in the hierarchy. This can explain the sorption isotherms obtained by different molecules: water can enter the smallest pores, whilst nitrogen and larger molecules cannot. Therefore, parts of the pore system are inaccessible for different molecules. It is also claimed that the resultant structure has a fractal dimension of 2.74, agreeing with the "volume fractal region" reported by neutron scattering. It was suggested that the C–S–H morphologies observed in micrographs form by self-organisation of the colloidal particles [3]. Phenomena like creep and the mechanical response to drying have been explained based on rearrangements of the globules and stresses due to menisci entering the small pore space during drying [78].

In 2008, a revised version of the Jennings model was published [4], which focuses on the low-density C–S–H proposed to form in the capillary pore space during cement hydration. The model is outlined in Figure 2.9e. The concept of the hierarchical particle packing was kept, but the idea of the 1.5 nm base unit forming a globule was replaced by introducing a new globule of 2.5 nm radius with a layered internal structure. The new globule is shown in Figure 2.9e. The globule has three water environments: the interlayer space, the intra-globular pores and surface layers adsorbed on the particle surface. In addition to these three water environments, two groups of pores in the hierarchical packing are proposed: small-gel pores ranging in size between 1 and 3 nm and the large gel pores (LGP in Figure 2.9e), ranging from 3 to 12 nm. Depending on the degree of water saturation, the packing density of these globules ranges between 0.7 and 0.59. Hysteresis in the sorption isotherms at low relative-humidity is explained by preferential emptying of the intra-globular pores.

Jennings' model has become increasingly popular, due to its at least semi-quantitative nature and the fact that it is based on a relatively easily understandable concept of particles. It has induced considerable work within the MIT group, for example, multi-technique in-

vestigations of cement paste [79]. For sub-stoichiometric<sup>9</sup> conditions, even three different C–S–H phases with different mechanical properties were found. This was interpreted in the light of Jennings' model as regions with three different packing densities [80]. In this context, the mechanical response of polydisperse packing has been investigated numerically by Masoero et al. The packings were generated using a Metropolis Monte Carlo algorithm with a Lennard-Jones-type potential between the particles. New particles were inserted with a probability depending on the free-energy gain for the whole structure during the insertion. Moderate agreement with experimental data was achieved [81]. This idea regarding the particle insertion was also used by Ioannidou et al. to describe the time-resolved development of a Jennings-type particle model. A molecular dynamic/particle dynamic scheme was employed to simulate the behaviour of particles with a typical size of 10 nm to 30 nm with a Lennard-Jones potential and Yukawa repulsion. The potential was parameterised according to experimental data<sup>10</sup>. Time evolution in the model was controlled not by molecular dynamics but by logarithm of the occurrence of insertions. The idea is completely phenomenological. However, the shape of hydration curves can be reproduced for the space-filling versus time plot [82].

## 2.6 Discussion and Conclusions

Looking back at the models which have been reviewed in this section, one can split them into the two classes initially proposed by Michaëlis and le Chatelier: colloidal particle and crystalline models. Crystalline may mean a highly defective crystal. The Feldman-Sereda model and its more modern derivatives can probably be seen as highly defective sheet crystals.

The colloidal model is currently the most popular approach to the meso-structure of C–S–H. This probably due to be due to its conceptual simplicity, its quantitative nature when it comes to the description of pycnometry and surface data, and the fact that particles are easy to handle - both conceptually as well as numerically. If one broadens the scope and considers the formation of these structures, conceptual problems can be found. Ongoing nucleation of particles is unlikely to happen in cement paste due to the insufficient supersaturation relative to C–S–H [38]. The way that current colloidal models are built requires the assumption of a monodisperse, or at least rather narrow, size distribution of colloidal particles. It is not clear why these conditions exist, under which C–S–H particles should be able to nucleate but not continuously grow at the same time. Normally, nucleation is hindered by the surface tension

---

<sup>9</sup>This refers to a  $w/c$ -ratio smaller than approximately 0.4. This means that the water added to the mixture is not enough to for complete hydration of the cement powder.

<sup>10</sup>The resulting potential function looks like a Lennard-Jones potential with a small repulsive hump before the potential energy approaches zero for infinite distances.

of the new phase. This means that nucleation needs a higher super saturation than growth, in order to occur. The slope of the hydration curve during the early nucleation is cited as leading to growth exponents of three and larger. For a process dominated by nucleation at constant concentration, the slope is expected to be constant. Brisard and Levitz pointed out that diffusion limited aggregation (DLA) cannot explain the formation of the particles, since the structures are too open [61]. The proponents of the particle model suggest that the DLA clusters may grow into each other, which cannot happen within conventional DLA due to steric blocking of further aggregation at the surface of contact between both clusters. Nevertheless, a cluster-rearrangement mechanism is conceivable.

Ionnadiou et al. [82] and Masoero et al. [81] proposed a Monte Carlo scheme to control particle nucleation, which effectively favours heterogeneous particle nucleation in the vicinity of previously deposited particles. Such a process is, however, no longer diffusion limited aggregation unless the cohesion forces between the particles are weak and allow for cluster rearrangement.

The other popular model is the sheet model of Feldman and Sereda, which has received various conceptual extensions. A model of growing sheets is attractive for a number of reasons. Most micrographs of the outer product in cement paste fit this picture, such as those shown in Figure 2.7. Nevertheless, neither 5 nm-particles nor sheets would be visible in the micrographs. The classic chemical argument that the macroscopic shape of a structure is related to the atomic arrangement may be valid though. C–S–H shown in micrographs also do not appear like diffusion limited aggregation clusters. The synthetic C–S–H systems appear, at least to the author of this thesis, like thin sheets, even those which are described as fibrillar: these occur in conditions which are relatively lean in silicon. Thus, a preferential growth direction in the direction of the silicon chains on the surface of the tobermorite-like sheets is conceivable. The growth kinetics of such a model are, as Gartner points out, likely to agree with the growth exponents reported for the early nucleation and growth periods [8].

A considerable weakness of the sheet-model, compared to the colloidal model, is its vague nature. Since it is non-quantitative, it lacks the convincing quantitative argument of Jennings' model. Also, whilst growth of a bulky crystal of tobermorite may be easy to model, it is not clear how defects could be introduced leading to the large volume of gel pores measured by NMR. The growth mechanism must be much more complicated than growth of straight sheets, since the resultant structures are amorphous and highly disordered. This disorder cannot be introduced by a large number of randomly oriented sheet seeds, since all estimates of the seed density [47, 50] are relatively low. Scherer [47], Bishnoi and Scrivener [46] suggest the formation of a low-density hydration product which densifies later. Sheet growth is able to sample a large amount of space, so this idea is con-

ceivable. On the other hand, a densifying particle packing could describe this as well, such as the packing-limited growth model as structure for C–S–H proposed by Brisard and Levitz [61]. A packing generated by packing-limited growth has a fractal dimension of about 2.5, agreeing with the small-angle scattering. This is due to the blocking of growing particles by previously grown particles. Such phenomena are, however, also likely to be found in other growing structures.

Both models share two ideas: a hierarchical pore space, and some mechanical flexibility. In the colloidal model, these two ideas are incorporated by allowing the particles to rearrange, whilst in the sheet model one can assume some mobility of sheet-sheet contacts, particularly at defects. The main conceptual difference seems to be the mechanism of formation. This author wonders whether both concepts could be reconciled by replacing the concept of a colloidal particle with a grain boundary.

The picture emerging from this literature review suggests that there is no such thing as "a structure for C–S–H". In fact, the discussion revolves around two conceptual models, which are the colloidal model and the sheet model.

This PhD began as a project investigating moisture transport through C–S–H numerically. The colloidal model appeared to be better established, so it was chosen as the structural model for the moisture transport investigation. This has led to Chapter 4. With increasing understanding of the field, the author realised that it would be more appropriate to step back and study the structural aspect of C–S–H formation. Since colloidal models have been well-covered by recent numerical modelling, it was decided to investigate the space filling by sheets, which gave this thesis its title and led to chapters 5 and 6. A second reason not to focus on the colloidal model is that this work is currently being pushed ahead by a large group of researchers associated with MIT. Consequently, it was decided to investigate the rarely-studied sheet model.

# Chapter 3

## Methods

This chapter gives a brief summary of the background to general methods used in this work. This a brief introduction into the background of the kinetic Monte Carlo method used in Chapter 5, how to simulate small-angle scattering curves as done in Chapters 4 and 6 and how to compute the transport properties of a numerical representation of a structure using lattice Boltzmann methods, Chapters 4 and 6.

### 3.1 Introduction

In this chapter, some of the methods used to generate and characterise the structures generated in this thesis are reviewed. In none of the cases does the author claim any intellectual ownership. Nevertheless, all codes used in this work were developed by himself.

In Section 3.2, a brief overview of Monte Carlo methods and the algorithm developed formally. A very brief introduction to small-angle scattering is given in 3.3, together with a brief outline of the Schmidt-Rohr method used to calculate small-angle scattering curves from voxel representations of random structures. In Section 3.4, the lattice Boltzmann-based scheme for the prediction of transport properties of random structures is presented.

### 3.2 Kinetic Monte Carlo methods

Monte Carlo (MC) methods are a broad class of methods used to solve problems by the use of random numbers. Modern MC methods appeared together with modern computers in the 1950's [83] to study the properties of equilibrium phases. These methods use random numbers to sample phase space, finding the most-likely equilibrium configuration. Overviews

about different Monte Carlo techniques are given by numerous authors [84, 85].

The class of Monte Carlo used in this work is known today as kinetic Monte Carlo (KMC), however, the term dynamic Monte Carlo is also in use. In this thesis, it is used in Chapter 5 to ensure correct evolution of time in a sheet growth model. The early KMC methods were developed to add a time scale to the probabilistic simulation of a system, such as diffusion in alloys [86], Ising spin systems [87], surface desorption and molecular beam epitaxy [88, 89], recrystallisation [90] and chemical reactions [91]. Recently, the technique was used to extend the time scale of molecular dynamics simulations of water-solid interactions to predict NMR data by Faux et al. [65]. The well-established nature and importance of the technique is confirmed by reviews and introductory texts [92, 93].

In the next subsection, the derivation of the general algorithm is given to demonstrate the underlying principle. It connects to the description of the sheet growth algorithm in the self-contained Chapter 5.

### 3.2.1 Derivation of the Gillespie algorithm

In this section, the derivation of the Gillespie algorithm is given as a representative example of a kinetic Monte Carlo algorithm. The derivation follows closely Gillespie's work, but is generalised towards a system of processes instead of reactions [91].

Consider a system in which  $N$  different processes  $\{R_i\}$  can occur. Each process can occur up to  $n_i$  times at any given moment. The probability for a process  $R_i$  to occur in the time interval  $(t, t + \delta t)$  is:

$$k_i \delta t \tag{3.1}$$

$k_i$  is the rate of the process, interpreted as the number of this type of process occurring per unit time. In Gillespie's original derivation, the different processes are chemical reactions, and  $n_i$  denotes the number of different permutations of atoms capable to react in a certain way. Equally, the two different processes might be the diffusive movements of two species with different diffusion coefficients, then,  $n_i$  denotes the number of possible movements for each species.

The problem can be approached by defining a *process probability density function* (PPDF),  $f(\tau, i)$ . In this case,  $f(\tau, i)d\tau$  is the joint probability that at time  $t$  the next process will occur in the interval  $(t + \tau, t + \tau + d\tau)$  and will be of type  $i$ . This joint probability density function can be written as product of two probabilities: the probability  $\bar{P}(\tau)$  that no event occurs in the interval  $(t, t + \tau)$ , and the probability that an event of type  $i$  will occur in a time interval  $d\tau$ .

$$f(\tau, i)d\tau = \bar{P}(\tau)P_i(d\tau).$$

$P_i(d\tau)$  is found from Equation 3.1, so one obtains:

$$f(\tau, i)d\tau = \bar{P}(\tau)k_i n_i d\tau. \quad (3.2)$$

The probability that no event occurs in the time interval  $(t, t + \tau)$  can be calculated by splitting the time interval  $\tau$  into  $M$  subintervals of length  $y = \frac{\tau}{M}$ . The probability that no event of type  $i$  will occur in an interval of length  $y$  is obtained from Equation 3.1 as  $1 - k_i n_i y$ . The joint probability that no event of type  $i$  occurs in any of the  $M$  time intervals is then:

$$\bar{P}(\tau) = \left( \prod_{i=0}^{N-1} (1 - k_i n_i y) \right)^M = \left( 1 - \sum_{i=0}^{N-1} k_i n_i y \right)^M. \quad (3.3)$$

Taking the limit for infinitesimally small  $y$ , one obtains an exponential function,

$$\bar{P}(\tau) = \exp\left(-\sum_{i=0}^{N-1} k_i n_i \tau\right). \quad (3.4)$$

The expression for the PPDF is then:

$$f(\tau, i) = k_i n_i \exp\left(-\sum_{j=0}^{N-1} k_j n_j \tau\right) \quad (3.5)$$

The PPDF can now be used to construct an algorithm simulating the evolution of such a system in time. An ideal algorithm performs one process per iteration. To do so, one needs to predict the length of the time step per iteration as well as the process to occur next. In other words, one needs to know the time difference between the current and the previous process irrespective of the types of these processes.

Both information can be obtained from the PPDF. The joint probability density function  $f(\tau, t)$  can be rewritten as

$$f(\tau, i) = f(\tau) \cdot P(i|\tau). \quad (3.6)$$

$f(\tau)d\tau$  is the probability for any process to occur in the interval  $(t + \tau, t + \tau + d\tau)$ . For the algorithm, it means that it is the probability that the length of time passing during an iteration is  $\tau$ .  $P(i|\tau)$  is the joint probability that if an event occurs after a time  $\tau$ , it will be of type  $i$ . From the definition of  $f(\tau, i)$  above follows:

$$f(\tau) = \sum_{i=0}^{N-1} f(\tau, i) = \sum_{i=0}^{N-1} k_i n_i \exp\left(-\sum_{j=0}^{N-1} k_j n_j \tau\right). \quad (3.7)$$

The length of each time step can now be sampled from this probability density function by finding a time step as

$$\tau = \left( \sum_{i=0}^{N-1} k_i n_i \right)^{-1} \ln(1/X), \quad (3.8)$$

where  $X \in [0, 1)$  is a uniformly distributed random number. The sum in this equation is also known as the rate line. It is noted that some authors ignore the logarithm since it averages to unity and use instead [86, 88, 89]

$$\tau = \left( \sum_{i=0}^{N-1} k_i n_i \tau \right)^{-1}. \quad (3.9)$$

Substitution of Equation 3.7 in Equation 3.6 and rearranging leads to:

$$f(i|\tau) = \frac{k_i n_i}{\sum_{j=0}^{N-1} k_j n_j}. \quad (3.10)$$

Sampling this distribution is trivial. An example flow diagram of the algorithm is given in Chapter 5.

### 3.3 Small-angle neutron scattering prediction

If any radiation, such as X-rays or neutrons, passes through a material, it is scattered. For simplicity, the radiation is monochromatic with wavelength  $\lambda$ . The scattering centres are the atomic nuclei (neutrons) or the corresponding electron shells (X-rays). Thus, the scattering of X-rays and neutrons of the same material may effectively see a very different picture, which makes both methods complementary. In this section, only elastic scattering methods are considered. A detailed presentation of the small-angle scattering theory outlined here can be found in chapters one and five of Roe's book [94].

The relative positions of scattering centres leads to interference between the scattered waves from different scattering centres. The scattered wave receives a phase shift encoding spatial information about the scattering centre it has been scattered by. Interference between these waves leads to an intensity  $I(\mathbf{q})$  depending on the direction of observation. The  $\mathbf{q}$ -vector is defined as the difference between the direction of the incident radiation and the observed direction, multiplied by  $2\pi/\lambda$ . Therefore, the intensity encodes information about the spatial arrangement of matter.

It can be shown that the amplitude of the radiation scattered in direction  $\mathbf{q}$  is given by

$$A(\mathbf{q}) = \int_V \rho_S(\mathbf{r}) \exp(-i\mathbf{q} \cdot \mathbf{r}) d\mathbf{r}. \quad (3.11)$$

This expression is the Fourier transform of the scattering length density function  $\rho_S(\mathbf{r})$ , which describes the spatial distribution of scattering centres. The Fourier transform offers another view on the method: the amplitude is a measure for the occurrence of a spatial frequency  $q$ , whose associated (wave) length is  $\frac{2\pi}{q}$ . Neither the amplitude of neutrons nor that of x-rays can be measured, instead, the detector obtains the intensity. It is related to the amplitude as  $I \propto |A|^2$ . Taking the absolute value of the amplitude means that the complex part of the amplitude is lost during detection, thus, geometrical information is lost. It can be shown that

$$I(\mathbf{q}) = \int_{(V)} \Gamma_{\rho_S}(\mathbf{r}) \exp(-i\mathbf{q} \cdot \mathbf{r}) d\mathbf{r}. \quad (3.12)$$

The intensity is the Fourier transform of the autocorrelation function of the scattering length distribution  $\Gamma_{\rho_S}(\mathbf{r}') = \langle \rho_c(\mathbf{r}) \rho_S(\mathbf{r} + \mathbf{r}') \rangle_V$  [95]. It contains less information than the scattering length distribution  $\rho_S(\mathbf{r})$  itself. The angled brackets denote the volume average. Thus, it is not possible to obtain  $\rho_S(\mathbf{r})$ , or what one may call "the structure", by inverse Fourier transform.

Elastic scattering techniques can be broadly split into two types: diffraction methods look on the arrangement of atoms, whilst small-angle scattering (SAS) methods look on larger length scales. The separation is at about 1 nm. Only small-angle scattering of neutrons are directly relevant to this thesis. In both cases, the interpretation of the scattering results requires the use of models. Geometrical interpretation of SAS curves by fitting analytical models is probably the most common. For particles, these include, but are not limited to, spheres, discs, rods, hollow versions of these, core-shell versions of these and many others. Long-range correlations can be captured for particle systems in the structure factor  $S(\mathbf{q})$ .

More complicated structures may not allow the use of simple models. The numerical evaluation of Equation 3.12 allows one to predict the scattering curve of a sample.

Different methods are mentioned in the literature to simulate the small-angle scattering pattern of a given structure [61, 96, 97]. Different methods were used in different chapters of this thesis. For the spherocylinder packings in Chapter 4, the method proposed by Schmidt-Rohr was used, as explained below. Since the sheet structures introduced in Chapter 5 are difficult to describe on a lattice, it was decided to choose another approach to simulate the scattering curve, which is outlined in Chapter 6.

### 3.3.1 The Schmidt-Rohr scheme for scattering curve prediction

The procedure used in this work to predict the scattering curves of three-dimensional structures follows Schmidt-Rohr [97]. Instead of a scattering length distribution, an indicator function  $I(\mathbf{r})$  is defined. It is either one for all points that lay within the solid or zero for all points outside the solid [95].

Consider a lattice representation of a structure with  $N^3$  nodes. The lattice spacing is denoted as  $\delta x$ . The numerical Fourier transform of this field shall be denoted as  $A_{disc}(\mathbf{q})$ . Since there is only information on each lattice node, this is effectively the Fourier transform of a set of delta functions. To include the size of each cube, Schmidt-Rohr suggests to convolve the result with the form factor for each lattice cube, which reads:

$$F_{cube}(\mathbf{q}) = \prod_{i=1}^3 \frac{\sin(q_i \cdot \delta x/2)}{q_i \cdot \delta x/2}, \quad (3.13)$$

where  $q_i$  denotes the three components of the scattering vector. The convolution is conveniently carried out in Fourier space using the multiplication theorem:  $I(\mathbf{q}) = |F_{cube}(\mathbf{q})|^2 \cdot |A_{disc}(\mathbf{q})|^2$ . The spherically averaged scattering curve  $I(q)$  is then calculated via a radial average. The minimal value for the q-vector is then given by  $q_{min} = \frac{2\pi}{\delta x \cdot N}$ , the maximal value due to the Nyquist limit as  $q_{max} = \frac{\pi}{\delta x}$ . During the radial averaging, not all q-vectors fall on the discrete points in  $I(\mathbf{q})$ . The points between the discrete data points of the numerical Fourier transform are linearly interpolated. The first version of the algorithm was implemented in MATLAB. A Java version was developed later. Both versions can be used on up to  $512^3$  lattices using a workstation with an Intel Core i7 and 16 GB RAM.

**Verification of scattering pattern calculation** The procedure to compute small angle scattering curves was verified by comparison against a known solution. A single sphere was placed somewhere in a box with  $256^3$  voxels, the radius was varied to see the effect of the sphere resolution. The scattering curves, normalised by the spheres radius, are given in Figure 3.1 together with the analytical result for the form factor of spheres  $I(q) \propto \frac{9(\sin(qR) - qR \cos(qR))^2}{(qR)^6}$  [94].

A good agreement between the numerical form factors and the analytical results shows that the suggested procedure is valid. However, care must be taken when small angle patterns are computed due to the coarse resolution at  $q \rightarrow 0$ , which is  $\frac{2\pi}{N \cdot \delta x}$ . This may lead to features being missed. However, as Brisard and Levitz point out, domain size effects may occur in this range [61].

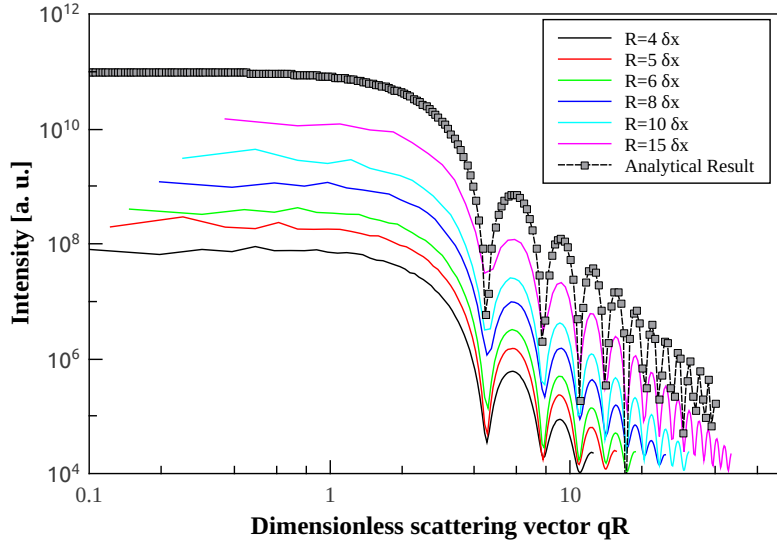


Fig. 3.1 Simulated scattering pattern of a single sphere placed in a box with  $N^{256}$  voxels. The particle radius is given in voxels. The analytical result is given by the grey squares. Even for small particle radii, the analytical result is in good agreement with the numerical data. The difference between the position of the first fringe predicted by the numerics and the analytical result is around 1 %.

### 3.4 Characterisation of transport properties of random structures

The transport properties of random porous media can be characterised by their permeability and their diffusivity. The permeability is the resistance of the medium against pressure driven flow and is defined in steady state via the empirical Darcy's law [98]:

$$\mathbf{q} = -\frac{k}{\mu}(\nabla p - \rho \mathbf{g}). \quad (3.14)$$

The flow rate per unit area is  $\mathbf{q}$  and the permeability is denoted  $k$ .  $p$  denotes the fluid pressure,  $\rho$  its density and  $\mathbf{g}$  the gravitation. The permeability depends on the porosity, the pore sizes and the connectivity between these pores. Similarly to Darcy's law, a porous media version of Fick's first law can be defined:

$$\mathbf{j}_e = -D_e \nabla c_e. \quad (3.15)$$

$c_e$  is the effective concentration of a diffusing species averaged over a porous media and  $\mathbf{j}_e$  is the effective flux per unit area. An effective diffusivity, the ratio between the effective

diffusion coefficient  $D_e$  and the free diffusion coefficient  $D_0$  of the diffusing species, can be defined for a porous medium. According to van Brakel and Heertjes, its dependence on the parameters of the porous media can be given as [99]

$$\frac{D_e}{D_0} = \frac{(1 - \varphi)\delta}{\tau_c^2}, \quad (3.16)$$

The porosity is  $(1 - \varphi)$ , and the connectivity of the pores is rationalised in the tortuosity  $\tau_c$ .  $\delta$  is the constrictivity, describing variations of the diffusion coefficient due to different pore widths.

In an experiment, both quantities are in principle easy to measure. The investigated porous sample is placed in a device able to maintain a constant driving force along the sample and the flow of fluid or the flux of tracer (for diffusion) is measured. The effective transport properties can then be calculated from Equation 3.14 or 3.15. If the transport coefficients are low, this can take a very long time. The experiment may be complicated if the sample reacts with the flowing medium or a tracer can be adsorbed on the internal surface of the porous medium. Both is the case for cement. More advanced, non-equilibrium techniques have been proposed [100].

The numerical permeability or diffusivity computation for a given structure follows the experiment. A numerical representation of the porous media is placed in the computational domain with pressure or concentration boundaries at the domain ends. Alternatively, the fluid can also be forced through the porous media by applying a body force. In this work, lattice Boltzmann is used to solve the Navier-Stokes equation and the convection diffusion equation (CDE) in the pore space. As soon as steady state has been reached, the simulation is terminated and the permeability/diffusivity is computed from the flow rate through the sample.

The obtained result is, of course, dependent on the physical model used. The lattice Boltzmann algorithms used in this work solve macroscopic fluid dynamic equations. Their solutions are self-similar for all length scales. Thus, contrary to popular belief, at least standard lattice Boltzmann methods are not capable of reproducing any nano-fluidic effects. Special boundary conditions may be required [101].

### 3.4.1 Lattice Boltzmann

The lattice<sup>1</sup> Boltzmann method is a relatively young, cellular-automaton based method of computational fluid dynamics (CFD). In this section, the general background, the algorithm

<sup>1</sup>About the capitalisation: in this work, following Wolf-Gladrow, lattice Boltzmann is written with a normal-case 'l' [102].

and program are introduced to communicate the general understanding of the method. For an overview, the reader is referred to Succi's book and Raabe's review [103, 104]. A frequently cited introduction in the mathematical background is given in the published lecture notes of Wolf-Gladrow [102]. This author found the thesis of Sani also a helpful starting point [105]. Permeability studies with lattice Boltzmann have been quite popular [106–110]. However, It has also been used for reactive flows in geology [111] and chemical engineering [112]. Algorithms for multiphase flow were also developed.

Classical CFD methods employ different mathematical methods to solve the partial differential equations describing the motion of fluid. For bulk fluid motion, this is the Navier-Stokes equation (NSE), for diffusive mass transfer this is the convection diffusion equation (CDE) [98]. The methods to solve these equations employed are typically finite-difference, finite-volume or finite-element methods. These equations are macroscopic averages of the the underlying behaviour of the parcels of fluid. Lattice Boltzmann approaches fluid behaviour from a particle perspective. Flow properties are derived from the evolution of a highly simplified model of particle dynamics, originating in the Boltzmann equation.

The basis of the lattice Boltzmann model is the lattice Boltzmann equation, which is a discrete variant of the Boltzmann equation describing the behaviour of a gas. Phase space is discretised; the spatial component  $\mathbf{r}$  as an  $n$ -dimensional lattice, the velocity component as  $N$  discrete velocities on each point in space. The lattice spacing is denoted  $\delta x$ , and time evolves in steps  $\delta t$ . The discrete velocities are  $\{\mathbf{c}_i\} = (\mathbf{c}_0, \mathbf{c}_1, \dots, \mathbf{c}_{N-1})$ . The idea is illustrated in Figure 3.2 with the lattices used in this work. The state of the gas at each lattice node is described by the discrete velocity probability density function, which is discretised as probabilities  $\{f_i\} = (f_0, f_1, f_2, \dots, f_{N-1})$ . Thus,  $f_i$  is the probability of finding a gas molecule moving in direction  $\mathbf{c}_i$ . Macroscopic variables, such as the fluid density  $\rho$  and fluid velocity  $\mathbf{u}$  are defined via the zeroth and first moment of the velocity probability density function. The evolution of the velocity probability density function is described by the lattice Boltzmann equation (LBE):

$$f_i(\mathbf{r} + \mathbf{c}_i \delta t, t + \delta t) - f_i(\mathbf{r}, t) = \Omega_i(\mathbf{r}, t). \quad (3.17)$$

The right hand side of the LBE,  $\Omega(\mathbf{r}, t)$  is the collision operator, which contains the model for the particle interactions. Each time step can be split into two algorithmic steps: the collision step in which the particle velocity distributions are altered according to  $\Omega(\mathbf{r}, t)$ , and the streaming step, in which the particles sitting at time  $t$  are moved in direction  $\mathbf{c}_i$  to the next lattice node.

The lattice Boltzmann algorithm in this work uses a discrete version of the Bhatnagar-

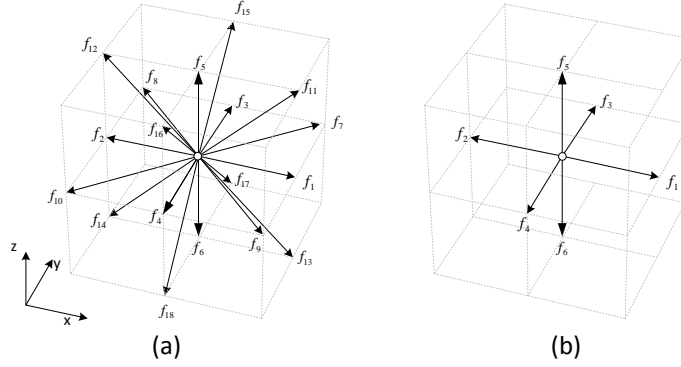


Fig. 3.2 3D visualisations of the two lattices used in this work. (a) The D3Q19 lattice used for the simulations of bulk fluid movement. (b) The D3Q7 lattice used for the simulations of mass diffusivity. The white-filled circle in the centre represents the rest channel  $f_0$ . Redrawn after Navaez and Harting [113] with changed labels.

Gross-Krook approximation, which reads

$$\Omega_i(\mathbf{r}, t) = -F (f_i(\mathbf{r}, t) - f_i^{eq}(\mathbf{u}(\mathbf{r}, t), \rho(\mathbf{r}, t))). \quad (3.18)$$

$F$  denotes the collision frequency  $\delta t/\tau$ , where  $\tau$  is the collision time. As it will be seen later,  $\tau$  controls the transport properties of the gas regarding momentum (hydrodynamic lattice Boltzmann) and mass (diffusion lattice Boltzmann).  $f_i^{eq}(\mathbf{u}(\mathbf{r}, t), \rho(\mathbf{r}, t))$  is the equilibrium velocity probability distribution. In principle, different choices for the equilibrium distribution can recover the same macroscopic behaviour, as long as the collision operator fulfils the right properties. The properties needed to reproduce certain physical behaviour are discussed in the corresponding section.

### 3.4.2 Lattice Boltzmann for the Navier-Stokes equations

A lattice Boltzmann model leading to solutions of the Navier-Stokes equation requires a collision operator which conserves mass and momentum, fulfils Galilean invariance and leads to isotropic fourth-order velocity tensors. The following equilibrium function conserves mass and momentum [102]:

$$f_i^{eq}(\rho(\mathbf{r}), \mathbf{u}(\mathbf{r})) = \omega_i \rho \left( 1 + \frac{\mathbf{c}_i \cdot \mathbf{u}}{c_s^2} + \frac{(\mathbf{c}_i \cdot \mathbf{u})^2}{2c_s^4} - \frac{\mathbf{u}^2}{2c_s^2} \right). \quad (3.19)$$

Certain symmetry requirements are imposed on the lattice to obtain the demanded isotropy of the fourth order velocity tensors. These can be ensured by using one of the lattices given by Qian [114] with appropriate lattice weights  $\{\omega_i\} = (\omega_0, \dots, \omega_{N-1})$ . The constant  $c_s^2$  is the

lattice speed of sound. The pressure is related to the density of the lattice gas via

$$p(\mathbf{r}, t) = c_s^2 \rho(\mathbf{r}, t). \quad (3.20)$$

The lattice used in this work for the lattice Boltzmann algorithm to recover the Navier-Stokes equation is the *D3Q19* lattice shown in Figure 3.2. It has 1 rest and 18 velocity channels. The macroscopic variables, such as the fluid density  $\rho$  and fluid velocity  $\mathbf{u}$  are defined via zeroth and first moments of the velocity probability:

$$\rho = \sum_{i=0}^{N-1} f_i, \quad (3.21)$$

$$\rho \mathbf{u} = \sum_{i=0}^{N-1} f_i \mathbf{c}_i. \quad (3.22)$$

The kinematic viscosity of the model is

$$\nu = c_s^2 \left( \tau - \frac{1}{2} \delta t \right). \quad (3.23)$$

The relaxation time  $\tau$  can take values  $0.5 < \tau < \infty$ .

### Boundary conditions

The boundaries of the fluid domain require special treatment, as in any other solution method for a PDE. The left-hand side of Equation 3.17 shows that for a fluid node close to the domain boundary, those parts of the velocity probability distribution function which come from outside the domain boundary remain undefined. In turn, the treatment of those velocity vectors pointing out of the domain must be specified, otherwise, the domain would "leak". This problem is outlined in Figure 3.3. The definition of a boundary condition means finding meaningful ways to specify those velocity distributions pointing inwards at the wall. Below, the different types of boundary conditions used in this work are introduced.

**Solid walls: no-slip boundary conditions** The most frequently appearing boundary conditions are no-slip boundaries at solid walls. Their simplest treatment are bounce-back boundary conditions. The principle is shown in Figure 3.3c. Those velocity probabilities streamed into the boundary nodes are inverted and returned in the next step [103, 116].

**Periodic boundary conditions** Periodic boundary conditions are a common way to realise open domains, provided that the geometry under consideration (e. g. the porous media)

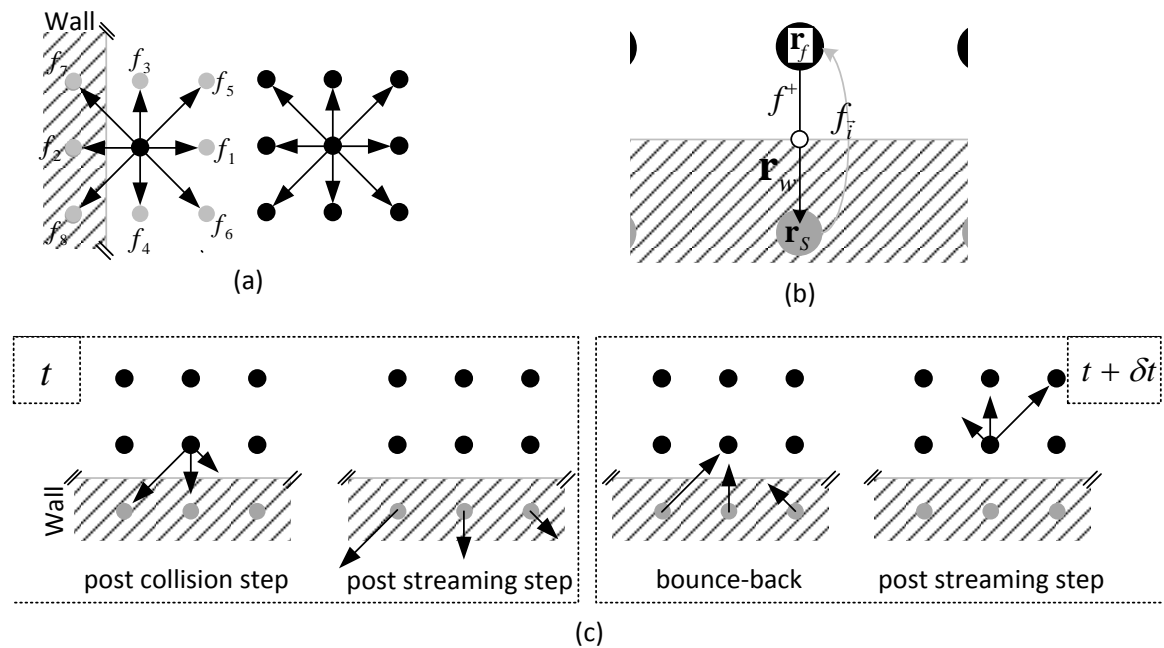


Fig. 3.3 (a) Two-dimensional illustration of the problem at the domain boundary of lattice Boltzmann domains: during an update step, the velocity distributions  $f_7, f_8$  and  $f_2$  are streamed out of the domain, whilst the  $f_5, f_1$  and  $f_6$  do not receive a new value from a cell out of the domain. (b) Illustration of the generalised boundary conditions proposed by Zhang et al. Redrawn after [115]. (c) 2D illustration of half-way bounce back boundary. Each time step consists of a collision and a streaming step (see equation 3.17). From left to right: (1) after the collision step, the velocity distributions aiming for the wall are shown. Their values are represented by the different lengths. (2) The streaming step moves them into the wall nodes. Note that time increments by  $\delta t$ . During the collision phase of this step, the wall particle velocity distributions are reversed. (4). The streaming step returns the velocity distributions in the domain. The grey line shows the effective wall position half-way between the wall nodes and the fluid nodes. Redrawn and modified after Sukop and Thorne [116]

is periodic too. They can be implemented by inserting those velocity probabilities leaving the domain at the opposite site, and vice versa.

**Pressure boundary conditions** Consider a pressure boundary in the positive  $x$ -direction. Then, as shown in Figure 3.2a, the velocity distributions  $\{f_2, f_8, f_{10}, f_{12}, f_{14}\}$  are unspecified after the streaming step. The idea, first developed by Zou and He for  $D2Q9$  and  $D3Q15$  lattices and extended to  $D3Q19$  lattices by Hecht and Harting [117, 118] is as follows: the relationship between the velocity probability distributions and their first and zeroth moments, namely  $\rho$  and  $\mathbf{u} = \{u_x, u_y, u_z\}$ , is linear. Due to the continuity equation, one of these moments is dependent on the other three. This leads to an under-determined system of three equations and five unknowns. By assuming bounce-back for the non-equilibrium part of the outgoing particle velocity probability distributions and the introduction of two extra variables, the transversal velocities, the system of equations can be balanced. As a result, a density can be specified at the domain boundary which is related to the pressure via the lattice gas equation of state. Velocity boundary conditions can be defined by the same approach.

### 3.4.3 Lattice Boltzmann diffusivity scheme

Shortly after the first lattice Boltzmann methods hydrodynamic simulations appeared, it was recognised that LB can also be used as a solver for the convection diffusion equation [119–121]. Its application for characterising the diffusivity of porous media has also been proposed previously by different authors [122, 123]. The CDE requires only mass but not momentum, to be conserved by the collision operator. Additionally, the symmetry requirements on the underlying lattice for recovering diffusion are less than those for the Navier-Stokes equation. In this work, a Cartesian  $D3Q7$  lattice with six velocity channels and one rest channel was used, as shown in Figure 3.2b. This reduces the memory demand and increases the code performance.

The CDE equation can be recovered from a lattice Boltzmann scheme if the equilibrium distribution function reads

$$f_i^{eq} = c\omega_i(1 + K_i\mathbf{u}_B \cdot \mathbf{c}_i). \quad (3.24)$$

The velocity of the fluid, in which the species diffuses, is denoted as  $\mathbf{u}_B$  and  $K_i$  is a lattice dependent constant. In this work, only pure diffusion has been investigated, therefore  $\mathbf{u}_B = 0$ . The particles described by the velocity probability density distribution are now interpreted as particles of the diffusing species. Thus, the concentration of particles is the zeroth moment and the flux the first velocity moment of the particle velocity probability

distribution:

$$c = \sum_i f_i \quad (3.25)$$

$$\mathbf{j} = \frac{\tau - 1/2}{\tau} \sum \mathbf{c}_i f_i \quad (3.26)$$

Note the  $\tau$ -dependent term  $\frac{\tau - 1/2}{\tau}$  in the definition of the flux of the diffusing species. The diffusion coefficient in this model is

$$D = c_s^2 \left( \tau - \frac{1}{2} \delta t \right). \quad (3.27)$$

Again, the relaxation time can take values between  $0.5 < \tau < \infty$ .

### Boundary conditions

The principle difficulty in treating the boundary conditions is the same as for the Navier-Stokes solver. Sources and sinks for the diffusing species are simulated with concentration or flux boundaries. One also may be interested in simulating global or local decaying processes of the diffusing species, for example, if one is interested in reacting systems. Finally, on passive solid surfaces a no-flux boundary is needed. In this work, generalised boundary conditions are used as described by Zhang et al. which can represent the general boundary condition [115]:

$$b_1 \nabla c \cdot \mathbf{n}|_{\mathbf{r}_w} + b_2 c = b_3. \quad (3.28)$$

$\mathbf{n}$  denotes the surface normal vector, and  $\mathbf{r}_w$  the position of the boundary. These definitions are shown in Figure 3.3. The idea is to define a fictitious wall concentration  $c_{w,i}$  on the boundary node, which is defined for each channel. Its value is chosen by linear extrapolation so that the boundary condition is maintained. The velocity distribution functions  $f_i^-$  streamed in the simulation domain from outside the wall are then

$$f_i^-(\mathbf{r}_f, t + \delta t) = f^+(\mathbf{r}_f, t) + 2\omega_i c_{w,i}. \quad (3.29)$$

$f^+(\mathbf{r}_f, t)$  denotes the velocity distribution that was streamed in the wall from the fluid node. For a concentration boundary condition, the wall concentration  $c_{w,i}$  is the concentration on the boundary. For other types of boundary condition, the concentration gradient at the boundary is computed using the following finite-difference scheme:

$$\nabla c \cdot \mathbf{n}|_{\mathbf{r}_w} = \frac{c_f - c_{w,i}}{-0.5(\mathbf{n} \cdot \mathbf{c}_i) \delta x}. \quad (3.30)$$

Here,  $c_f$  is the concentration on the fluid node next to the wall node. Please note that the factor 0.5 comes from the fact that the flux is evaluated half-way between the fluid and the boundary node. Inserting the finite difference in Equation 3.28 leads to

$$c_{w,i} = \frac{c_f + 1/2\delta x(\mathbf{n} \cdot \mathbf{c}_i)b_3/b_1}{1 + 1/2\delta x(\mathbf{n} \cdot \mathbf{c}_i)b_2/b_1}. \quad (3.31)$$

For no-flux boundary conditions on solid surfaces, one has  $b_2 = b_3 = 0$  and, thus,  $c_{w,i} = c_f$ .

During the verification of the code, it was shown that for  $\tau = 1$ , these boundary conditions work very well. For  $\tau \neq 1$ , deviations were observed. For steady state simulations, errors of the order of 10% were found. The test for a non-steady state, as shown below, has revealed that these boundary conditions are not mass conserving.

### 3.4.4 Conversion between the lattice and the real world

In lattice Boltzmann, all lengths are discretised by the lattice spacing  $\delta x$  and time is discretised as time steps  $\delta t$ . These define via relaxation time  $\tau$  the viscosity of the lattice fluid, as seen in Equation 3.23. A more detailed discussion is given in Succi's book [103].

### 3.4.5 Implementation

The lattice Boltzmann schemes used in this work were implemented in C. Their performance using only a single CPU core was optimised using the the recipes suggested by Wellein et al. and Zeiser [124, 125]. These include, among others, the rolling out of short loops and adjusting the looping through the arrays to archive cache coherence.

The permeability scheme was implemented using the message passing interface (MPI) library. MPI allows communication between different processes on the same system and is a standard programming tool for parallel programming. Efficient parallelisation of lattice Boltzmann code is a research topic on its own [125]. The parallelisation programmed by this author splits the domain along one spatial dimension and uses the ghost node technique [126].

### 3.4.6 Verification

#### Verification of the permeability code

The permeability code was verified in two stages. In the first stage, its ability to successfully predict the permeability of a laminar flow through a cubic channel was confirmed. Cubaud

et al. give an analytical result for Poiseuille-like flow through through a square channel with height  $h$ :

$$\mathbf{q} = -\frac{h^2}{A\mu} (\nabla p) - \rho \mathbf{g}. \quad (3.32)$$

$A = 28.43$  is a geometric constant [127]. On a cubic lattice, a square channel aligned with the lattice has smooth walls. To estimate the effect of rough walls on the lattice Boltzmann results, simulations in channels aligned with and rotated towards the underlying lattice by  $45^\circ$  were compared. The rotated channel was omitted for the second generation of code. The geometry is shown in Figure 3.4. In the second verification step, the permeability of an

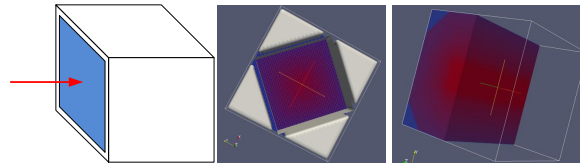


Fig. 3.4 Left: illustration of the square channel geometry used to verify the lattice Boltzmann code. The inlet and outlet of the channel had periodic boundary conditions. Centre and right: smoothed velocity fields along a cross section through the channel with 20 (rotated) and 4 lattice nodes height.

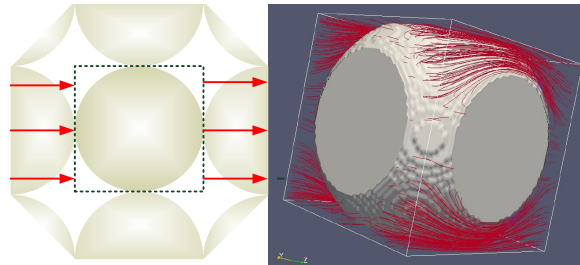


Fig. 3.5 Left: 2D illustration of the periodic cubic arrays of spheres used to verify the lattice Boltzmann code. The length of the dotted line is the box size. Right: 3D example flow field for a solid volume fraction of about 0.8.

infinite cubic array of spheres is calculated for different sphere radii, allowing one to tune the solid volume fraction. This procedure was proposed by Zalzale and McDonald [128]. An example of this geometry is shown in Figure 3.5. analytical results for the permeability of these arrays were given by Larson and Higdon [129]. If one maps a sphere on a lattice with finite-sized voxels, the volume of the sphere on the lattice will be slightly different to the actual volume of the sphere due to discretisation effects. This was taken into account when the lattice Boltzmann results were compared against the results of Larson and Higdon by linearly interpolating the latter to the exact volume fractions of the sphere on the lattice.

The two situations resemble well the two main geometries under consideration in this thesis: the square channel is similar to the sheets studied in Chapter 5 and 6, whilst the cubic array is a special case of the particle packings considered in Chapter 3.

The results for flow through a square channel aligned with the lattice is shown in Figure 3.6. For channel widths of one and two lattice nodes, the error is about 15 %. For a channel width of four it is about 7 %. The error decreases approximately as 2nd order in space, similar to Sengupta's et al. results who forced the flow by a body force [130].

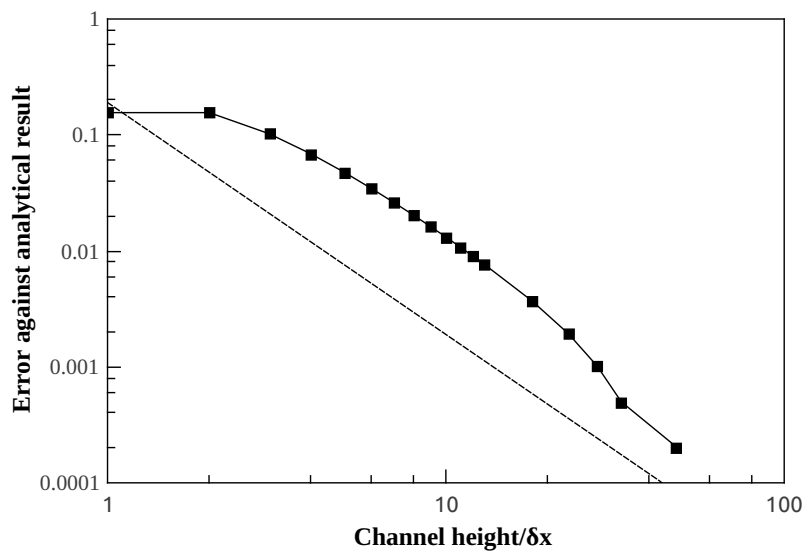


Fig. 3.6 Error of the lattice Boltzmann simulation of flow in a square channel carried out with the second generation permeability scheme. The dashed line indicates a second order decay.

In Figure 3.7, the error of the lattice Boltzmann permeability predictions of a cubic array of spheres against the literature value is shown. The error is plotted against the size of the cubic lattices' elementary cell. The maximum error reported for a box size of only eight is about 38 %. Box sizes between eight and twenty were sampled in great detail, and the error decreases considerably to less than 10 % for all cases investigated for a box size of twenty. Within the detailed region, strong fluctuations in the accuracy are observed. These fluctuations are probably due to discretisation effects of the sphere, leading to a slightly different-shaped form for each structure with a set box-size and specified volume fraction.

### Verification of the diffusivity code

Initial tests for the diffusivity code were run for diffusion in a small channel, similar to the one carried out for the permeability code (see Section 3.4). Concentration boundary

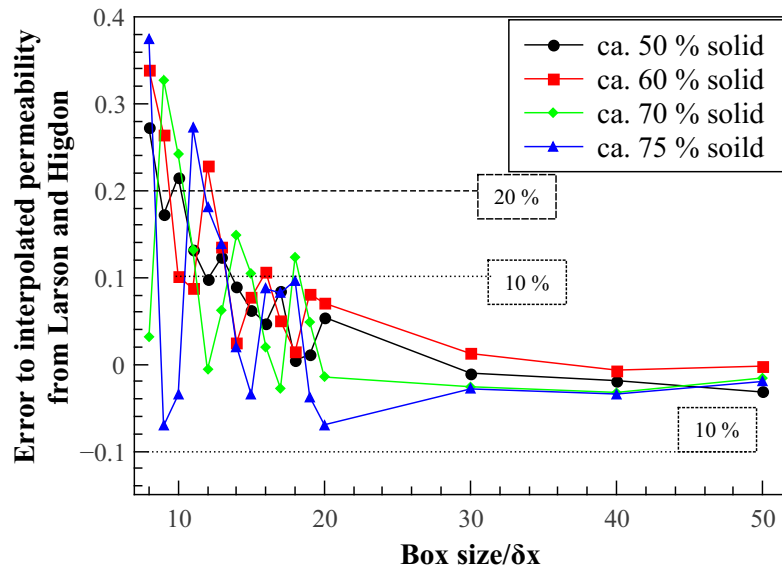


Fig. 3.7 In this Figure, the error of lattice Boltzmann simulations for cubic array of spheres to the result of Larson and Higdon is plotted versus the size of the simulation box [129].

conditions were used at the inlet and the outlet of the channel. This procedure is equivalent to the channel flow employed for the Navier-Stokes solver. Even for channel heights as small as just two lattice nodes, a broad range of relaxation times led to the recovery of the correct diffusion coefficient.

As a second method of verification, a more ambitious problem was chosen. Berezhkovskii et al. studied a trapping problem in the geometry shown in Figure 3.8. It consists of two connected pipes radii  $R_1$  and  $R_2$ , with  $R_1 > R_2$ . The diffusion coefficients in the segments are labelled  $D_1$  and  $D_2$ , correspondingly,  $\tau_1$  and  $\tau_2$  denote the relaxation times for the lattice Boltzmann algorithm in the pipe segments. The wider end is sealed and the second pipe is terminated by a particle sink. At  $t = 0$ , a tracer is only present at the wall to one end of the pipe, which is closed. As time progresses, the tracer diffuses through the pipe and escapes through the open end. This can be described by the lifetime  $T$  of the tracer within the system, which is defined as

$$T = \frac{\int_0^\infty t \frac{dm}{dt}(t) dt}{\int_0^\infty m(t) dt}, \quad (3.33)$$

where  $m(t)$  is the overall amount of tracer in the domain at time  $t$ . The analytical solution

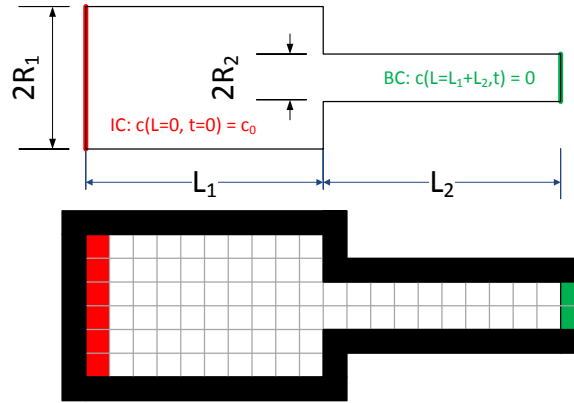


Fig. 3.8 Upper diagram: sketch of the geometry used for the verification of the diffusion code. Red: initial condition  $c(L=0, t=0) = c_0$ . Green:  $c(L_1 + L_2, t) = 0$  boundary condition. Black: no-flux boundary condition. Below: translation of the geometry into a lattice. In contrast to the analytical description, the initial condition has a finite width, which leads to errors when the total length becomes very small.

given by Berezhkovskii reads

$$T = \frac{L_1^2}{2D_1} + \frac{V_1}{4R_2 D_1 f(v)} + \frac{L_2 V_1}{\pi R_2 D_2} + \frac{L_2^2}{2D_2} \quad (3.34)$$

The term  $V_i = \pi R_i^2 L_i$  is the volume of segment  $i$ , and  $f(v)$  is a boundary homogenisation factor depending on the ratio between the radii  $v$ , as defined in their manuscript [131].

In Figure 3.9 two example lifetime spectra are shown. The spectrum for  $\tau \neq 1$  shows that the boundary conditions are not mass conserving. This leads to errors in the lifetime of factors between 0.5 and 3, for the values of  $\tau$  studied. It was decided to avoid the problem by avoiding running simulations with  $\tau \neq 1$ . The good accuracy of the code for reasonably sized systems was demonstrated by varying radii and pipe lengths. The results are shown in Figure 3.10. If lengths were resolved by more than three lattice spacings, an error of less than 10% was observed.

As a second verification, the results of the diffusion code were directly compared against a random walk algorithm developed by Churakov [132]. For simulations with  $\tau = 1$ , the error was generally less than 5% for particle packings. The comparisons showed that for  $\tau \neq 1$  the errors were of a magnitude of 10%, which suggests that the imperfect mass conservation is not as drastic for steady state.

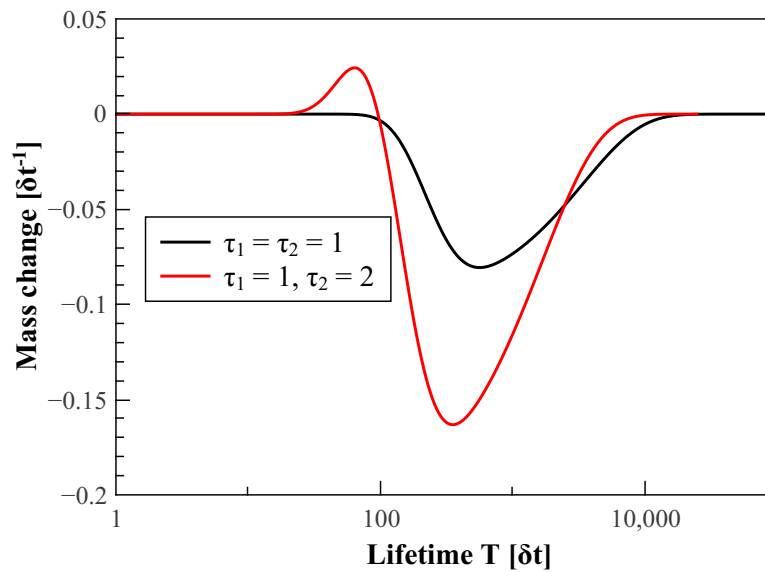


Fig. 3.9 Lifetime spectra  $\frac{dm(t)}{dt}$  for two different runs. For  $\tau = 1$ , the amount of the diffusing species remains constant until the sink is reached. For  $\tau_2 = 2$ , mass is gained when the diffusing species reaches the narrower part of the pipe. This is due to the finite difference scheme for the boundary conditions, which is not exactly mass conserving.

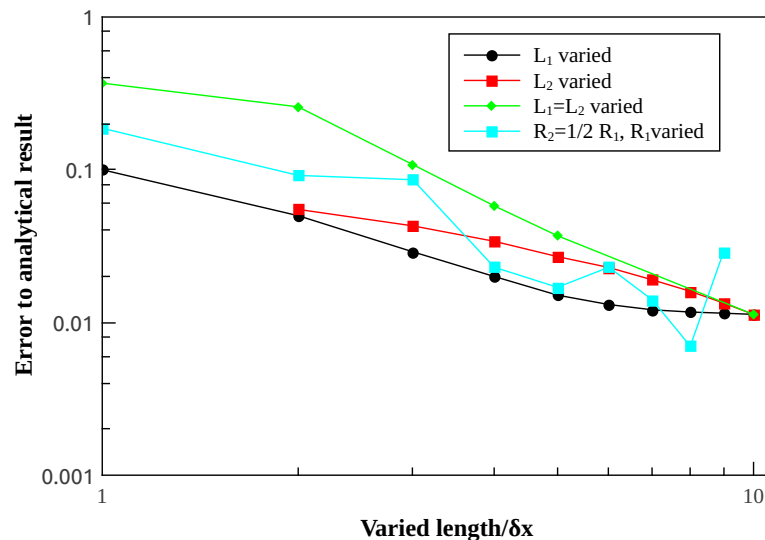


Fig. 3.10 Effects of the radial as well as axial resolution on the error towards the analytical result. The base system had  $l_1 = l_2 = 10 \delta x$  and  $R_1 = R_2 = 10 \delta x$ . The relaxation times were 1 in both pipe segments.

## 3.5 Conclusions

In this work, the backgrounds to the methods used in the thesis were given and the algorithms developed and verified by following largely literature examples. This procedure has been completed largely successfully. For the diffusion algorithm, it was not successful to implement mass conserving boundary conditions for  $\tau \neq 1$  as no-flux boundary condition. Whilst the error seemed to be within the acceptable range for steady state simulations, it was not acceptable for non-steady state simulations. Thus, it was decided to calculate all results presented in this thesis with  $\tau = 1$ .



# Chapter 4

## Simple particle model for the transport properties of C–S–H

Simple particle packings were studied as a transport model for the meso-scale of calcium-silicate-hydrate in cement. Particle packings of spherocylinders were generated using a relaxation algorithm. The transport properties and scattering curves of these simple models were compared to experimental data for cement paste. It was found that the transport properties of mature cement paste cannot be explained using the particle models presented.

### 4.1 Introduction

Currently, 11 billion tons of concrete are produced annually [9]. Most of it is Portland cement concrete, accounting for 5-8 % of mankind's carbon dioxide emission. In these materials, Portland cements and its blends are the glue holding a matrix of aggregates together. The need for understanding the long-term durability drives fundamental research into the processes of concrete corrosion. All corrosive processes in concrete are connected to the state of water in the material. Therefore, moisture transport in cementitious materials is an important field of study [21].

Cement paste is made by mixing cement powder and water. Hardened cement paste has three different pore systems, if voids from cracking during hardening are ignored: the capillary pores (1 to 100  $\mu\text{m}$ ), gel pores (1 to 12 nm [4]) and the interlayer pore space ( $\approx$  1 nm). The last two types of pores are located within the calcium-silicate-hydrate phase, the most important hydration product of Portland cement. It controls most of the properties of the hardened material. It was proposed that the systems of small pores in calcium-silicate-

hydrate control the transport properties of hardened cement paste if the capillary pore space depercolates [2, 133].

The arrangement of solid within C–S–H on the meso scale, that is from 1 nm to 100 nm, is the subject of an ongoing debate [22, 37, 38, 134]. It is dominated by two points of view: in the sheet model, based on the work of Feldman and Sereda, C–S–H is described as a disordered sheet structure. The interlayer space is the void space between aligned sheets, and the gel pore spaces are defects in the sheet structure [5, 6]. The other school of thought sees the hydrate as a colloidal aggregate of particles with an approximate diameter of 5 nm [3]. In the most recent version of this model, the particles have an internal layered structure which contains the interlayer pore space. The gel pore space is described as the space between the particles [4]. A more thorough discussion can be found in Chapter 2.

In this chapter, the transport properties of the most simple model of colloidal particles is investigated. This is a packing of monodisperse particles. Spherocylinders were chosen to be able to tune the solid volume fraction of the packing via the aspect ratio of the particles. Transport properties refer to the effective diffusion coefficient and permeability of the pure phase. In addition to transport properties, the scattering curve of the particle packings is also calculated and compared against literature data for C–S–H. The reasoning behind calculating a scattering curve for the model is the requirement of consistency: a transport model cannot just explain the transport properties; it also has to agree with other observations made on calcium-silicate-hydrate.

The chapter is organised as follows: in the next section, literature values for the transport properties of calcium-silicate-hydrate in cement are reviewed. Subsequently, the simple colloidal model is introduced. The procedures used to generate the particle model structures and to compute the transport properties are presented in Section 4.2. After presenting the results, the chapter concludes with a discussion.

### 4.1.1 Transport properties of C–S–H in cement paste

Transport properties in this chapter are defined as the effective (water) permeability of C–S–H, denoted as  $k$ , and the effective water self-diffusion coefficient in the C–S–H structure, denoted as  $D_e$ . This is also expressed as diffusivity  $D_e/D_0$ , where  $D_0$  denotes the diffusion coefficient of bulk water, measured as  $2.3 \times 10^{-9} \text{ m}^2 \text{ s}^{-1}$  by Mills et al. [135].

Neither value is directly accessible by experiment, since C–S–H in cement paste always coexists with other phases. These are crystalline solids, which are likely to be impermeable, and the capillary pores. Whilst synthetic C–S–H analogues have been used as model systems to study the chemistry and water removal [27, 136, 137], it is not clear whether the pore system in synthetic C–S–H is comparable to those in cement paste. The author of this thesis

is not aware of any study investigating transport properties of synthetic C–S–H.

The fact that C–S–H in cement paste always coexists with other phases raises the problem of how transport properties of the model structures for C–S–H can be compared to the measured transport properties, which are always given (except Powers' value, Table 4.1: row 1) for cement or alite paste. The effect of the coexisting phases in cement paste is estimated as follows: according to Muller et al. [40], the volume fraction of calcium-silicate-hydrate (solids, interlayer water and gel pore water) in almost completely hydrated white cement paste at a water-to-cement ratio of 0.4 is about 60 %. Furthermore, approximately 10 % of the volume are larger voids, and roughly 30 % are supposedly impermeable solids, such as unhydrated cement, crystalline portlandite and ettringite. The presence of the larger voids is ignored for the moment. Assuming a simple model for the spatial distribution of solids, using the continuum percolation model of overlapping spheres [138, 139], suggests a sample spanning cluster of C–S–H. This is because the C–S–H volume fractions exceeds the percolation threshold for this model of approximately 28.5 %. Thus, one can assume that transport in C–S–H is in parallel to transport through the other phases. Since the C–S–H volume fraction of paste is about 60 %, the influence on the transport properties is at most a factor of two, which is omitted in the subsequent discussion.

However, care must be taken since larger voids are present. At least for permeability, their contribution is expected to be large due to their larger pore sizes. One can assume again a continuum percolation model of overlapping spheres for the solid phases with the 10 % larger pores in between. The percolation threshold for these pores is a solid fraction of about 96 % for this model [140]. This indicates that the large pores may still contribute to the transport properties in such a system. The larger voids are of considerable size and may dominate transport as long as they do not depercolate. Using a more detailed model for cement paste, Zalzal et al. showed that the larger pore spaces indeed depercolate for mature systems. Thus, only the lowest transport coefficients for the most mature samples were taken as controlled by transport through C–S–H [133].

Transport data from literature is compiled in Tables 4.1 and 4.2. In both cases, a considerable spread of the transport coefficients obtained for different samples by different investigators is apparent. If the permeability values provided in literature are considered, a general trend that the older or more hydrated the samples are, the the lower the reported value, is found. The lowest value is given by Powers, who gave C–S–H a permeability of  $7 \times 10^{-23} \text{ m}^2$ . Only Cui et al. reported a lower value, which was the permeability of cement paste as a whole. Other authors like Nyame et al. or Odler et al. reported values of at least half a magnitude larger. In Chapter 2, it is discussed how the chemical composition of C–S–H can vary between different samples, which could also affect the permeability.

Therefore, it is reasonable to assume that the permeability of C–S–H varies over a considerable range. The permeability of C–S–H is therefore assumed to be in the order of  $5 \times 10^{-22}$  to  $5 \times 10^{-23} \text{ m}^2$ .

Table 4.2 shows self-diffusion coefficients of tritiated water. The situation appears to be similar to permeability data. The reported values show a large spread. The water self-diffusion coefficient seems to decrease as the water-to-cement ratio decreases. Also, older samples seem to have lower diffusivities. Some of the reported diffusion coefficients were calculated allowing for the adsorption of the tracer on the surfaces in the sample. The lowest diffusivities reported were obtained by Delagrave et al., being in a range from  $3 \times 10^{-4}$  to  $4 \times 10^{-3}$ . However, Tits et al. found a diffusivity almost 500-times larger than Delagrave et al. for a sample of similar  $w/c$ -ratio and comparable age. In fact, the sample used by Tits et al. is more mature, so one expects a lower value. The difference between both cases is that Tits et al. analysed their experiment by taking surface adsorption into account, whilst Delagrave et al. did not. Interestingly, Delagrave et al.'s results for  $w/c=0.45$  agree with those from Yamagouchi et al. for similar samples. It is difficult to decide which reported diffusivities are to be believed. Since the majority of the diffusion coefficients is of order  $2 \times 10^{-12} \text{ m}^2 \text{ s}^{-1}$ , it is assumed here that the diffusion coefficient of water in C–S–H is of the same order of magnitude.

### 4.1.2 Building a model for the meso-structure of C–S–H

Powers suggested a particle size of about 5 nm for his colloidal model. The interstitial space formed the gel pore space [2]. The more recent Jennings model keeps this idea, but the particles have a fine internal structure containing interlayer pore space [4].

The popular Jennings model describes the structure as a hierarchical particle packing with two different types of gel pore sizes: small gel pores between 1 nm to 3 nm in size and large gel pores from 3 nm to 12 nm. Depending on which of these pores is taken into account, the volume fraction of solids varies from 75 % (if only small gel pores are included) towards 59 % (if large gel pores are included) [3, 4]. Muller et al. measured with  $^1\text{H-NMR}$  relaxometry a dominant pore system with a characteristic size of 2 nm, which has a solid content of 53 % [40]. Different solid fractions for the gel pore system of C–S–H are also summarised in Table 4.3

The proponents of the particle model [3, 18, 57] have speculated that the meso-structure of C–S–H may form via a diffusion-limited aggregation mechanism. Recently, elaborate models have proposed how such structures may form in the condition of a hydrating cement system [81, 82]. In this work, details of the structure formation are neglected, and a simple packing of monodisperse particles is used. Since some of the volume fractions listed in

Table 4.1 Literature values for permeabilities of cement paste (if not stated otherwise) which might be used to estimate the permeability of calcium silicate hydrate gels. Note also that Power's value (# 1) gives the permeability for pure C–S–H, not for cement paste. Notes: Conv. denotes a conventional permeability test, BB a beam bending test, DP a dynamic pressurisation test.

#	w/c	$\alpha$ [%]	Age [days]	Permeab. [ $\times 10^{-18} \text{m}^2$ ]	Source	Notes
1	n. a.	n. a.	n. a.	$6.9 \times 10^{-5}$	Powers [2]	C–S–H
2	0.4	45		0.85	Halamicckova et al. [141]	Conv.
3	0.4	50		0.15		
4	0.4	55		0.025		
5	0.4	60		$4.3 \times 10^{-3}$		
6	0.25		28	0.038		
7			182	$3 \times 10^{-3}$		
8	0.36		28	0.025		
9			182	0.01		
10	0.23		7	0.08	Nyame et al. [143]	Conv.
11			$\approx 600$	$3.7 \times 10^{-4}$		
12	0.47		3	500		
13			$\approx 600$	$7 \times 10^{-4}$		
14	0.3		28?	$3.25 \times 10^{-4}$	Odler et al. [144]	Conv. (alite)
15	0.4			$3.31 \times 10^{-3}$		
16	0.5			$7 \times 10^{-3}$		
17	0.45			0.63		
18	0.5			0.776		
19	0.6			6.38		
20	0.3	53	7	$2.66 \times 10^{-3}$	Cui et al. [145]	Conv.
21		73.2	210	$< 2.69 \times 10^{-5}$		
22	0.4	69	7	$8.1 \times 10^{-3}$		
23		85	35	$3.47 \times 10^{-4}$		
24		93	210	$1.22 \times 10^{-4}$		
25	0.4		3	0.003-0.004	Vadakan et al. [100]	BB
26	0.4		9	0.0003		
27	0.4		5	0.005	Grasley et al. [146]	DP
28	0.4		11	0.0012		

Table 4.2 Diffusion measurements reported for water tracers in cement paste. Notes: T denotes a tritiated water test, +cap denotes if the surface adsorption of the tracer was taken into account.

#	w/c	$\alpha$ [%]	Age [days]	$D_e$ [m <sup>2</sup> s <sup>-1</sup> ]	$D_e/D_0$	Source	Notes
0	1/3		180	$2.85 \times 10^{-10}$	0.12	Tits et al. [147]	T+cap
1	0.25		90	$6.9 \times 10^{-13}$	$3 \times 10^{-4}$	Delagrave et al. [148]	T
2	0.45		90	$9.83 \times 10^{-12}$	0.0043		T
3	0.45	100	50	$1.5 \times 10^{-11}$	0.0065	Yamagouchi et al. [149]	T
4	0.6	100	50	$4.6 \times 10^{-11}$	0.02		T
5	0.4		28	$5.1 \times 10^{-11}$	0.022	Numata et al. [150]	T+cap
6	0.55		28	$3.8 \times 10^{-11}$	0.017		T+cap

Table 4.3 Compilation of different solid fractions of C–S–H models and measured taken from literature.

Source	Comment	Solid fraction $\phi$ %	Associated length scale
Jennings 2000 [3]	LD-C–S–H	72	-
	HD-C–S–H	87	
Jennings 2008 [4]	vicinity of globule	75	5 nm
	•	70	8 nm
	"greater scale"	64	
	"including LGP"	59	
Muller et al. [67]	NMR	53	4.3 nm (pore height)



and rotational movement on each particle. In each iteration, this procedure reduces the particle overlap and the packing expands. In the sections below, the necessary computations are described in detail.

### Particle overlap

The particles are represented by their position  $\mathbf{r}_i$  and their orientation  $\mathbf{O}_i$ . The orientation vector is normalised to the half-length of the particle,  $|\mathbf{O}_i| \equiv \frac{1}{2}L$ . The particle's radius is denoted by  $R$ . The overlap between two particles  $i$  and  $j$  is defined as

$$\delta_{ij} = 2R - d_{min}. \quad (4.1)$$

$d_{min}$  is the minimal distance between the lines connecting the centres of the half-sphere caps. In Figure 4.1 one can see that the overlap is positive if the particles do overlap and is negative if they do not. Here, a negative overlap is not considered and set to zero<sup>1</sup>. As a control parameter to evaluate the progress of the algorithm, a mean overlap is defined as

$$\bar{\delta} = \frac{1}{N} \sum_{i \neq j}^{N,N} \delta_{ij}. \quad (4.2)$$

As soon as  $\bar{\delta} \leq \frac{1}{100}R$ , the packing is considered relaxed.

### Inter-particle forces

In order to reduce  $\delta_{ij}$ , the force has to act along the vector  $\mathbf{D}_{ij}$  between the closest points,  $\mathbf{C}_{ij}$  and  $\mathbf{C}_{ji}$ . The magnitude of the separating force is given by the overlap:  $|\mathbf{D}_{ij}| = \delta_{ij}$ .

In order to find the overlap between two spherocylinders, the directions of the forces and their contact points, the backbones of the spherocylinders are described as two parametric lines:

$$\mathbf{P}_i(s_i) = \mathbf{r}_i + s_i \mathbf{O}_i, \quad (4.3)$$

$$\mathbf{P}_j(s_j) = \mathbf{r}_j + s_j \mathbf{O}_j, \quad (4.4)$$

$$|s_i|, |s_j| \leq 1. \quad (4.5)$$

The last condition given in Equation 4.5 ensures that only points on the backbone of the spherocylinder are included. The closest point is  $\mathbf{C}_{ij} = \mathbf{P}_i(s_{cij})$ , where  $s_{cij}$  is the parameter

<sup>1</sup>If a negative overlap were allowed, it would cause an attractive force between the particles. This was explored but has always resulted in stability problems.

value for the closest points between  $i$  and  $j$  in  $i$ . It is worth noting that the geometric properties of the spherocylinders are included at two different points. Whilst the radius is included by the definition of the overlap in Equation 4.2, their length is included when the distance between two of them is calculated.

For the first step, Condition 4.5 is ignored. The problem reduces to the distance and the closest point of two lines in space.  $s_{cij}$  and  $s_{cji}$  can be found by solving the linear equations

$$\mathbf{D}_{ij} \cdot \mathbf{O}_i \equiv 0, \quad (4.6)$$

$$\mathbf{D}_{ji} \cdot \mathbf{O}_j \equiv 0, \quad (4.7)$$

where  $\mathbf{D}_{ij} = \mathbf{C}_{ij} - \mathbf{C}_{ji}$ . This leads to two values for  $s_{cij}$  and  $s_{cji}$ . Now, Condition 4.5 is imposed. If  $s_{cij}$  and  $s_{cji}$  are within  $\pm 1$ , the corresponding point on the spherocylinders backbone is calculated using Equations 4.3 and 4.4. If  $s_{cij}$  or  $s_{cji}$  exceeds  $\pm 1$ , they are set accordingly either to 1 or to  $-1$ . The problem reduces then to the closest distance between a point and a line in space, which can be found by solving

$$\mathbf{D}_{ij} \cdot \mathbf{O}_i \equiv 0. \quad (4.8)$$

with either  $s_{cij}$  or  $s_{cji}$  set. With these known, the direction of the force is

$$\mathbf{D}_{ij} = \mathbf{C}_{ij} - \mathbf{C}_{ji} = \mathbf{P}_i(s_{cij}) - \mathbf{P}_j(s_{cji}) = -\mathbf{D}_{ji}. \quad (4.9)$$

The magnitude of the force is normalised by the overlap,  $|\mathbf{D}_{ij}| = |\mathbf{D}_{ji}| = \delta_{ij}$ . This removes the overlap completely.

As indicated in Figure 4.1, two relaxation modes are available for anisotropic particles: rotation and translation. Each overlap results in a displacement  $\mathbf{D}_{ij}$  and a torque  $\mathbf{M}_{ij} = \mathbf{C}_{ij} \times \mathbf{D}_{ij}$ . The translational and the rotational displacement are obtained by summing over all overlaps between particles:

$$\mathbf{D}_i = \alpha \sum_j \mathbf{D}_{ij}, \quad (4.10)$$

$$\mathbf{M}_i = \beta \sum_j \mathbf{M}_{ij}. \quad (4.11)$$

The parameters  $\alpha$  and  $\beta$  can, in principle, be freely chosen. Their choice affects the resulting packing densities.

### Update of Positions

The update of the particle positions is proportional to the restoring force in each iteration. Accordingly, for the change in the particle's position one uses

$$\Delta \mathbf{r}_i = \frac{1}{2} \mathbf{D}_i. \quad (4.12)$$

The angular displacement  $\theta$  around the axis  $\hat{M}_i$  is

$$\theta = \frac{1}{2} |\mathbf{M}_i| \quad (4.13)$$

To rotate the orientation vector  $\mathbf{O}_i$  around  $\hat{M}_i$ , the appropriate rotation matrix is needed. This can be found by the method of quaternions [154]. They are an extension of the complex number system and can be efficiently used to describe rotation in space [154]. The rotation is represented by a four dimensional vector  $\hat{\mathbf{q}} = [q_1, q_2, q_3, q_4]^T$ , whose components are:

$$q_1 = \hat{M}_1 \sin(\theta/2), \quad (4.14)$$

$$q_2 = \hat{M}_2 \sin(\theta/2), \quad (4.15)$$

$$q_3 = \hat{M}_3 \sin(\theta/2), \quad (4.16)$$

$$q_4 = \cos(\theta/2). \quad (4.17)$$

Knowing the quaternions, the Euclidean rotation matrix  $R(\hat{\mathbf{q}})$  is given as [154]:

$$R(\hat{\mathbf{q}}) = \begin{pmatrix} q_0^2 + q_1^2 - q_2^2 - q_3^2 & 2q_1q_2 - 2q_0q_3 & 2q_1q_3 + 2q_0q_2 \\ 2q_1q_2 + 2q_0q_3 & q_0^2 - q_1^2 + q_2^2 - q_3^2 & 2q_2q_3 - 2q_0q_1 \\ 2q_1q_3 - 2q_0q_2 & 2q_2q_3 + 2q_0q_1 & q_0^2 - q_1^2 - q_2^2 - q_3^2 \end{pmatrix} \quad (4.18)$$

Then, the new orientation  $\mathbf{O}_i'$  is given by

$$\mathbf{O}_i' = R(\hat{\mathbf{q}}) \mathbf{O}_i. \quad (4.19)$$

These are the underlying ideas of the particle packing algorithm used to generate the structures used in this chapter.

### Algorithm

The following pseudo-code illustrates the algorithm based on the algebra presented above:

---

```
double **r; //position vector for all particles
```

```
double **M; //angular momenta for iteration
double **D; //force for iteration
double Delta; //average overlap

Collide(i,j)
{
    Compute s1 and s2 for the two line problem

    if(abs(s1)>Length)
    {
        s1 = sign(s1)*Length;
        s2 = Compute s2 for the line and point problem
        if(abs(s2)>Length
            s2 = sign(s2)*Length;
    }
    if(abs(s2)>Length)
        analogue to s1;

    Compute Pi(scij) and Pj(scji);
    Compute Dij=-Dji via Pi(scij)-Pj(scji);
    Compute Overlap;
    Delta+=Overlap;
    Compute Mij, Mji;
}

OneIteration()
{
    EraseIterationVariables(); //M,D,Delta
    Compute forces and angular momenta
    for(i=0; i<NumberOfParticles; i++)
        for(j=i; j<NumberOfParticles; i++)
            Collide(i,j);
    for(i=0; i<NumberOfParticles; i++)
        Update(i);
    if(Delta<Threshold)
        Terminate();
}
```

---

The method `OneIteration()` is repeatedly executed until the  $\bar{\delta} < 1/100R$ . The packing used for the simulations in this chapter were made using the parameters  $\alpha = 0.085$  and  $\beta = 0.14$ .

## 4.2.2 Computation of transport properties

Lattice Boltzmann schemes were used to calculate the permeability and diffusivity of the resultant particle packings. The spherocylinder radius was discretised as  $20 \delta x$ , where  $\delta x$  denotes a lattice unit. From the centre of each particle packing, a block measuring  $300^3 \delta x^3$  was cut. The walls  $x$ - and  $y$ -direction of the packings were sealed with solid walls, and a pressure/concentration gradient was applied in the  $z$ -direction. The permeability and diffusivity schemes described in Chapter 3 were used to calculate the transport properties of the packing.

The computed diffusivities are intrinsically non-dimensional and represent a scale-invariant property of the particle packings. The permeabilities were non-dimensionalised by the equivalent radii  $r_e$  of the particles, which are defined as

$$r_e = \left(1 + \frac{3}{2}w\right)^{1/3} R, \quad (4.20)$$

where  $R$  denotes the radius of the spherocylinders, and  $w = \frac{L}{2R}$  is the particles aspect ratio. The equivalent radius of a particle is the radius of a sphere with the same volume. The permeabilities were then computed by assuming that the equivalent radius of the particles is  $r_e = 2.5 \text{ nm}$ , as suggested by various particle packing models [2–4].

## 4.2.3 Scattering curve prediction

The scattering curves were computed using the Schmidt-Rohr method [97], which is also described in Chapter 3. The same lattice representations of packings were used as were used to characterise the transport properties.

# 4.3 Results

## 4.3.1 Spherocylinder Packings

Particle packings were generated with aspect ratios  $w$  ranging from 0 to 7.5. The resulting maximum solid volume fraction  $\phi$  varied strongly as a function of the aspect ratio, as shown in Figure 4.2. The maximum packing fraction can be obtained for slight perturbations from

the sphere, from aspect ratios of approximately 0.5 to 1.5. For the case of spheres ( $w = 0$ ) the solid fraction is approximately 62%, close to the random packing limit. For higher values of  $w$ , the maximum solid volume fraction decreases with increasing aspect ratio.

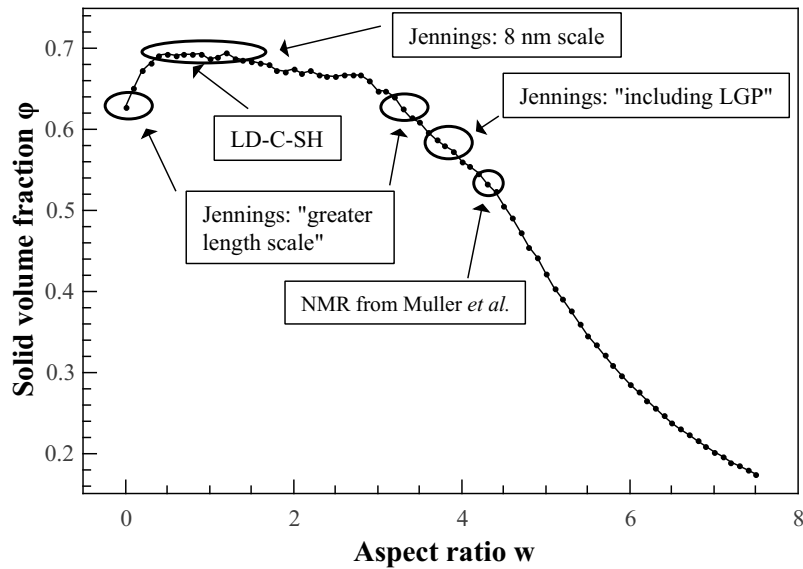


Fig. 4.2 Solid volume fractions of spherocylinders at different aspect ratios obtained with the packing algorithm. The weighting parameters were  $\alpha = 0.085$  and  $\beta = 0.14$ .

The curve agrees qualitatively with various literature reports [152, 153, 155, 156]. The detailed shape of the curve is, however, different. Literature data exhibits a relatively sharp peak with a packing fraction of about 0.72 around an aspect ratio of 0.5. This is followed by a much more uniform decrease of the packing density. The author of this thesis did not conduct detailed investigations into the origin of this discrepancy, since the details of the particle packing did not appear relevant. One may speculate that the chosen weighting parameters for the two relaxation mechanisms favour particle alignment, since  $\beta > \alpha$ . Relaxation by rotation of particles favours alignment, since it reduces the overlap.

Figure 4.2 also shows markers indicating the solid volume fractions proposed for different C–S–H particle models (see Table 4.3). These particle packings were chosen as model structures for C–S–H, to investigate the transport properties.

### 4.3.2 Scattering pattern of spherocylinder packings

The small-angle scattering curves were calculated for those spherocylinder packings matching the solid volume fractions proposed for different C–S–H densities. The results are shown

in Figure 4.3. Literature small-angle scattering data for C–S–H is shown in Figure 2.8 in Chapter 2.

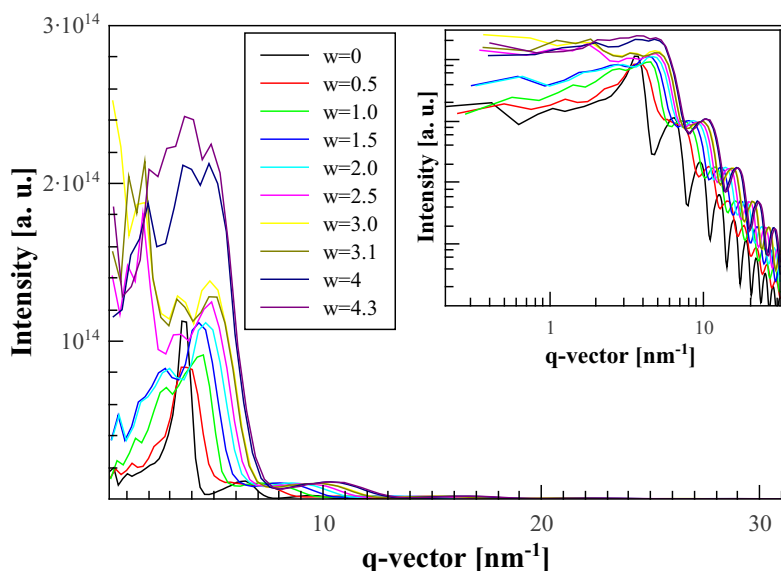


Fig. 4.3 Linear-Linear plot of spherocylinders scattering pattern; the inset shows a double-logarithmic plot. The lin-lin scale was chosen to visualise the dominating spatial frequencies and the log-log plot to emphasis the Form factor and the flattening out of the curve beyond the peak.

For large  $q$ , the curves exhibit a Porod regime with the fringes typical of the form factor of spherical particles [94]. The position of the fringes in the Porod regime is different for the curves for particle packings with different aspect ratios. The curves exhibit peaks in the low- $q$  region at about  $1.5 \text{ nm}^{-1}$ . For  $w < 2.5$ , these are relatively sharp. As the aspect ratio increases, the  $q$ -vector associated with the peak decreases. For aspect ratios of 3 and larger, the peak becomes broader and its centre moves towards smaller values of  $q$  again. Beyond this peak, all curves shown become flat.

The initial peak is due to the correlation between particle positions (and orientations) and their next-neighbours. It is typical for the scattering curve of mono-disperse particle packings [95]. As the aspect ratio increases, the peak shifts towards smaller  $q$ -vectors. This is because the particle radii were all scaled by the corresponding equivalent radii. Thus, as the aspect ratio of the particle increases, the radius of the spherocylinders decreases, as does the centre-to-centre distance between next-neighbouring particles. The broadening of the peak is probably due to geometrical frustration occurring in packings of large spherocylinders, preventing them from taking defined next-neighbouring positions.

Compared against the literature scattering curves of C–S–H, shown in Figure 2.8, the

curves are very different. Literature data does not exhibit a correlation peak. Furthermore, it exhibits two  $q^x$  regimes in the low- $q$  range [30]. The scattering curve obtained by a mono-disperse particle packing cannot explain the scattering curve measured on cement paste.

### 4.3.3 Permeability of spherocylinder packings

The permeability of the spherocylinder model was calculated for various aspect ratios using the lattice Boltzmann scheme. The results are plotted against the solid volume fraction (as mapped on the lattice) in Figure 4.4.

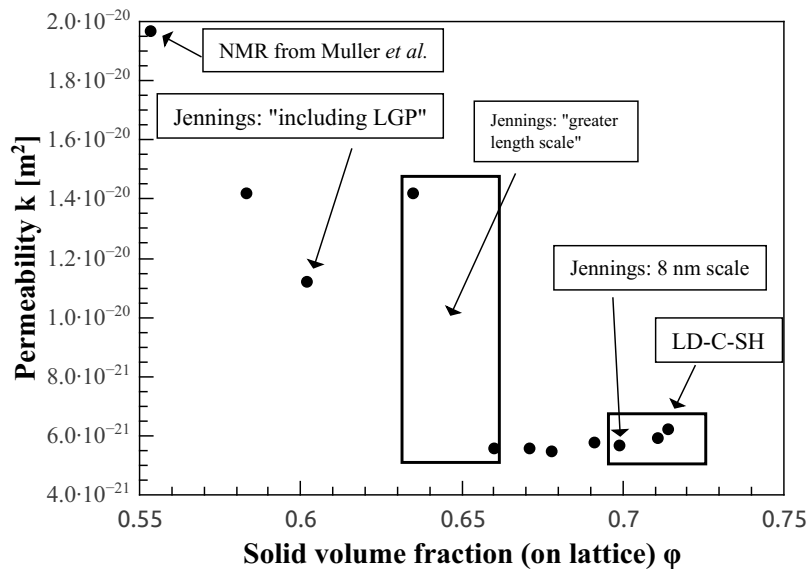


Fig. 4.4 Permeabilities calculated for selected generated particle packings, assuming an effective particle radius of 5 nm. Particle packings with the same density as particle models proposed in literature are labelled. See also Table 4.3.

The permeabilities of the packings, assuming a 2.5 nm equivalent radius, vary between  $2 \times 10^{-20}$  and  $5 \times 10^{-21}$   $\text{m}^2$ . They are plotted against the effective solid fraction in Figure 4.4. The permeability of the packings depends strongly on the solid volume fraction between 0.55 and 0.65, where it changes almost over one order of magnitude. For solid volume fractions greater than 0.65, the permeability remains approximately constant at  $6 \times 10^{-21}$   $\text{m}^2$ . This is likely to be an effect of the rescaling of the particle diameters.

The permeabilities for those particle packings with the same solid volume fractions as the particle models from the literature are marked. The permeabilities associated with these models span over half an order of magnitude. Nevertheless, all permeabilities obtained are at least two orders of magnitude larger than the lowest permeabilities measured on cement



ity: simple particle packing models cannot account for the transport properties likely to be attributed to C–S–H in cement paste.

## 4.4 Discussion

In this chapter, a simple particle model for the meso-structure of C–S–H was constructed, using spherocylinders with an equivalent radius of 2.5 nm. For different packing densities, proposed by different literature sources, the transport properties and scattering curves of the packings were calculated and compared to literature data. Despite the large spread within the transport data for mature cement paste, poor agreement was found. Most notably, both the water self-diffusion coefficient and the permeability are higher than "reasonable literature values" by at least two orders of magnitude.

A detailed examination of the modern particle models, as reviewed in Chapter 2, suggests a simple explanation for these discrepancies - the proposed model is an oversimplification of Jennings' model. Jennings' particle model proposes a hierarchical packing of particles, which is more likely to have a scattering curve with the power-laws in the low- $q$  region. Including hierarchical levels in a packing decreases the solid volume fraction and increases the pore size. If all pores, which are in C–S–H according to Jennings' model are included, the solid volume fraction is at the lower end of the packings investigated here. This means a more realistic model would be at the lower end of the solid fractions investigated here, and, therefore, be characterised by higher permeabilities and diffusivities. The current model also ignores the contribution of any interlayer pore space - effectively transport through the particles. This would increase the transport properties relative to those computed. Thus, if one assumes bulk hydrodynamics and a bulk water diffusion coefficient in the pore space between the particles, the conclusion is that a particle model for C–S–H cannot explain the low permeabilities reported for cement paste.

What happens if bulk hydrodynamics and diffusion coefficients cannot be applied within the pores space? The pores between particles of diameter 5 nm are of the same order of magnitude, and the interlayer pore space is even smaller, about 1 nm. Thus, one can raise the question as to whether the Navier-Stokes equation for continuum mechanics with no-slip boundary conditions on solid surface is valid in the gel pores of cement, or, equally, whether water in these pores actually has the same self-diffusion coefficient as bulk water.

It is well-known that the self-similarity of fluid dynamics over different length scales breaks down under certain conditions, for example, when the mean-free path of fluid molecules becomes comparable to the length scale of the problem. This "simple rule" applies for gases. Here, water in a liquid-like state is considered.

The problem is reviewed by Karniadakis et al. [101]. Bitsanis et al. investigated flow of Lennard-Jones (LJ) fluids in small channels. They concluded that deviations from continuum behaviour remain small as long as the channel is larger than ten times the diameter of a fluid molecule. In the case of water, this is about 3 nm. However, their simulations indicated an increase of the effective viscosity by a factor of 12, if the pore diameter becomes about 3 times the fluid molecule diameter. Similar data was shown for diffusion, whereby the diffusion coefficient LJ-fluid decreased by a factor of four in the same range [157].

Rotenberg et al. [158] investigated the dynamics of aqueous solutions in clays, a system similar to cement in characteristic lengths and chemistry, using molecular dynamics. In channels with a width of merely two nanometres, they found that the diffusion coefficient parallel to the confining wall decreased relative to the bulk value by a factor of two. Botan et al. [159] investigated hydrodynamics in clay nano pores using Grand-Canonical molecular dynamics. They concluded that for pore widths larger than 3 nm, macroscopic hydrodynamics with slip boundary conditions at the wall describe the hydrodynamics reasonably well. In 4.5 nm pores, the deviation from Poiseuille flow was about 30 %.

The pores between C–S–H particles were measured by Muller et al. as 4.5 nm. They are probably slightly smaller if one assumes a dense particle packing of diameter 5 nm. Therefore, it is likely that macroscopic hydrodynamics cannot completely describe the fluid behaviour within the gel pores of C–S–H. The brief literature review above, however, also indicates that those deviations are an order of a magnitude at most, more likely half that value. Thus, these deviations cannot explain the difference between the simulated values for the particle packing and literature-found transport properties for C–S–H.

## 4.5 Conclusion

A highly simplified colloidal model was tested as a transport model for flow and diffusivity through the calcium-silicate-hydrate found in hydrated cement paste. The simple proposed model led to transport coefficients exceeding literature estimates by at least a factor of 100. Any attempt to modify the structure to be closer to Jennings' model is likely to increase the transport coefficients. The potential effects of the small pore sizes were discussed. These may or may not play a role but are not sufficient to explain the discrepancy. It is unlikely that any of these effects depresses the viscosity of the pore fluid by more than a factor of 100. It is clear that a better understanding of the structure as well as the water dynamics in C–S–H is needed. The results presented here make a strong point against the validity of a colloidal model.

# Chapter 5

## Filling of three-dimensional space by two-dimensional growing sheets

Models of three-dimensional space filling based on growth of two-dimensional sheets are proposed. Beginning from planar Eden-style growth of sheets, additional growth modes are introduced. These allow the sheets to form layered or disordered structures. These mechanisms can also be combined. A new kinetic Monte-Carlo-based computer model was developed to study the kinetics of these new models and the resultant structures. For the first time, it was possible to study space filling by two-dimensional growth in a three-dimensional domain with arbitrarily oriented sheets; the results agree with previously published models where the sheets were only able to grow in a limited set of directions. The introduction of a bifurcation mechanism gives rise to complex disordered structures that may be interesting as model structures for the meso-structure of calcium-silicate-hydrate in hardened cement paste.

### 5.1 Introduction

In this chapter, growth of two-dimensional sheets and the resultant filling of three-dimensional space is studied. The author's primary interests can be summarised into three questions:

1. How is space filled by two-dimensional growth processes?
2. How can two-dimensional growth sample three-dimensional space?
3. How can the amount of disorder be controlled in these structures?

These questions arise from the author's thoughts about the meso-structure of calcium-silicate-hydrate in cement paste, which is a material of overwhelming economic and environmental impact. Quasi-continuous sheet structures have been proposed as a model for C–S–H by different authors [5, 7, 8]. Despite the recognised importance of the meso-structure of C–S–H, quasi-continuous sheet structures have never been explored with a numerical model. The problem of space filling by sheets or other anisotropic growth processes is of wider interest, as it will be discussed below. In this chapter, the problem of space-filling by growing sheet structures is investigated on an abstract level, putting the focus on the kinetics and the structure.

In this thesis, the word *growth* is used to describe the evolution of an object from a single nucleus. The object is referred to as a cluster. The simplest growth model conceivable is an  $D$ -dimensional sphere, growing radially in time. A range of different growth models has been proposed for a variety of applications. The Eden process, forming the base of the modelling presented here, was conceived to model cell growth on a Petri dish [160]. Variants of the model have been used for the growth of tumour cells [161] and polymer crystals [23]. The Witten-Sander model (diffusion limited aggregation, DLA) and the Vold-Sutherland model (ballistic deposition) describe the aggregation of sticky particles [162, 163].

*Space filling* refers to the process of space being filled by structures *growing* from one or multiple nuclei. It can be seen as a competition between different clusters for space. The first space filling models were developed by metallurgists to understand phase transformation kinetics in metals [164, 165]. Analytical and numerical space filling models have been applied to problems in space filling, including metals [90, 166], polymers [167], and cement (on paste length scale) [46–48].

The growth of sheets is described via a two-dimensional Eden model [160]. Additional mechanisms, which occur infrequently, are introduced. These allow the sheets to sample three-dimensional space. Some of these mechanisms allow parts of the growing sheet to change its direction. The proposed extensions of the Eden model lead to at least three new growth models. The kinetic properties of these extended Eden growth models are investigated and the morphologies of the grown clusters discussed. In a second step, space-filling by clusters emerging from the growth models is studied in a continuous nucleation scenario. The evolution of the model was simulated using a new algorithm.

The remainder of this chapter is organised as follows: in Section 5.2.1, the properties of the Eden model are briefly reviewed and some of the metrics introduced to characterise the properties of the grown cluster. Subsequently in Section 5.2.2, the model of Kolmogorov, Johnson, Mehl and Avrami (KJMA) is introduced and the problem of anisotropic growth is discussed. The Avrami plot, a quantitative analysis method for kinetics of space filling, is

also introduced. The modelling presented in this work is based on a set of seven key ideas (Section 5.3.1). These can be combined to create different growth and space filling models, which are presented in Section 5.3.2. The new kinetic Monte Carlo scheme used to study the kinetics of the models is the topic of Section 5.4.1. In Section 5.5, the kinetic properties of the models are analysed and the grown structures discussed.

The ideas presented in this chapter have been used to develop a cavity filling sheet model to describe the formation of calcium-silicate-hydrate in an environment resembling a (capillary) pore in hydrating cement paste. The properties of the structure were calculated and compared against experimental results on cement paste [168]. This is discussed in Chapter 6.

## 5.2 Background

### 5.2.1 The Eden model and its properties

The most simple models of growth are simple geometric shapes whose characteristic length  $r$  (for example, the radius of a sphere) increases with time. These have been used to describe growth in space-filling models such as the Kolmogorov-Johnson-Mehl-Avrami equation (see next section). With the appearance of computers came stochastic growth models. One of the first of these growth model was the Eden model [160], which is the base for the work described here.

The structure arising from a growth model is called a cluster. The clusters grown are typically characterised by their dimensionality,  $D$ . The clusters discussed in this chapter are always discretised. Each discrete element is referred to as a site, to achieve consistency in language to the literature concerning lattice-based growth models. If the structure is compact and hole-free, the number of sites within the cluster scales as  $N \sim r^D$ , where  $r$  is a characteristic length of the structure, such as the radius of a circle. Correspondingly, the number of surface sites  $S$  scales as  $S \sim r^{D-1}$ . For open structures, the concept of the radius is replaced by the radius of gyration,  $r_g = \sqrt{\frac{1}{M} \sum_{i=0}^{M-1} (\mathbf{r}_i - \bar{\mathbf{r}})^2}$ . Using the Hausdorff-dimension,  $D_H$ , analogous to the dimensionality, the number of cluster sites scales as  $N \sim r_g^{D_H}$  [163].

The original Eden model was developed on a two-dimensional rectangular lattice [160]. However, versions on other lattices, for example, honeycomb or triangular lattices [90, 161], have been developed. Jullien and Botet identify three variants of the Eden model [169]: In the original Eden model, a random bond between an unoccupied and an occupied lattice site is chosen and the unoccupied lattice site occupied. This version is called Eden B and

is used in this work. In the Eden A model, all those sites adjacent to the surface of a lattice are picked with equal probability, which leads to a rougher cluster surface. In the Eden C model, a random occupied site at the surface is chosen. The growth site is then any of its empty neighbouring sites, chosen with equal probability. This leads to relatively smooth surfaces, due to the enhanced probability of choosing unoccupied surface sites with many occupied neighbours. Other variants of the Eden model include the introduction of a noise reduction parameter to alter the kinetic behaviour of the cluster and the cluster morphology [170]. Eden models have been also been combined with diffusion-limited-aggregation models [171].

The Eden model appeals through its simplicity. Crystal growth can be imagined as the sites in a crystal lattice being randomly occupied by material coming from solution [23], or by randomly adding an elementary cell to the crystal lattice. This is why it was chosen for this work. In fact, the author of this thesis chose the Eden model as the base for this work intuitively without even being aware it has been a widely studied process, which was only later pointed out to him.

The properties of the Eden models have received considerable attention. Numerical studies have shown that the perimeter,  $S_E$  of the Eden cluster scales as  $S_E \sim N_E^{(1-1/D)}$  for large clusters in two and three dimensions, where the dimensionality is denoted as  $D$  and  $N_E$  is the number of growth sites in an Eden cluster [163]. However, for small clusters deviations were reported [172]. Leyvraz showed that the surface of the cluster scales as  $S_E \sim N_E^{(1-1/D)}$  for this class of models [173]. A time scale can be introduced to the Eden model by defining growth probabilities on surface sites per unit time [23, 90].

In this work, the Eden model is extended to grow lattice-free into space by placing regular triangles into the space and randomly adding material to the perimeter. This idea is, to the best of the authors knowledge, novel.

## 5.2.2 Models of space filling and anisotropic growth

Models of space filling describe how space is filled by clusters. In principle, each space filling model may be split into four components:

1. The space in which growth can occur may be finite of a given shape, or infinite space may be considered<sup>1</sup>.
2. A model for nucleation is needed, which controls the nucleation rate  $k_N$ . In this work, a constant nucleation rate is referred to as continuous nucleation. If a number of nuclei is initially present, it is called the site saturation case,  $k_N = \delta(t)\rho_N$ , with  $\delta(t)$

---

<sup>1</sup>Space filling of an infinite domain can only work if a density of nuclei is defined.

being the Dirac symbol,  $t$  denoting time, and  $\rho_N$  the number density per unit volume of nuclei.

3. A model describing the evolution of a nucleus deposited at time  $t'$ . The cluster's volume is denoted as  $V(t, t')$ .
4. A model for the interaction between different clusters. In this work, it is taken to be hard exclusion between solids. The process of further growth being hindered by previously grown solids is called impingement.

Probably the first, and almost certainly most popular, model of space filling is the analytic model due to (in order) Kolmogorov, Johnson and Mehl, and Avrami (KJMA)[165, 174, 175]<sup>2</sup>. The motivation of these authors was to understand the observed phase transition kinetics of metals. Growth is described in infinite domains for homogeneously distributed nuclei, either in the site saturation or continuous nucleation cases. The growth model in the KJMA model is a sphere of the same dimension as space. The final result for the solid fraction of space  $\varphi(t)$  reads

$$\varphi(t) = 1 - \exp(-kt^n). \quad (5.1)$$

The constant  $k$  is a collection of different constants invoked in the derivation, among others the radial growth rate of the sphere and the nucleation rate or number of initial nuclei. In this work,  $n$  is referred to as the growth exponent. It is determined by the growth mechanism and the nucleation model. In the site saturation case, the growth exponent is equal to the dimension of growth. For a constant nucleation rate the growth exponent is equal to the dimension of growth plus 1. Variations of the model have been developed to account for variable growth and nucleation rates in time [166]. Improvements have been made, most notably by Cahn, who introduced the time cone formalism to derive expressions for  $\varphi(t)$  in confined spaces and at the presence of grain boundaries [176]. This formalism has been used by Villa and Rios to develop analytic expressions for the filling of confined spaces with different shapes [177]. Model extensions have also been proposed to predict the cluster size distribution [178, 179].

The KJMA analysis gives rise to the classical analysis for space filling processes. Equation 5.1 is linearised as  $\ln(\ln(1/(1 - \varphi(t)))) = n \ln(t) + \ln(k)$ . The corresponding plot of  $\ln(\ln(1/(1 - \varphi(t))))$  versus  $\ln(t)$  is referred to as the Avrami plot; the slope of the curve gives the growth exponent. For processes following the KJMA theory, the Avrami plot yields a straight line. This means that the growth exponent is constant. If the growth mechanism changes in the process, the exponent changes as well.

Shepilov and Baik note that the treatment of the exclusion between different clusters in the KJMA model imposes a set of conditions on the validity of Equation 5.1 [180]. One of

<sup>2</sup>Kolmogorov published first and in Russian.

these conditions is that the "growth rate in a fixed direction is the same for all (...) [clusters]", as long as growth is not blocked by other clusters. In other words, anisotropic growth cannot be treated by Equation 5.1. Anisotropic growth leads to mutual blocking of clusters, as seen in Figure 5.1. Blocking describes the process when a cluster is denied a point in space by a second cluster, without that point in space being included in the second cluster at that time.

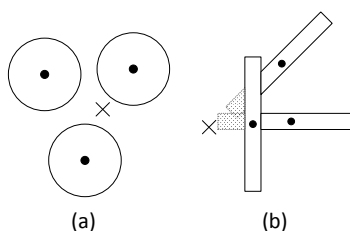


Fig. 5.1 The derivation of the KJMA equation requires that a nucleation event at a point guarantees the extent of the grown structure to a certain point ( $\times$  in the figure). This is the case for growing spheres, here illustrated in two dimensions (b) Growing one dimensional structures in two dimensions can block each other, the vertical rod prevents the angled rods from reaching  $\times$  in (b). Drawn similar to [180].

Computer models have been used to study anisotropic growth. Shepilov and Baik used ellipsoids in three dimensions and treated the blocking explicitly up to limited order [180]. Puzstai and Gránásy considered growing ellipses in two-dimensional space; interaction between the ellipses was treated by mapping the ellipses onto a lattice. Blocking was treated by only allowing growth of pixels that are intersected by the ellipsoid and have a neighbouring lattice site belonging to the same shape [181]. Godiksen et al. did the same with ellipsoids in three-dimensional space [182]. These authors observed that for mild-anisotropy of the growing shapes, the deviations from KJMA kinetics are small. If the anisotropy becomes large, they observed that early in the process, before the clusters impinge, the KJMA equation holds.

The extreme case of anisotropic growth is when the dimensionality of growth is lower than the dimension of filled space. Kooi used a lattice-based discrete time step Monte Carlo algorithm to study such situations for one-dimensional growth in two dimensions and two-dimensional growth in three dimensions. The growing needles and sheets were constrained by the lattice to a limited number of orientations. Interestingly, as a two-dimensional growth model, an over-damped Eden model was used [183]. For the site saturation case, growth ends when the sheets impinge on each other. If the nucleation rate is constant, a second growth regime with a low growth exponent is observed at long times after the impingement. In this regime, the voids between the first sheets are filled by shorter sheets, leading to a behaviour comparable to the packing-limited growth model for spheres [62].

## 5.3 The sheet growth model

### 5.3.1 Model elements

The motivation of this chapter is to investigate how sheets grow in space, and how disorder can be introduced in these models. Based on an Eden model for the two-dimensional "pure" sheet growth, a set of further growth mechanisms was identified. These are shown in Figure 5.2. In order to grow the sheets, they are discretised as triangular prisms with side-length  $L$  and height  $h$ . The whole model can be summarised as:

1. Each sheet has a thickness  $h$ .
2. Sheets exclude each other; any point in space can only belong to a single segment.
3. Nucleation is modelled by randomly placing a triangle in the domain. Thus, nuclei have finite size and an orientation.
4. *Sheet growth* is modelled by coupling a two-dimensional Eden model [160] with a kinetic Monte Carlo scheme (KMC). New triangles are added with a rate  $k_S$  to edges of previously deposited triangles, which are referred to as growth sites. This approach allows complex geometrical situations such as growth around other sheets to be resolved.

This approach allows modelling of planar growth and space filling by planar sheet growth. The subsequent model elements were conceived when considering how a two-dimensional growth model could sample three-dimensional space:

5. At each site available for planar growth, a second process can occur where newly grown segments are tilted by an angle  $\gamma_B$  around the perimeter from which it has grown. This occurs with a rate  $k_B$  and is referred to as *bifurcation*.
6. New sheets may form layers on previously deposited sheets, with a rate  $k_L$ , at a distance  $d$  from the previous sheet. This is termed *layering* and occurs from locations called layering sites.
7. Alternatively to forming aligned sheets, the newly nucleated sheets may tilt out of the plane of alignment by an angle  $\gamma_T$ . This process has a rate  $k_T$  and is labelled *tilted layering*.

These elements can be combined into a range of different growth models, which are outlined in Section 5.3.2.

### 5.3.2 Combinations of model elements

The model elements 5-7, introduced in Section 5.3.1, can be combined with simple sheet growth to a variety of models for growth and space-filling.

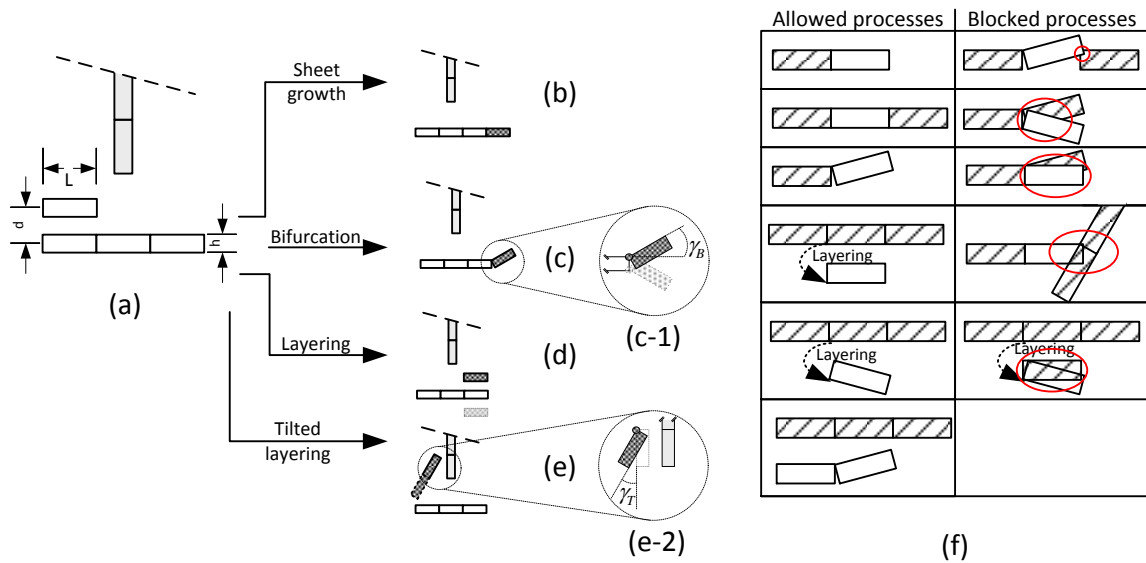


Fig. 5.2 Two-dimensional illustration of the key elements and the growth steps. The new triangle is always filled. (a) shows an example with two sheets about to impinge with perpendicular angle and the definition of sheet thickness  $h$ , interlayer space  $d$  and triangle side length. (b) shows a planar growth step extending the horizontal sheet, (c) a bifurcation step. The enlargement (c-1) defines the bifurcation angle  $\gamma_B$  and shows the alternative bifurcation process as dotted lines. Note the dot marking the rotation axis. (d) shows a layering step and (e) a tilted layering step. The enlargement (e-2) defines the tilt angle  $\gamma_T$  and the rotation axis relative to a layering step occurring at the same position (grey). (f) table of allowed and blocked configurations in a two-dimensional illustration.

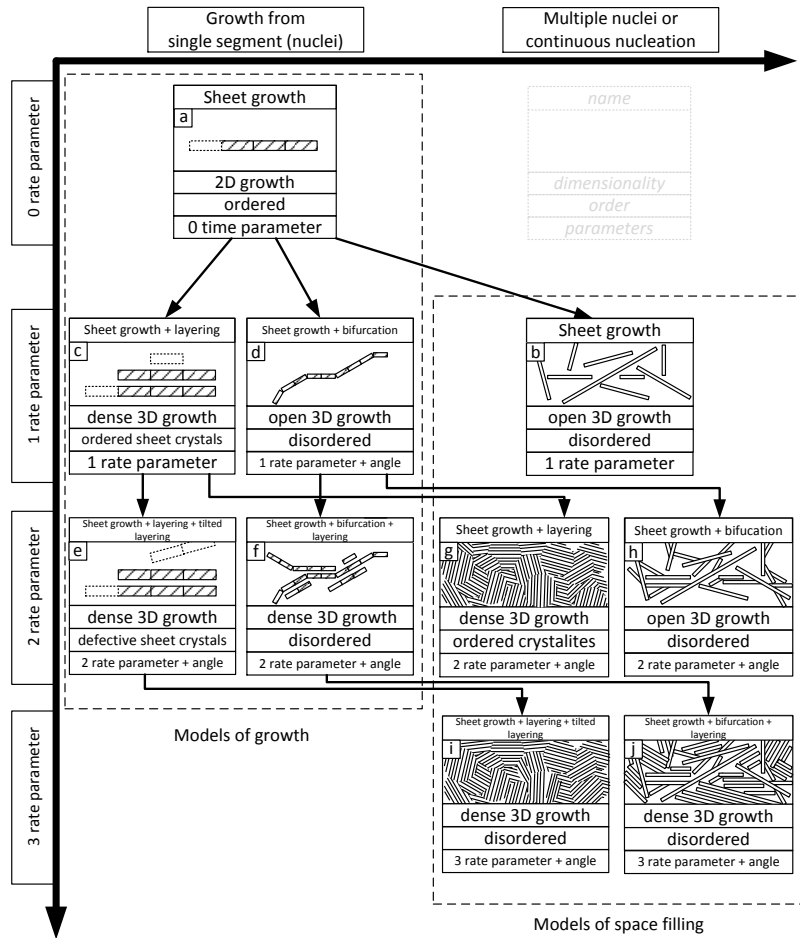


Fig. 5.3 Overview of the sheet growth models. Starting from the Eden model (sheet growth), gradual addition of complexity leads to models forming complex clusters. Introducing a nucleation model or a finite domain turns the growth models into models of space filling.

Figure 5.3 classifies the models according to the number of rate parameters and the nucleation mode. Alternatively, the models are classified as models of growth or space filling (left and right column). Time is always made dimensionless by the sheet growth rate, thus, it is not a free parameter. The ability to sample space is characterised. Growth is classified as dense if no significant holes allowing further growth processes remain within the evolved structure. The order within the structure is also qualitatively characterised.

The simplest conceivable model is sheet growth from a single segment, shown in Figure 5.3a. This model is an Eden model [160] on a two-dimensional lattice with arbitrary orientation in three-dimensional space. The resultant structure is an almost circular disc with a rough surface, see Section 5.2.1. Two mechanisms are proposed to allow two-dimensional growth to form three-dimensional structures. In the simplest step, new segments can nucleate aligned with an existing sheet a certain distance  $d$  away, which is called layering. This is shown in 5.3c. The resultant structure grows in three dimensions and produces a highly ordered sheet crystal, prohibiting any further growth within its boundaries<sup>3</sup>. Alternatively, defects can be introduced as individual sheets grow, as shown in Figure 5.3d. Occasionally, segments are allowed to tilt out of the plane of growth, leading the sheet to bifurcate. One expects disordered three-dimensional structures from such a process.

The order in the crystalline structure grown with the growth and layering model (Fig. 5.3c) can be broken up by tilting the new segments during the layering step, introducing defects and new orientations of growth. Now, disordered polycrystalline structures emerge from a single nucleus. This is the model in Figure 5.3e. Layering can also be introduced in the bifurcation model, as shown in Figure 5.3f. The nature of growth will depend on the relative importance of the layering step towards the growth rate.

Space filling of a domain by sheet growth in a space filling scenario leads to disordered open structures, Fig. 5.3b. It is important to note that the structures densify further and are expected to eventually fill space, if nuclei are of infinitesimal size. The relative orientations of impinging sheets are uncorrelated. The growth models of Figure 5.3c and 5.3d can be introduced in multiple-nuclei scenarios as sketched in Figures 5.3g and h. Sheet growth and layering lead to structures which can be described as polycrystalline sheet structures, see Figure 5.3g. They exhibit a high degree of order within each crystallite originating from a single nucleus, whilst the orientation of different crystallites is uncorrelated. This scenario is expected to follow standard KJMA kinetics. Growth with bifurcation in a multiple nucleation scenario, as shown in Figure 5.3h, leads to disordered, porous structures. The structures originating from single nuclei are porous by themselves, and the kinetics of the space filling will be dominated first by growth of the disordered cluster from the individual

---

<sup>3</sup>This assumes that no growth is possible between sheets.

nuclei, and later by the impingement between these clusters.

A space filling version of the model illustrated in Figure 5.3i, was used by this author to model the development of the nano-structure of cement [168], which is discussed in Chapter 6. Therefore, it will be omitted from the discussion here. The study of the model of Figure 5.3f and the corresponding space filling model, Figure 5.3j, was not included in the thesis due to the excessive memory requirements.

This work concentrates on introducing disorder into sheet-like structures; the properties of the three growth models 5.3a, c and d will be studied. The focus will be on the kinetic properties.

### 5.3.3 Theory of sheet growth

In this section, the expected kinetic behaviour of the growth and space filling models is developed from theoretical considerations. For most models of growth, it is attempted to find expressions for the number of triangles (sites) in a cluster as a function of time, or at least to evaluate the expected growth exponent.

#### Two-dimensional growth

Pure two-dimensional growth of a single sheet leads to a two-dimensional object. It has a characteristic measure  $r$ , which would be the radius of a circle or the side length of a square. The surface area of the object is denoted  $A$ . Consider an infinitesimal expansion of the shape,  $dr$ . If the shape is sufficiently large,  $dr$  can be approximately the height of a triangle. This is sketched in Figure 5.4.

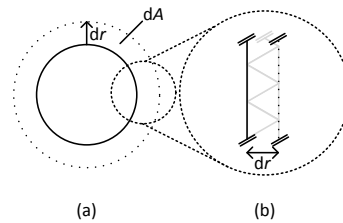


Fig. 5.4 Idea behind deriving  $N(t)$  for sheet growth.

The number of equilateral triangular segments with side length,  $L$ , in such a shape changes per time step such that:

$$\frac{\partial N}{\partial t} \approx \frac{1}{A_{\Delta}} \frac{\partial A}{\partial t} = \frac{C}{A_{\Delta}} r \frac{\partial r}{\partial t}. \quad (5.2)$$

The constant,  $C$ , relates the length of the perimeter,  $L_P$ , of the shape to the characteristic size, such that  $L_P = Cr$ .  $A_\Delta = \frac{\sqrt{3}}{4}L^2$  is the surface area of an equilateral triangle with side length  $L$ . If one assumes that the radial growth rate<sup>4</sup> is  $\partial r/\partial t = \frac{\sqrt{3}}{2}k_S L$ , one obtains:

$$\frac{\partial N}{\partial t} \approx \sqrt{3}Ck_S^2 t. \quad (5.3)$$

Setting  $C = 2\pi$ , as in a circle, leads to

$$\frac{\partial N}{\partial t} \approx 2\pi\sqrt{3}k_S^2 t. \quad (5.4)$$

Integration of this equation leads to the scaling law for the number of triangles in large clusters

$$N = \sqrt{3}\pi k_S^2 t^2. \quad (5.5)$$

The result for the growth rate versus number of inserted segments is also given:

$$\frac{\partial N}{\partial t} = 2\sqrt[4]{3\pi^2}k_S\sqrt{N}. \quad (5.6)$$

These equations are only expected to hold for the limit of very large structures. They are, as it will be seen in the next section, useful approximations to understand how fast the individual sheets grow.

### Sheet crystals: clusters grown by sheet growth and layering

If sheet growth and layering occur together, the triangular segments within the resultant sheet crystal are arranged on a triangular-prismatic lattice. The resultant three-dimensional growth is expected to behave like an Eden model in three dimensions. Therefore, a growth exponent of 3 is expected for sufficiently large structures [173]. The aspect ratio of these structures is related in a non-trivial way to the ratio between the sheet growth and the layering rate,  $k_S/k_L$ . This was already observed by Eden in two dimensions when he first published the model [160].

### Growth with bifurcation

In Figure 5.5a, a few bifurcation events are sketched on a growing sheet; when a bifurcation event occurs, a half-circularly shaped sheet grows into space, as outlined in Figure 5.5a. Thus, each bifurcation event effectively creates a nucleation site for a new sheet. Figure

---

<sup>4</sup>  $\frac{\sqrt{3}}{2}L$  is the height of an equilateral triangle with side length  $L$ .

5.5b (marked spots) and c show how sheets of the same cluster can impinge on each other internally. This is expected to occur via two mechanisms: Figure 5.5b shows in cross section how sheets of the 1st generation are not able to impinge in cross section. Only those of the 2nd and higher generation are able to impinge on sheets of any other generation. If this mechanism for internal impingement dominates, the characteristic time until the first impingement is expected to depend on the bifurcation angle  $\gamma_B$ . Alternatively, as shown in Figure 5.5c, 1st generation sheets can intersect in the plane of their parent sheet. In this case, the bifurcation angle should not play a role. It is possible that both impingement regimes occur, and it is reasonable to assume that they are controlled by the relative likelihood of bifurcation events,  $\frac{2k_B}{2k_B+k_S}$ .

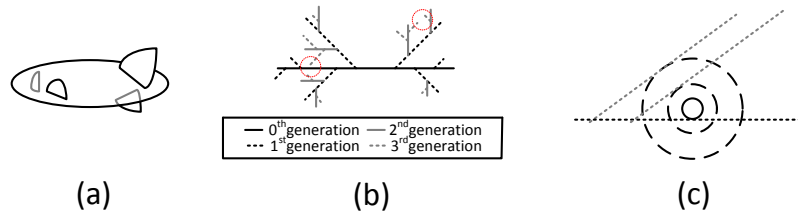


Fig. 5.5 (a) 3D illustration of an early structure generated by sheet growth and bifurcation. (b) 2D illustration of the tree-like structure generated by sheet growth with bifurcation. Red-dotted circles denote sites where internal impingement is imminent. (c) Growing sheet shown in the plane of the page (circles). The dotted lines are sheets growing out of the plane due to bifurcation at different times (for example towards the observer). Internal impingement can occur if the sheets intersect on the plane of the parent sheet.

As Figure 5.5a indicates, each bifurcation site effectively serves as the origin for an approximately half-circular sheet. For each of the new sheets, Equation 5.5 should hold. Let us consider a growing sheet in space; bifurcation events are possible at the perimeter of the sheet, effectively leading to new sheets, similar to a nucleation event. For the moment, it is assumed that at the new sheets, no further bifurcation events are possible. The number of triangles in a sheet nucleated at  $t'$  is denoted as  $N(t, t')$ . The length of the perimeter of the primary sheet is proportional to its radius, so one has  $L_P \sim (t - t')$ . Since bifurcation can occur at each perimeter segment, the number of bifurcation events is  $\beta(t - t')$ . The constant  $\beta$  contains the necessary proportionality factors and the bifurcation rate. Combining this with  $N(t, t')$  leads to the number of segments in a first-generation-only bifurcation cluster:

$$N(t, t') + \int_{t'}^t \beta(t'' - t') N(t, t'') dt'' \quad (5.7)$$

(This is actually also an interesting case to investigate. The author of this thesis regrets that he had this idea only during an attempt to clarify this section a few days before submission).

If bifurcation is also possible on those sheets which were formed by bifurcation themselves, a recursive expression can be obtained if internal intersection between the sheets grown from the same cluster is ignored. The sheets of generation  $i$  are denoted by a superscript  $(i)$ ; the sheet growing from the first nucleus has the superscript  $(0)$ . The segments of all sheets of higher generations bifurcating from it are included into its number of segments  $N^{(i)}(t, t')$ .  $t'$  denotes the time of nucleation/bifurcation of the sheet. The number of segments in such a sheet is the sum of a  $t^2$  term for the growth of the main sheet plus those in the sheets formed by bifurcation. These can be found by integrating in time over the product of the probability to nucleate a sheet per unit time and the expression for the segments contained in a segment,  $N^{(i)}(t, t')$ . Thus, if created at  $t^{(i)}$ , the number of segments of sheet of generation  $(i)$  and higher is given by the recursive equation:

$$N^{(i)}(t, t^{(i)}) = \alpha^{(i)}(t - t^{(i)})^2 + \int_{t^{(i)}}^t N^{(i+1)}(t, t^{(i+1)}) \beta(t^{(i+1)} - t^{(i)}) dt^{(i+1)}. \quad (5.8)$$

The constant  $\alpha^{(i)}$  is the prefactor from Equation 5.5.

As already indicated, internal impingement is inevitable and occurs at some point. This leads to a decrease of the growth exponent. Equation 5.8 can be evaluated, if one assumes that only  $J$  generations of bifurcation events occur. This leads to

$$N^{(0)}(t, t^{(0)}) \sim t^{2+2J}, \quad (5.9)$$

still assuming that the sheets formed by bifurcation do not impinge on each other internally.

As soon as internal impingement occurs, one expects the growth exponent to decrease. Since at least 1 generation of sheets needs to be formed by bifurcation,  $\text{Min}(J) = 1$ . Thus, the lower bound for the growth exponent for sheet growth and bifurcation is 4. Impingement can either occur in the plane of the 0th generation (see Figure 5.5c) or, as shown in Figure 5.5b, between sheets of the 2nd generation. Therefore, it is unlikely that more than two generations of sheets form by bifurcation at any time, thus,  $\text{Max}(J) = 2$ . This leads to the upper bound for the growth exponent for sheet growth and bifurcation, which is 6.

For long times beyond first internal impingement, only those sheets whose growth sites lie on the surface of the convex hull of the cluster can continue growing. Thus, the growth exponent is expected to approach a three-dimensional growth law,  $N \sim t^3$  for large  $N$ . This is effectively the Leyvraz approach [173].

### Space filling by two-dimensional growth

Consider an infinite domain with a nuclei density of  $\rho_N$ . Each nucleus is placed at a randomly chosen position. The average distance between the nuclei is then  $D_N = \rho_N^{-1/3}$ . Deviations from unhindered growth are expected when the size of the growing objects becomes equal to some critical size,  $D_c \approx C_2 D_N = C_2 \rho_N^{-1/3}$ . The constant  $C_2$  is expected to be 1 for spherical growth and in the order of 1 for anisotropic growth. The sheets are assumed to grow with constant radial growth rate  $\dot{r}$  ( $= \frac{\sqrt{3}}{2} L k_S$ ). The first impingement between sheets should then occur then at a critical time,  $t^*$  [183]:

$$t^* = \frac{C_2^{3/4}}{k_N^{1/4} \dot{r}^{3/4}} \quad (5.10)$$

Well beyond the first impingement, any non-dense growth leads to a regime in which the growth from the last-inserted nucleus comes to a halt before the next nucleus is inserted, as has been shown by Dodds and Weitz for packing limited growth of spheres [184]. Kooi points out that in this regime, the inserted volume is expected to depend only on the average size of the void,  $D_v$ , in the structure in which the sheet is inserted. He proposes  $D_v \propto \rho_N^{-1/3}$  and the inserted volume being  $V \propto h D_v^2$ , with  $h$  being the sheet height. In a continuous nucleation regime, one obtains

$$V(t > t^*) = V(t^*) + \int_{t^*}^t k_N V(t, t') dt' = V(t^*) + \int_{t^*}^t k_N \frac{Z}{(t k_N)^{2/3}} dt' = V(t^*) + Zh(k_N(t - t^*))^{1/3}. \quad (5.11)$$

$Z$  is the collection of all the proportionality constants involved in the derivation of Equation 5.11. It shows that in a scenario of two-dimensional sheet growth in three-dimensional space one expects the growth exponent to fall to  $\frac{1}{3}$  past the initial blocking.

#### 5.3.4 How the models are studied

The primary aim of this study is to examine the dynamic properties of the different growth models and corresponding models of space filling. The growth exponents as a function of time are obtained from a classic Avrami plot for the space filling models.

For the growth models, it is assumed that they grow in an infinite domain. Numerically, this is realised by terminating the simulation as soon as the structure touches the domain boundary. These models are studied by investigating the number of segments as a function of time,  $N(t)$ . This is equivalent to studying the volume of grown solid or surface area with time, but as a dimensionless, and therefore more general, case. Since the volume

is infinite, the fraction of space filling becomes infinitesimal. Via a series expansion of the inner logarithm of the Avrami linearisation, it can be shown that it then becomes:  $\ln(N(t)) = n \ln(t) + \ln(A_N)$ . The element prefactor  $A_N$  is also evaluated for the growth models to be able to give an approximate expression for the number of segments in the cluster after a certain time.

For the clusters evolving via different growth models, the power law for  $r_g(t) = A_r t^{n_r}$  is evaluated. The radius of gyration,  $r_g$ , indicates the approximate size of the resulting structure, and  $A_r$  is called the radial prefactor, and  $n_r$  the radial growth exponent. For the growth of a two-dimensional sheet, the assumption of circular growth leads to the approximate radius. The corresponding growth laws are important measures if analytical models of space filling of the more complex models are discussed.

All time scales and rate constants are normalised by the sheet growth rate. All length scales are given relative to the side length of a triangle, and time is always rescaled relative to the sheet growth rate  $k_S$ .

## 5.4 Numerics

In order to simulate the evolution of the model proposed in the previous section, a computer algorithm must be able to describe the positions of the sheets in space and to simulate the growth as a function of time. Kinetic Monte Carlo (KMC) schemes have been used for the latter purpose. Previous numerical growth models usually relied either on lattices to keep track of the spatial arrangement of the solids, or were only able to handle simple growing shapes.

In order to describe the position of the sheets in space, they were discretised as triangles whose vertices can take arbitrary positions in three-dimensional space. In this section, the KMC scheme is introduced and the algorithm discussed.

### 5.4.1 Kinetic Monte Carlo scheme

Kinetic Monte Carlo (KMC) is introduced in Chapter 3, where a generalised derivation of Gillespie's algorithm is given [91].

The model elements require up to five different discrete processes to occur at two different types of growth sites: planar growth and bifurcation can occur at the active perimeter sites of an existing sheet. Layering and tilted layering can occur over the active triangular facets of segments.

The index  $x$  is used to denote the type of a growth event, which is 0 for sheet growth, 1

for bifurcation, 2 for layering, 3 for tilted layering and 4 for bulk nucleation. At any given time,  $l_x$  denotes the number of possible events of type  $x$ . Each event is denoted by the letter  $G_i^x$ , where  $i$  denotes the  $i$ th event of that type. The events are associated with sets, which are denoted  $L_x$  and have  $l_x$  elements each<sup>5</sup>. With each type of growth events, a growth rate is associated<sup>6</sup>, which are  $k_0 = k_S$ ,  $k_1 = k_B$ ,  $k_2 = k_L$ , and  $k_3 = k_T$ . For example, there are  $l_0$  possible sheet growth events in the set  $L_0 = \{G_0^0, G_1^0, G_2^0, \dots, G_{l_0-1}^0\}$ . The growth events  $G_i^x$  are to be understood as attempted growth events, and the rates are to be interpreted as the *probability for an event to be attempted per unit time per site*. Continuous nucleation in the volume requires the definition of the nucleation rate,  $k_4 = k_N$ , which is interpreted as the probability for a nucleation attempt per unit volume per unit time.

The algorithm proposed here does not "know" whether an event at site  $G_i^x$  is successful, which means it will grow a new triangle, or whether the new triangle will intersect with another sheet and, therefore, be rejected, which means the event fails. Failed events are treated as successful ones. The implications of this are discussed at the end of this chapter section.

Subsequently, the generalised algorithm, introduced in Chapter 3, is applied to the sheet growth model. The number-weighted probability for an event to be attempted per unit time step is  $K_i = l_i k_i$  for  $i = 1, 2, 3$  and  $K_i = V k_N$  for  $i = 4$ , the continuous nucleation process.

The probability that an arbitrary event will occur in the interval  $(t + \tau, t + \tau + d\tau)$  is the sum of all number-weighted probabilities:

$$P_1(\tau) = \sum_{j=0}^4 K_j \cdot \exp\left(-\sum_{i=0}^4 K_i \tau\right). \quad (5.12)$$

This probability can be sampled by drawing the time interval such as

$$\tau = \frac{1}{K} \ln(1/X_2), \quad (5.13)$$

where  $X_2$  is a uniformly drawn random number between zero and one.  $K$  denotes the sum over all  $K_i$  and is sometimes referred to as the rate line. Since  $\langle \ln(1/X_2) \rangle = 1$ , the time interval  $\tau$  has also been sampled [86] as

$$\tau' = \frac{1}{K}, \quad (5.14)$$

<sup>5</sup>The numerical index  $i$  is used to denote the different events. This does not imply any order of the events within the set.

<sup>6</sup>The formulation of the scheme becomes considerably easier if an ordered index is used, for example, numbers instead of letters.

which is the expression used in this work. The joint probability that if a process is attempted in the time interval  $(t + \tau, t + \tau + d\tau)$ , it is of type  $x$ , is

$$P_2(x|\tau) = \frac{K_x}{\sum_{y=0}^4 K_y}, \quad (5.15)$$

where  $x$  can take the values 1, 2, 3, 4. The joint probability  $P_2$  is sampled by drawing a uniformly distributed number  $X_1$  between zero and one and taking the process  $x$  fulfilling

$$\sum_{i=0}^{x-1} K_i < X_1 K \leq \sum_{j=0}^x K_j, \quad (5.16)$$

where  $K$  denotes the sum of all number weighed probabilities.

This leads to the program flow diagram summarised in Figure 5.6. After initialisation, the class of the process to be attempted is determined using Equation 5.16. Subsequently, an event  $G_i^x$  is chosen from all possible processes of that class  $L_x$ . The index of the process is determined by using a uniformly distributed random number  $I \in [0, l_x)$ . The chosen growth event is then attempted. After the attempt, irrespective of the outcome, simulation time is increased according to Equation 5.14.

Each attempted growth event has two possible outcomes: the event is either successfully carried out, or the insertion of the triangle fails. In this case, time progresses without any change to the system. Within each class, the lists containing the possible growth events  $L_x$  can be split into two subsets at any time. The first subset,  $\hat{L}_x$ , contains those events which could be grown successfully at that time; their number is denoted as  $\hat{l}_x$ . The corresponding number of events that would fail is denoted as  $\bar{l}_x$ ; the subset containing these events is  $\bar{L}_x$ .

If the growth event belongs to the  $\hat{l}_x$  successful growth events in class  $x$ , is carried out and removed from the  $L_x$ . In this case, the growth site will be deactivated by deleting all events  $G_i^x$  originating from that site. For example, in a growth model with bifurcation and sheet growth, a successful sheet growth attempt leads to the deletion of the two bifurcation events that were possible from the same site. If the newly grown triangle occupies a neighbouring position of a previously grown triangle, the corresponding growth sites are detected and deleted. If the growth event belongs to the failing events in  $\bar{L}_x$ , it is simply deleted from  $L_x$  and time progresses as before.

The presence of not-executed events in KMC methods has been discussed in the literature. Chatterjee and Vlachos show that for *null-event*-Monte Carlo the average time increment can be obtained using the same expression as rejection-free methods [92]. Serebrinsky has come to similar conclusions [185].

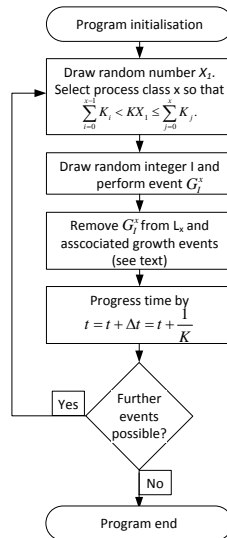


Fig. 5.6 Flow diagram of the KMC procedure. In the first step, the class of process (planar growth, bifurcation, layering, tilted layering) is determined. One process belonging to that class is chosen with equal probability and attempted. After deleting processes which have become impossible now, time is increased by  $\tau$  and the next iteration begins

### 5.4.2 Implementation details

The triangular segments of the sheets were kept track of as triangles, using a self-developed library adopting ideas from the computational geometry library CGAL [186]. Random vectors were needed frequently and found using the method proposed by Muller [187]. Intersection detection between newly inserted triangles and previously deposited sheets was implemented efficiently by a three-staged sequence: each triangle is kept in a spatially resolved list, thus limiting the intersection tests to be carried out only to triangles in the vicinity of the new triangle [188, 189]. In a second step, the axis-aligned bounding boxes (AABB) between two triangles is tested for intersection [189], and only if this relatively cheap test indicates that intersection is possible, an exact test is conducted. The exact intersection test is the popular Gilbert-Johnson-Kerthi (GJK) algorithm, which allows efficient overlap detection between convex polygons [189, 190].

The algorithm was implemented in Java, a decision made in favour of rapid development at the expense of some performance. Typical wall clock times for code execution were about one day for the runs 3-6 in Table 5.1 on a server with 128 GB memory and two Intel Xeon E5-2680 CPUs with 20 MB cache and 2.7 GHz. Whilst no particular measures were undertaken to parallelise the code and it was hence executed serially, multiple cores were used by Java's garbage collector when invoked. The memory requirement for one of the runs mentioned above was in the order of 100 GB, thus, performance problems are more a

problem of memory requirement than due to the demand of computational time. This is likely to be caused by an overhead on the Java objects used for triangles and vertices, and growth events. However, the potential for optimisation of the current version of the program has not been fully explored yet.

## 5.5 Results

The model parameters used to generate the results presented in this section are summarised in Table 5.1. The relatively simple models, namely, sheet growth and sheet growth with layering, were relatively quick to run, so averaging over multiple runs was possible within a reasonable time. Since runs of more complicated models take more computational time, it was decided not to average over many runs. However, trials showed that whilst the kinetics seem to be variable for small clusters, the growth behaviour for large clusters seems to be robust. Since the purpose of this work is to explore the parameter space, it was decided not to investigate the statistics of the model in great detail. The section is split into two parts. During the first three sections, growth of clusters of three models is investigated. In the second part, these growth models are studied in space filling scenarios.

### 5.5.1 Single sheet growth

In this section, individual sheet growth is studied in a large domain. Growth was terminated when the first sheet reached the domain boundary. The kinetics are analysed using an Avrami plot, which effectively assumes the equation  $N = A_N t^n$  to hold. The growth exponent,  $n$ , and the prefactor,  $A_N$ , are determined as a function of time.

The raw data is plotted in Figure 5.7a and the model parameters are given in Table 5.1. The plot in Figure 5.7a shows a straight line, indicating a power law as predicted by Equation 5.5. The derivative of the Avrami plot shows that the initial growth exponent is about 0.5, which then increases towards a value of about 2.3, followed by a slow decrease towards 2. Equation 5.5 predicts a value of 2, which is approached for very large clusters in the long-time limit. The prefactor seems to approach a value of 5.5 in the long-time limit, as seen in Figure 5.5e, apparently in good agreement with Equation 5.5. However, the length of the simulations is not sufficient to demonstrate this behaviour with certainty.

The same picture emerges if the radial growth rate of the sheet is considered. The sheet radius was approximated from the radius of gyration as  $r^2 = 2r_g^2$  and is plotted in 5.7b versus time. As proposed in Section 5.3.3, the radius grows approximately linearly with time for small structures and approaches linear growth for large structures, as can be seen in Figure

Table 5.1 Parameters for the growth models presented in this chapter.

Sec.	#	Dom. size/ $L^3$	$h/L$	$d/L$	$k_L/k_S$	$k_B/k_S$	$\gamma_B[^\circ]$	$k_N L^3/k_S$	Runs
5.5.1	0	$400^3$	0.1	-	-	-	-	-	100
	1								
	2								
5.5.4	3	$400^3$	0.85	-	-	-	-	$10^{-6}$	1
	4							$5 \times 10^{-7}$	
	5							$10^{-7}$	
	6							$10^{-8}$	
5.5.2	9	$150^3$	0.5	0.5	10	-	-	-	10
	10				1				
	11				0.1				
5.5.5	12	$250^3$	0.5	0.5	1	-	-	$10^{-6}$	1
	13				10				
	14				$10^{-3}$				
	15				$10^{-7}$				
5.5.3	16	$200^3$	0.1	-	-	$10^{-2}$	11	-	1
	17	$10^{-3}$							
	18	$300^3$				$10^{-2}$			
	19	$200^3$				$10^{-3}$			
	20	$300^3$				$10^{-2}$			
21	$200^3$	$10^{-3}$	85						
5.5.6	22	$350^3$	0.85	-	-	$10^{-2}$	11	$10^{-6}$	1
	23					45			
	24					85			

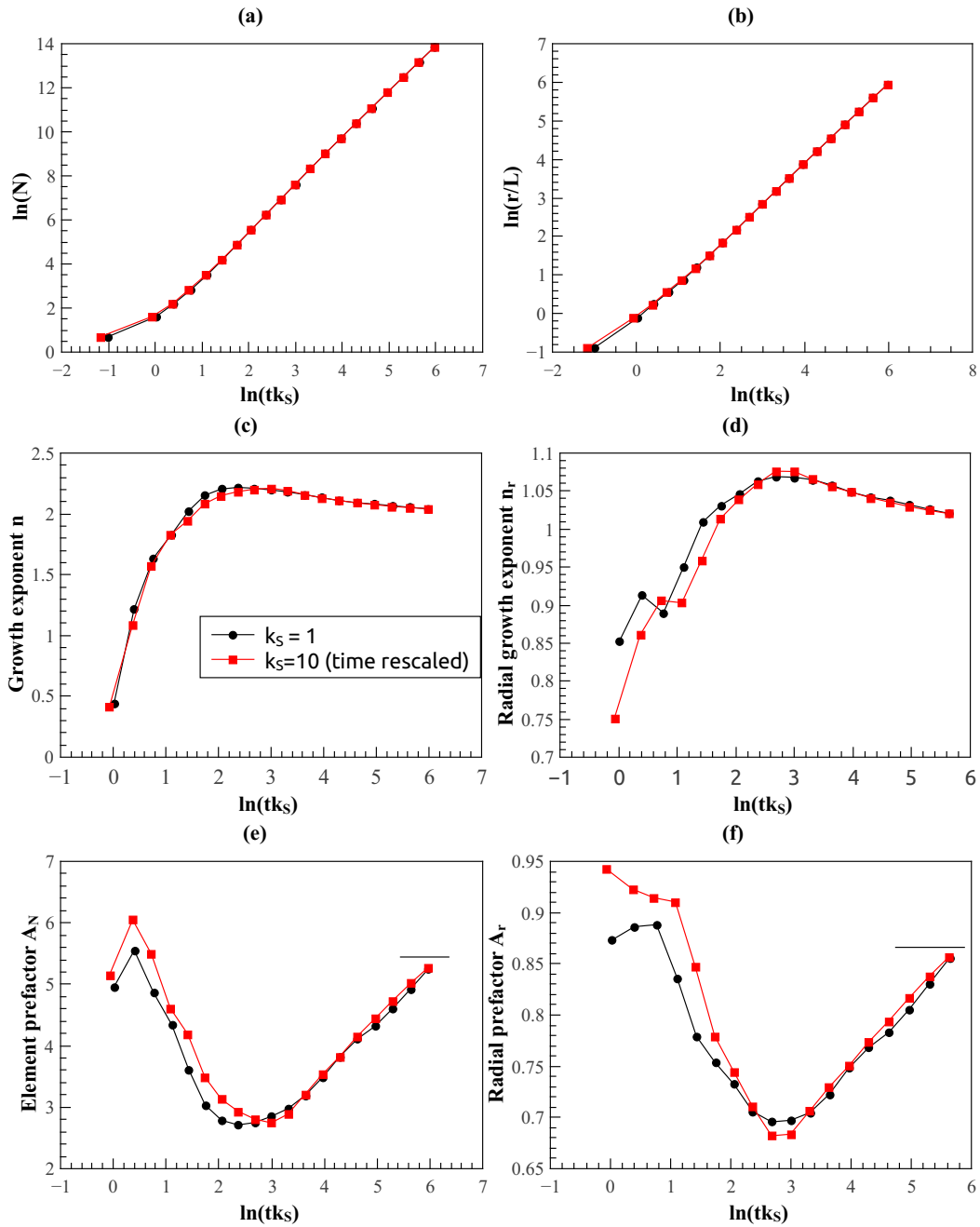


Fig. 5.7 (a) Double logarithmic plot of the number of segments in the cluster versus time. (b) Double logarithmic plot of the radius of the grown sheet versus time. (c) The growth exponent as a function of time obtained by taking the derivative of (a). (d) Radial growth exponent of the sheet. (e) Element prefactor  $A_N$  and (f) radial prefactor  $A_r$  as a function of time. The lines in (c) and (e) are the expected values according to Equation 5.5 and assumed radial growth rate respectively.

5.7d, in which the radial growth exponent approaches 1 for large structures. The assumption from Section 5.3.3 of the radial growth rate approaching  $\sqrt{3}Lk_S/2$  can be confirmed for large clusters, as shown in Figure 5.7f.

These results show that Equation 5.5 can be used to approximate the area of a sheet as well as the radius of each sheet as it grows, as approximately  $r = \frac{\sqrt{3}}{2}Lk_S t$ . This expression will be used to understand the mutual interaction of the grown sheets in later sections.

## 5.5.2 Growth of a sheet crystal: sheet growth and layering

In this section, growth of sheets combined with the aligned layering mechanism is investigated. The model parameters are given in Table 5.1. In Figure 5.8, cross sections through the three clusters grown are shown. It is apparent that the ratio  $k_L/k_S$  controls the anisotropy of the structure. The structures are approximately ellipsoids with an aspect ratio of approximately 1:2. Note that for the left structure shown the sheets are oriented perpendicular to the large aspect, whilst for the second structure they are aligned with the largest aspect.

The kinetics are plotted in Figure 5.9. Figure 5.9a shows the number of triangles in the structure versus time, Figure 5.9c the evolution of the growth exponent in time. It increases for all runs shown from values between 1 and 1.5 towards a maximum at about 3.5, and decreases towards 3 for longer times. The position of the maximum depends on the ratio  $k_L/k_S$ . This picture agrees with the behaviour of the radius of gyration, which is plotted as a function of time in Figure 5.9b. The radial growth  $n_r$  exponent is plotted in Figure 5.9d. It increases from values between 0.9 and 0.6 towards about 1.1, and decreases then towards 1.0 again. The position of the maximum agrees with the maximum growth exponent. In Figure 5.9e and f are the values of the prefactors  $A_N$  and  $A_r$  are shown. Their values seem to approach constant values in the long time limit, consistent with a power law describing growth. The actual value of the prefactors  $A_N$  and  $A_r$  depends strongly on the ratio between the rates for sheet growth and layering,  $k_L/k_S$ .

This behaviour is analogous to a three-dimensional Eden model. The new triangles form a prismatic lattice. This leads to three-dimensional Eden-like growth with anisotropic growth rates. Thus, the limiting growth exponent approaches 3, so the characteristic size of the cluster increases approximately linearly. The anisotropy of the clusters depends on the ratio between the sheet growth rate and the layering rate,  $k_L/k_S$ , in a complex way. The author of this thesis has not investigated this systematically yet.

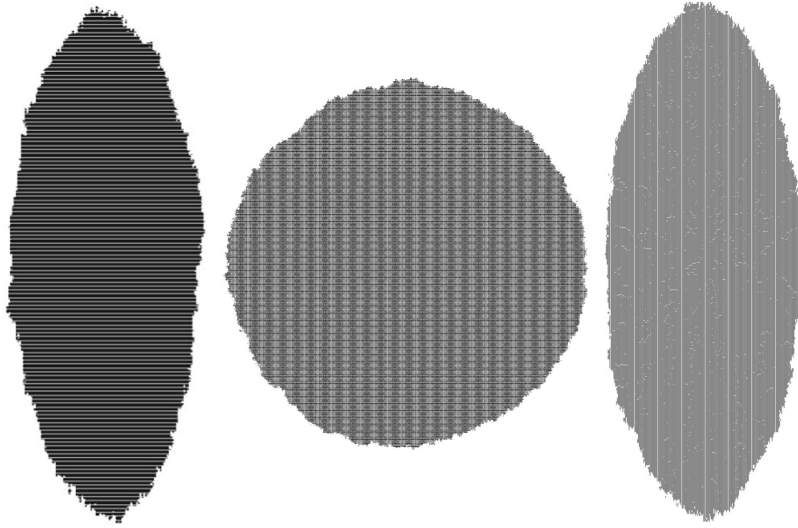


Fig. 5.8 Cross sections through the clusters discussed in Section 5.5.2. The dimension in main direction is about  $150 \cdot L$ . From left to right:  $k_L/k_S = 10$ ,  $k_L, k_S = 1$ ,  $k_L/k_S = 0.1$ . Note that (i) that in the left cluster the sheets are oriented perpendicular to the main direction and that in the right cluster the sheets are aligned with the larger aspect. (ii) the aspect ratio for the two anisotropic shapes is about 1:2.

### 5.5.3 Sheet growth and bifurcation

In this section, sheet growth and bifurcation from a single nucleus is investigated. The parameters are given in Table 5.1. Growth was always stopped as soon as a segment intersected with the domain boundary to exclude boundary effects. Example structures are shown in Figure 5.10. The structures sample three-dimensional space. Those clusters grown with  $\gamma_B = 45^\circ$  and  $\gamma_B = 90^\circ$  are approximately spherical, whilst the cluster grown with  $\gamma_B = 11^\circ$  has a doughnut-like shape. The inspection of the three cross sections through the structure reveals orientational anisotropy in the clusters.

The kinetic data for the growth of clusters with growth and bifurcation is shown in Figure 5.11. Figure 5.11a and c show the Avrami plot and the derived growth exponents for the clusters. Figures b and d show the radius of gyration plotted against time and the associated radial growth exponent.

Those curves obtained for models with a bifurcation rate of  $k_B = 0.01$  are referred to as high bifurcation rate, those which had a bifurcation rate  $k_B = 0.001$  are referred to as low bifurcation rate. Three bifurcation angles  $\gamma_B$ ,  $11^\circ$ ,  $45^\circ$  and  $85^\circ$ , were investigated for both groups.

The growth exponent, Figure 5.11c, always takes initial values between 1.0 and 1.5 and increases subsequently to a value of 2.0. If the bifurcation rate is high, the growth exponents

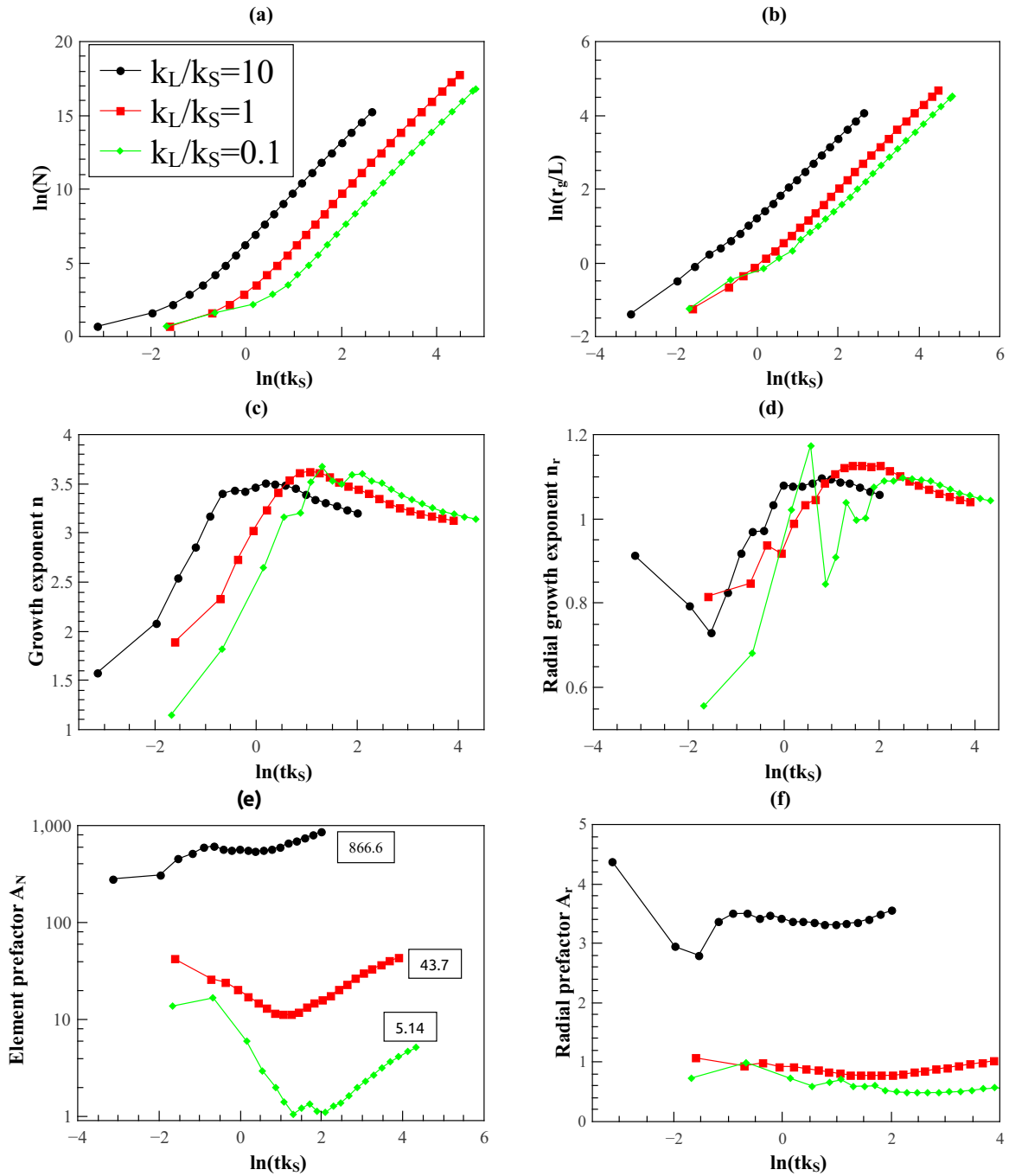


Fig. 5.9 (a,b) Double logarithmic plots of the raw data for the number of segments in the layered sheet cluster and its radius of gyration. (c) Growth exponent for the sheet clusters for different parameters. The long-time behaviour always approaches three. (d) Radial growth exponent for the radius of gyration. In all cases shown, it approaches one for large clusters (e) Prefactors for the power laws the number of sheets in the sheet cluster  $N(t) = A_N t^n$ . (f) Prefactor for the power-law  $r_g(t) = A_r t^{n_r}$  for the gyration radius of the sheet cluster.

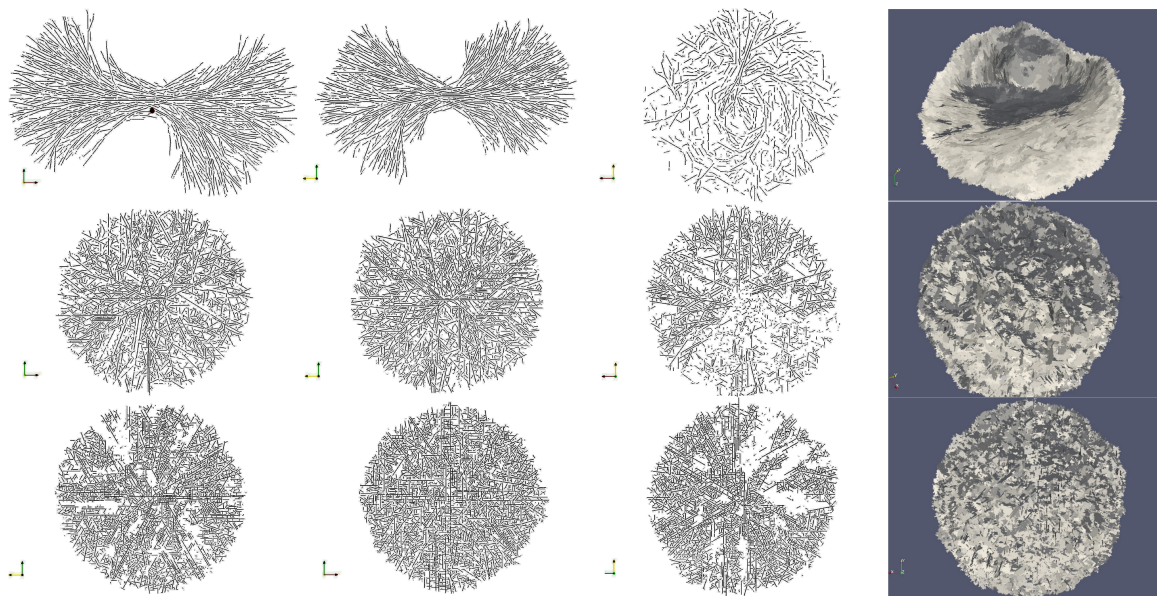


Fig. 5.10 Cross sections through clusters grown by combining planar sheet growth with bifurcation. The first three columns show different the  $yz$ -,  $xz$ - and  $xy$ -cross sections through the clusters. The last column shows a three-dimensional rendering of the cluster. The first row shows clusters grown with a bifurcation angle  $\gamma_B = 11^\circ$ , the second with  $\gamma_B = 45^\circ$  and the last one with  $\gamma_B = 90^\circ$ . Note the isotropy of the clusters which becomes apparent by inspection of the different cross sections. The bifurcation rate was always  $k_B = 0.01$ . The cross sections shown was obtained on different simulation runs than those used to analyse the kinetic parameters.

increase directly towards 4.0 and 4.5. If the bifurcation rate is low, the growth exponent seemed to plateau at a growth exponent of 2.0 for a while, before increasing further towards peak values between 4 (for the 85° case) and 5.1 (for the 45° case). The growth exponents decrease after the peak and seem to approach values close to 3.0 for the models with high bifurcation rate. The shape of the curves for the low bifurcation rates is similar to those with high bifurcation rate, which suggests that they should also approach 3.0 for larger structures. Since it was not possible to investigate larger structures with the current version of the code, it remains unclear whether 3.0 is actually approached.

The radial growth exponent  $n_r$  is plotted in Figure 5.11d and shows strong fluctuations for early times between 0.7 and 1.2. As the structures grow, the radial growth exponents seem to approach 1.05 and seem to continue decreasing, but the data does not reach out far enough. Nevertheless, this picture is consistent with the observation for the growth exponents. Due to these strong fluctuations, it was decided not to calculate the prefactors  $A_N$  and  $A_r$  for the bifurcation clusters.

It is notable that for the models with low bifurcation rate, the time of the maximum seems to be less dependent on the bifurcation angle  $\gamma_B$  than for those models with high bifurcation rate.

The observed growth exponents between 4 and 5 indicate that a second generation of bifurcation sheets causes internal impingement, leading the growth exponent to decrease. The results provide evidence that the growth exponent will eventually approach 3.0 for the structures generated. However, this conclusion has to be taken with care. This behaviour is expected since all growth sites within the cluster will eventually stop being active, leaving only those sites at the convex hull of the cluster available for growth. Since the surface for a three-dimensional object scales with its characteristic length to the power of 2, the growth exponent of such a structure must become 3 if growth is proportional to the convex hull of the structure [173].

#### 5.5.4 Space filling by growing sheets with continuous nucleation

In this section, the results for the model of space filling by sheet growth with continuous nucleation (Figure 5.3b) are presented. The parameters are given in Table 5.1. Two different situations are compared: in Case A, the nucleated sheets can only take three perpendicular orientations, this is Kooi's model [183]. In Case B, the orientation of each nuclei is randomly chosen. Both situations are contrasted by comparing the cross sections shown in Figures 5.12 and 5.13.

Figure 5.12 shows Case A, which means that the sheets were only allowed to have three different orientations. The left column shows structures evolved to about 50 %, and the

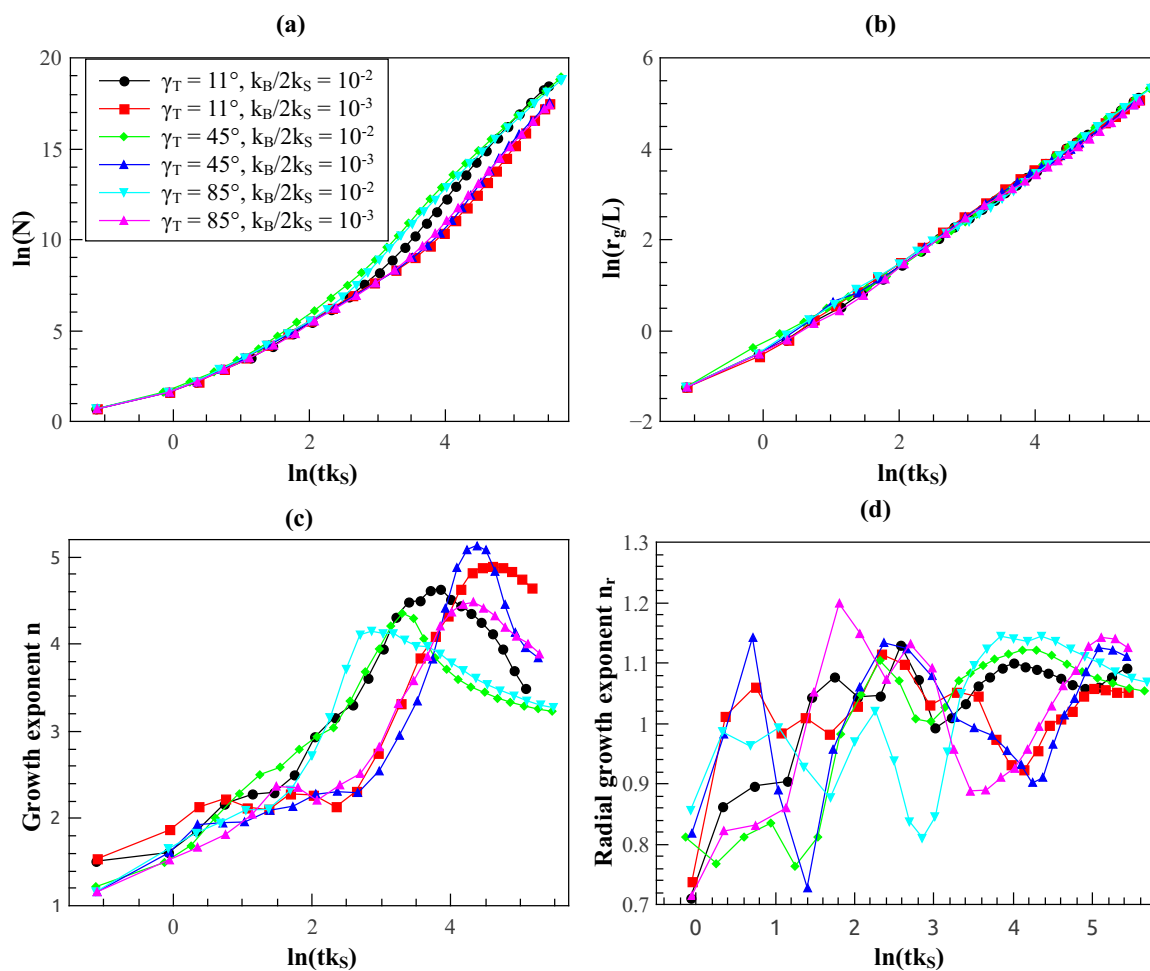


Fig. 5.11 (a,b) Number of segments in cluster and radius of gyration sheet growth and bifurcation versus time. (c) Growth exponent  $n$  plotted versus time. (d) Radial growth exponent plotted versus time.

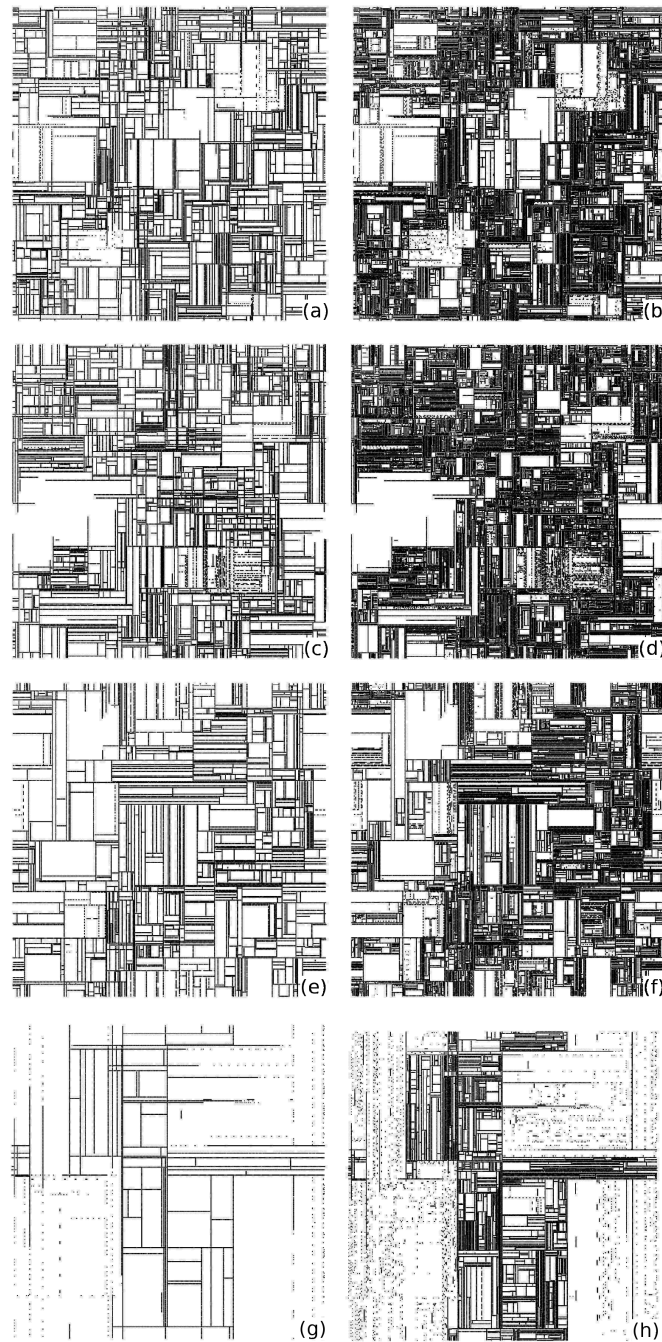


Fig. 5.12 Cross sections through structures grown for Case A. The first column shows structures evolved to about 50 %, the second column shows the final structures. The visualisations are in the same order as the parameters in Table 5.1.

right column shows final structures. From top to bottom, the bulk nucleation rate increases. Details are given in Table 5.1. The cross sections through intermediate structures show rectangularly shaped pockets of empty space of different sizes. Large white areas indicate space where the normal vector of the sheets in this area is normal to the plane of the cross section. In three-dimensions, the pockets are rectangular cuboids. The size of the pockets decreases with increasing nucleation rate. As the structures evolve, the pockets are filled by shorter sheets.

A similar picture shows Figure 5.13, which describes Case B. The newly inserted nuclei were allowed to take a randomly chosen orientation on the surface of a unit sphere. The Figure is organised as Figure 5.12, with the bulk nucleation rate increasing from top to bottom. Similarly to Case A, pockets of empty space, bound by sheets, are formed. These are of polygonal shape in the cross section, indicating that they are actually polyhedra in three-dimensional space. As the structures evolve, the pockets are filled up by smaller sheets.

Figure 5.14 shows the Avrami plots and derived growth exponents as a function of simulation time for both situations. The growth exponent exhibits three distinct regimes: the initial growth exponent is approximately 0.6 and increases quickly to a value of slightly larger than 3.0. It remains approximately constant for a while, followed by a steep decrease, after which the growth exponent increases again to a value close to 0.3, following which it decreases slowly. The value of the exponent in this third regime seems to be slightly dependent on the nucleation rate, being close to 0.2 for those runs with higher and approaching 0.3 for those with lower nucleation rate.

The initial behaviour of the model is due to the growth kinetics of the sheets. In Section 5.5.1, it is shown how clusters (sheets) evolving from nuclei start with low growth exponents, which increase towards values slightly in excess of 2.0 and decreases slowly. This is the picture observed here, but the growth exponent takes a value of three due to the continuous nucleation regime. The sharp drop in the growth exponent is caused by the impingement of the sheets.

Simulation time,  $tk_S$ , was rescaled in the data presented by the time for the expected first impingement, as given by Equation 5.10. The constant  $C_2$  was chosen as 2 from visual comparison against the simulated data, the radial growth rate was  $\dot{r}/k_S = \sqrt{3}L/2$ . The regime following the steep decay of the growth exponent is the blocking regime according to [183]. Equation 5.11 suggests a growth exponent of  $1/3$  in this regime, which is only reached by the simulation for Case A with the lowest nucleation rate. This is probably caused by the finite size of the nuclei. As the structures evolve and the free spaces between the pockets of sheets fill up, fewer nuclei can be inserted, which decreases the growth exponent. In

addition to this finite size effect, it is also noted that anisotropy of the nuclei can have an effect of the growth rate as well. This is the case when the sheets are very thin, such that the nucleus-triangles can only be inserted aligned to the sheets if inserted close to a surface of the structure grown.

It is notable that Case A, Kooi's model, and Case B behave more or less comparably.

### 5.5.5 Sheet growth and layering: space filling by sheet crystals

In this section, space filling by growing sheet crystals is studied. Sheet crystals form if the sheet growth and the layering mechanisms are active in a continuous nucleation scenario, as discussed in Section 5.5.2. The parameters for the simulations are shown in Table 5.1. Cross sections through resultant structures are shown in Figure 5.15.

The first column of Figure 5.15, reports cross sections through structures evolved to about 50%; those in the last column shows the final structures. The ratio  $k_L/k_S$  decreases from top to the bottom row. This pushes the aspect ratio of the clusters growing from single seeds from a cigar-shaped ellipsoid via a sphere towards a flat oblate ellipsoid. This emerges from the first three rows of Figure 5.15. The intermediate structure shown in Figure 5.15g has only a few layer repetitions, indicating that the layering rate is so low that layering plays only a minor role compared to nucleation and sheet growth. The structure appears similar to those shown for the sheet growth and continuous nucleation scenario discussed in Figure 5.14.

The kinetic data is shown in Figure 5.16. In all cases shown, the initial growth exponent is close to one and increases monotonically at first. Then, the different runs exhibit different behaviour. The growth exponent in the first two runs, for  $k_L/k_S = 1$  and  $k_L/k_S = 10$ , increases towards a value close to 4.5, and slowly decreases subsequently towards about 4.2. The evolution of the structures terminates after a steep decrease.

The growth exponent observed for the model with  $k_L/k_S = 10^{-3}$  increases towards 3, seems to plateau a short while and increases subsequently towards 4. This is followed by a sharp drops towards a shoulder at about 1, before dropping to 0. If the layering is much slower than the sheet growth,  $k_L/k_S = 10^{-7}$ , the maximum growth exponent is only slightly larger than 3. After staying at about 3 for a short while, it drops towards a value of approximately 0.3 and decreases slowly. The curve appears to be very similar to those shown in Figure 5.14, confirming the observations made previously on Figure 5.15.

The different behaviour of the models are caused by the anisotropy of the growth model due to different ratios  $k_L/k_S$ . If the ratio is close to 1, the growing clusters have only mild anisotropy and therefore, the KJMA Equation 5.1 should be applicable. The initial behaviour for small clusters is always due to the initial stabilisation of the growth kinetics and

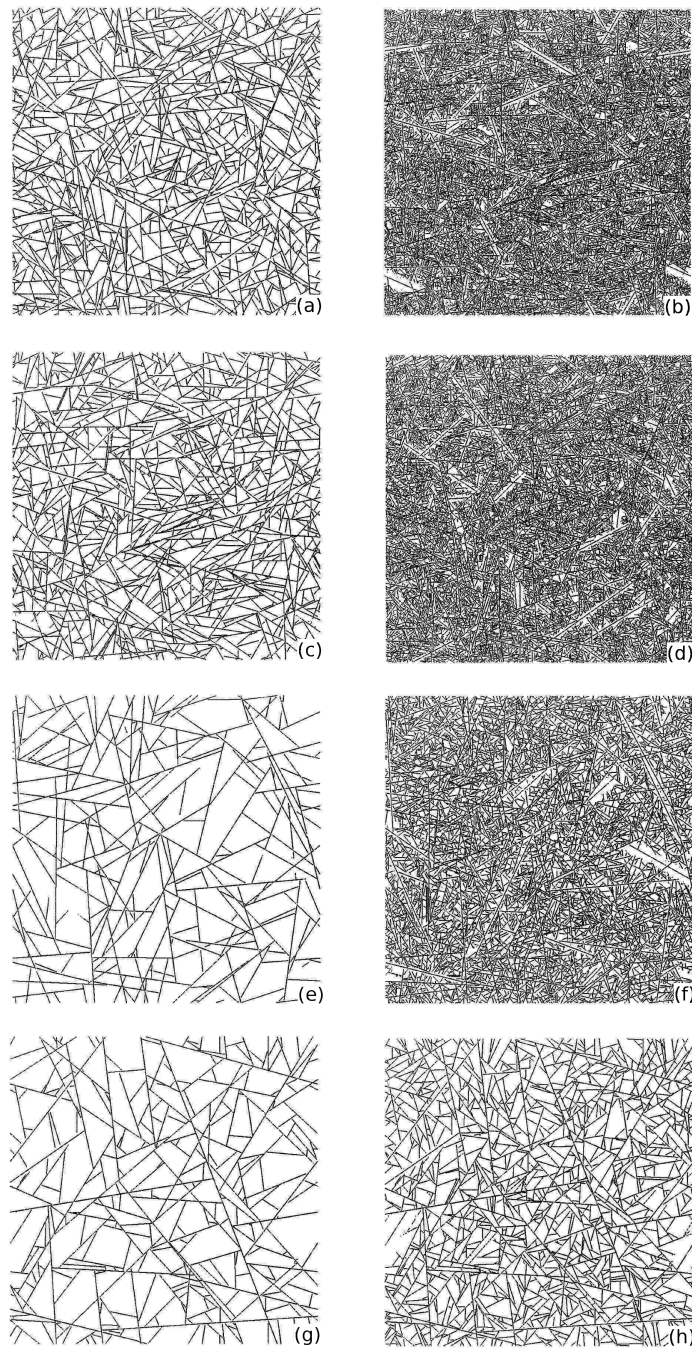


Fig. 5.13 Cross sections through structures grown for Case B. Left column contains structures evolved to approximately 50%. Right column: structures at the end of the simulation. The visualisations are in the same order as the parameters in Table 5.1.

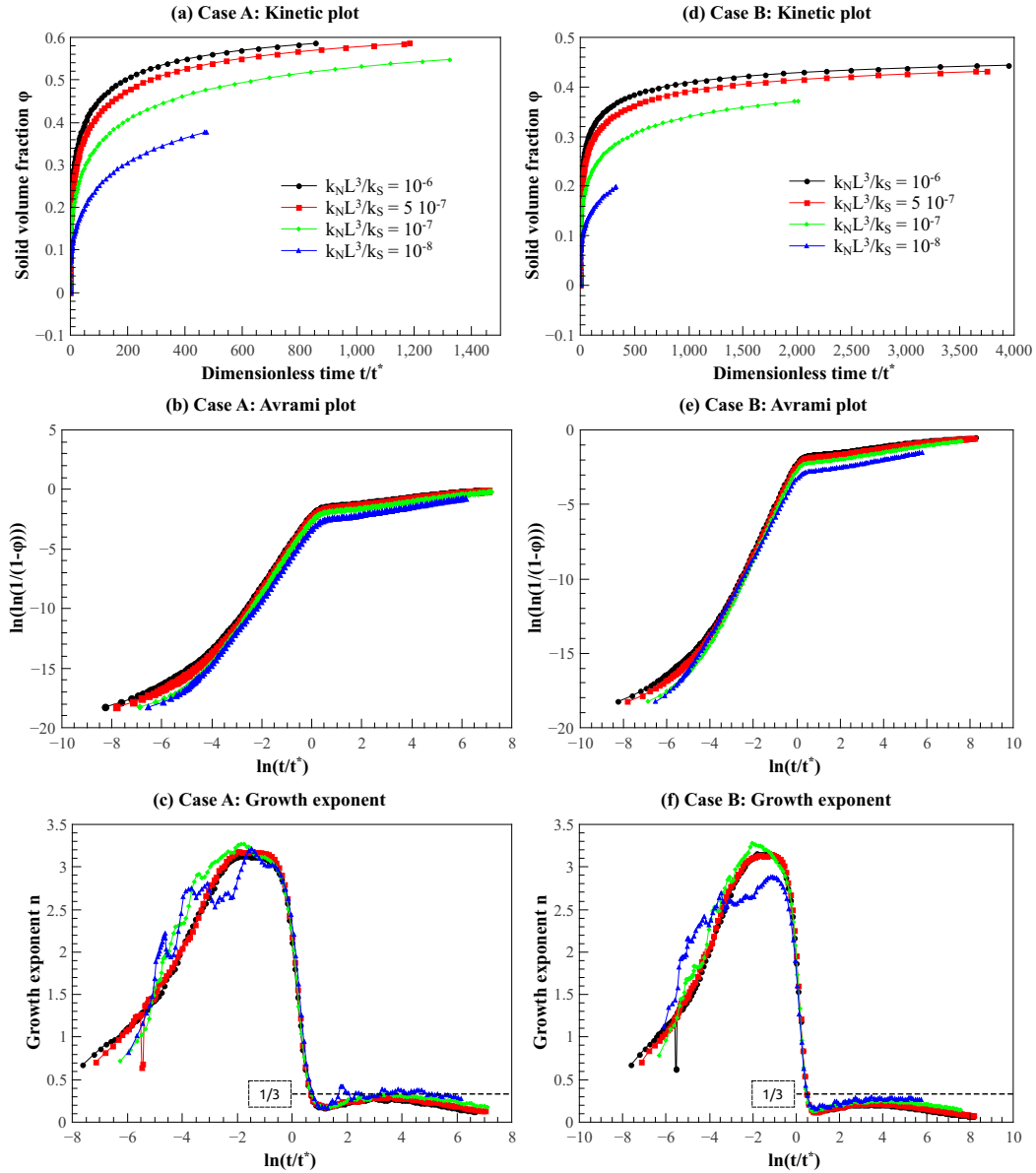


Fig. 5.14 Kinetic plots for space filling by sheet growth with continuous nucleation. The left column shows the plots for Case A, the right column for Case B. (a,d) shows the raw data, (b,e) the corresponding Avrami plots, and (c,f) the derived growth exponents.

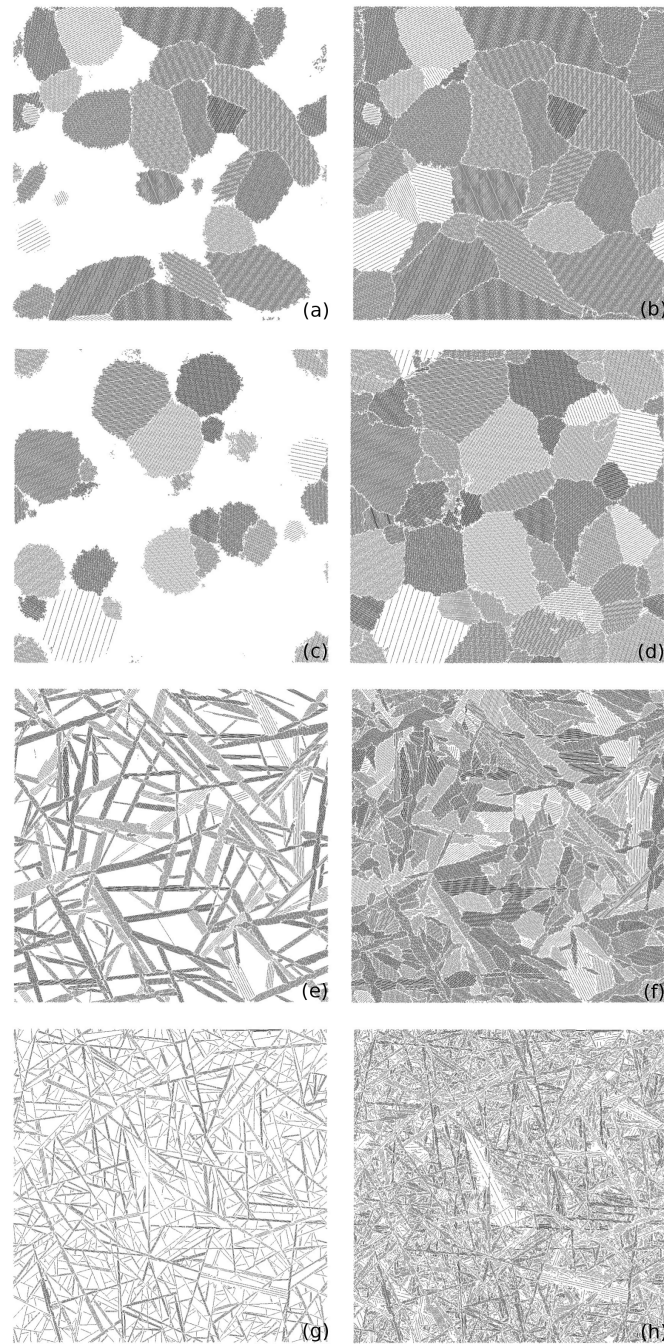


Fig. 5.15 Example structures for space filling by sheet crystals. First column: ca. 50% evolved, second column: final structures. The visualisations are in the same order as the parameters in Table 5.1.

is similar to the observations in Section 5.5.2, where it can be seen that the time exponent of the cluster volume reaches 3.5 before it approaches 3. Therefore, the peak value of the growth exponent reaches 4.5. The sharp decay of the growth rate is due to impingement of growth from the different clusters. This deviation from the KJMA equation is caused by the numerical growth model. A small gap remains between impinging clusters due to the finite size of the inserted triangles. These gaps are about 5 % of the final structures for the simulations shown in this section. One expects the KJMA equation to be highly sensitive to this detail, as can be shown by a series expansion of the KJMA equation, Equation 5.1:

$$\varphi(t) = 1 - \exp(-kt^n) \approx kt^n - \frac{1}{2}k^2t^{2n} + \frac{1}{3}k^3t^{3n} \dots \quad (5.17)$$

As long as  $t$  is small, only the first term contributes to the model. Thus, the Avrami plot gives the correct growth exponent. The higher order terms are sensitive to small changes. When two of the clusters impinge, the gap is not accounted for in the solid fraction, whilst the gap effectively increases the radius of both clusters slightly. Thus, compared to the KJMA equation, the numerical growth model "overestimates" impingement, leading to the rapid decay of the growth rate.

In the run with  $k_L/k_S = 10^{-3}$ , the time scale between sheet growth and layering is separated due to the small value of  $k_L/k_S$ . Thus, the growth exponent reaches a value of about three first and the model behaves like a pure sheet growth model. Only after a while the layering starts playing a role, leading to the increased growth exponent before the impingement of the growing shapes. The shoulder with a growth exponent of about 1 and a logarithmic-time of 5 is the remaining space filling by slow one-dimensional growth due to layering. This can also be seen in the works of Pusztai and Shepilov [180, 181]. Comparison of Figures 5.15e and f shows how spaces in the intermediate structure are mostly filled by layering, which is an essentially one-dimensional process.

In the model with  $k_L/k_S = 10^{-7}$ , time scales of growth and layering are so strongly separated that layering only plays minor a role before impingement. Therefore, the growth exponent barely exceeds 3.0, which shows that the model behaves like a model of impinging sheets. The influence of layering after impingement remains negligible as well, since the curve has the same shape as pure sheet growth with continuous nucleation (see Section 5.16). Therefore, the cross sections of the structures appear to be similar to those shown in that section.

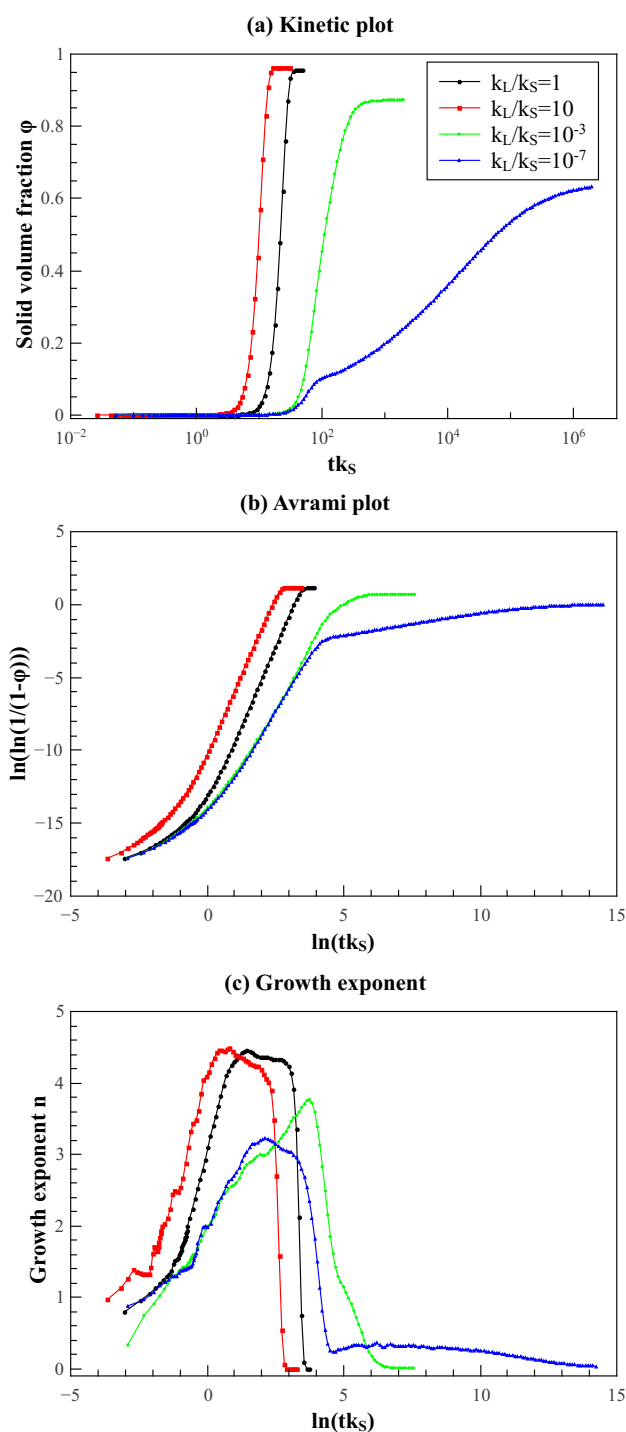


Fig. 5.16 Kinetic plots for space filling by sheet crystals (sheet growth and layering) and continuous nucleation. (a) Shows the raw data, (b) the Avrami plot and (c) the derived growth exponent.

### 5.5.6 Space filling by sheet growth with bifurcation

In this section, space filling is investigated in a continuous nucleation scenario, with clusters growing by the sheet growth and bifurcation mechanisms. The parameters are given in Table 5.1.

In Figure 5.17, cross sections through intermediate structures are shown in the first column and evolved structures in the second. The changing parameters between the rows is the bifurcation angle  $\gamma_B$ , which take the values  $11^\circ$ ,  $45^\circ$  and  $85^\circ$ . Figure 5.17a shows elongated packets of sheets, whilst the two other intermediate structures show more spherical clusters. This agrees well with the observations made in Section 5.5.3. The fully evolved structures are dense and disordered. The density appears to be homogeneous.

The kinetic curves are shown in Figure 5.18. The initial growth exponent is about 1.0 and increases towards a maximum of about 5.0. Subsequently, the growth rate drops sharply and the evolution of the structure terminates.

The initial increase of the growth exponent is following the undisturbed cluster growth kinetics, which has already been studied in Section 5.5.3. The maximum value of the growth exponent reaches about 5.5, before dropping sharply. This indicates that impingement between different clusters becomes important before the growth exponent decreases due to the internal impingement of the sheets formed by bifurcation, as found in Section 5.5.3.

The sharp decrease of the growth exponent shows that the porous clusters formed by sheet growth and bifurcation impinge like hard spheres. The clusters do not seem to grow into each other, leading to a fairly abrupt termination of growth. This is a similar behaviour to the dense sheet crystals discussed in Section 5.5.5. Thus, the kinetic behaviour of these structures might be approximated by an KJMA style model, if the radial growth rate is calibrated accordingly.

## 5.6 Discussion and Conclusion

In this chapter, growth of sheets and space filling by the resultant structures was studied. These studies were only possible by introducing a novel off-lattice kinetic Monte Carlo model to describe the growth. Different mechanisms were proposed to allow a two-dimensional growth mechanism to sample three-dimensional space. Some of these mechanisms, such as layering, lead to highly ordered structures. Other mechanisms, such as bifurcation, can potentially create amorphous structures.

It was shown that a simple set of equations can be developed to estimate the growth of a sheet using an Eden model. Sheet growth with continuous nucleation was used as a model for space filling by two-dimensional sheets. The presented results reproduce the

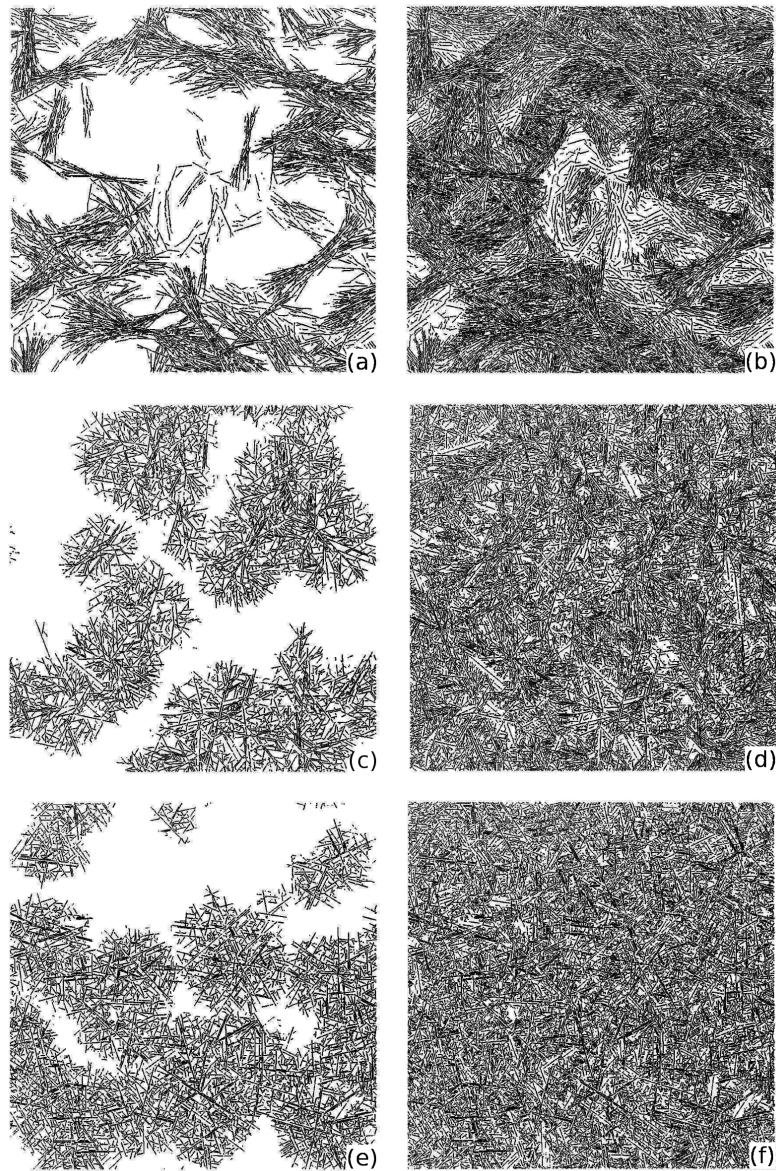


Fig. 5.17 Example structures for space filling by sheet growth and bifurcation. First column: ca. 50 % evolved, second column: final structures. The visualisations are in the same order as the parameters in Table 5.1.

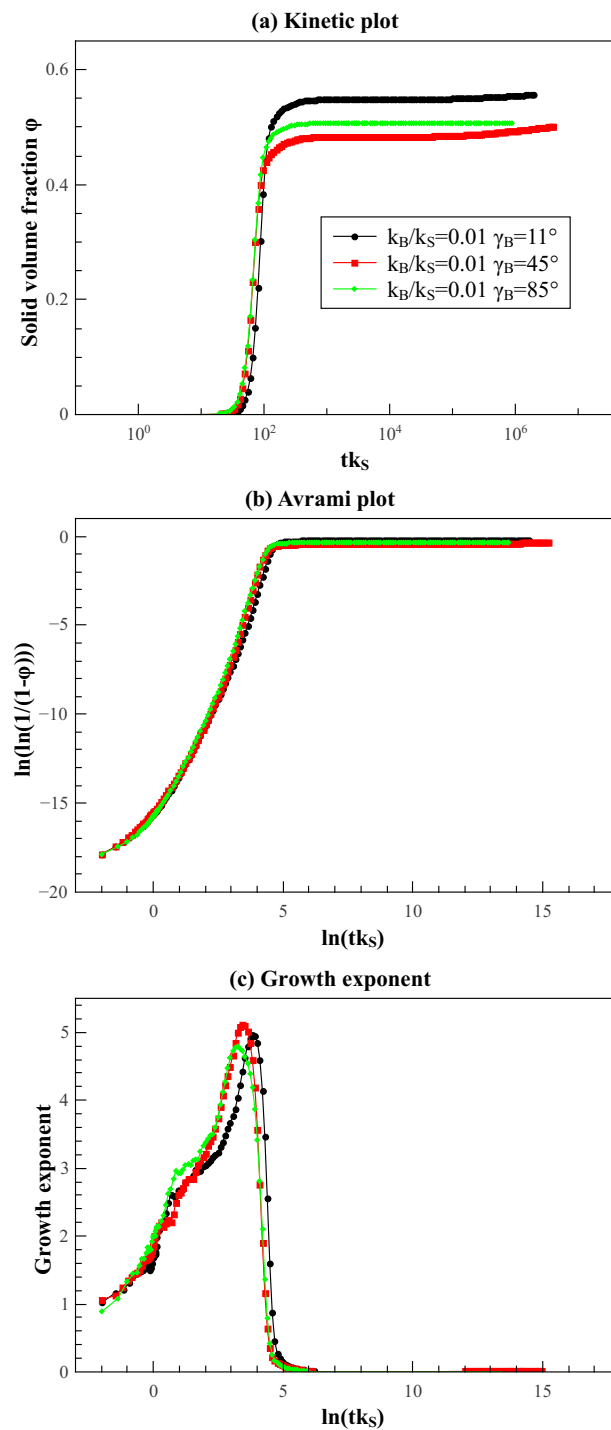


Fig. 5.18 Kinetic plots for space filling by sheet growth with bifurcation and continuous nucleation. (a) shows the raw data, (b) the Avrami plot and (c) the derived growth exponent.

known literature behaviour of a model where the sheets are allowed to take only few selected orientations. These were compared against the model in which the nucleating sheets can be of arbitrary orientation, which is one of the advantages of the new algorithm. Both models exhibit almost quantitatively the same kinetic behaviour. However, be aware that these graphs have log-scales.

Sheet growth in combination with the layering mechanism leads to the growth of massive, bulky structures. Their actual growth rate and aspect ratio depends in a complex way on the ratio between the layering and planar growth rate. As long as the aspect ratio of these structure is close to unity, they reproduce conventional KJMA behaviour within the limit of the discretisation of the sheets.

Introduction of bifurcation allows sheets to sample three-dimensional space in an disordered way. The kinetics for these models develops in different regimes, initially, low growth exponents are observed, which increase towards a maximum. Arguments have been presented as to why the maximum growth exponents are expected to be between 4.0 and 6.0, which matches the simulation results with exponents between 4.0 and slightly above 5.0. Beyond the maximum, the growth exponents seems to decay towards a value of 3.0. This could not be verified yet due to computational limitations. With regards to the initial motivation behind this work, to examine the meso-structure of C-S-H within cement, the author would like to remark that the clusters growing from nucleation and bifurcation resemble early age hydration products of Portland cement (compare Chapter 2). Also, their kinetic behaviour is in line with high Avrami exponents observed for the early stages of Portland cement hydration [37].

Space filling by clusters grown with the bifurcation mechanism exhibits high growth exponents, and a sharp drop in the growth rate. Besides the values of the growth exponents, the curves resemble those of impingement of sheet crystals. This indicates that the bifurcation clusters impinge hard on each other, despite their open internal structure.

The clusters grown with the bifurcation model are of high interest for the cement community, since they form a potentially open and disordered sheet structure from a single nuclei, which is in line with ideas proposed by Garter [8]. Nevertheless, it is anticipated that the model presented in this work will find applications beyond cement, where its fundamental results will be of interest. The results presented indicate that it is desirable to study larger computational domains, which is currently not possible due to the large memory demand. These problems can be overcome by, for example, applying known techniques to re-mesh the grown sheets at a much coarser resolution, thus, drastically reducing the memory demand.

The application of this model towards actual physical systems requires the establishment

of a link towards the experimental data. This may be via the kinetic data itself, as calculated in this chapter, or by further characterisations of the structure. In the next chapter of this thesis, a sheet growth model is applied to the formation of calcium-silicate-hydrates in Portland cement.



# Chapter 6

## A sheet model for the meso-structure of calcium-silicate-hydrate in cement

**Prior disclosure:** this chapter is largely identical to an article published by this author in Cement and Concrete Research [168].

The sheet growth model is used to grow quasi-two-dimensional sheet structures in three-dimensional confinements. These structures are used as a model for calcium-silicate-hydrate forming in the interstitial pore space between cement grains by the reaction of anhydrous cement and water. The generated structures have growth and morphological properties consistent with a range of experimental data.

### 6.1 Introduction

In this chapter, the previously introduced computer model, which grows amorphous three-dimensional structures from a network of disordered two-dimensional sheets, is applied to the growth of the calcium-silicate-hydrates (C–S–H) in cement. The properties of the numerical structures generated are compared to experimental data for cement paste.

The active component of cement paste is calcium silicate hydrate. It forms from a dissolution-precipitation reaction of anhydrous cement powder and water and it is related to minerals like tobermorite and jennite [27]. C–S–H comprises a disordered network of semi-crystalline layers of calcium and oxygen atoms with silica tetrahedra attached, interspersed by water and further calcium ions. Two water environments are commonly identified: the interlayer water, and water in nanoscopic gel-pores between locally aggregated semi-crystalline layers[6]. The nano-structure has been described as combining glass-like

short-range order with some features of the mineral tobermorite [34]. However, this model has been criticised for being inconsistent with the crystal chemistry of other calcium silicates [35]. Most macroscopic properties of cement depend on the details of the C–S–H formed. Despite its importance, the microscopic morphology of C–S–H remains poorly defined and the subject of intense debate [1].

For this work, the meso-scale is defined as structural features ranging from roughly 1 nm to hundreds of nanometres, or, alternatively, bridging the nano scale with the scale of cement paste ( $\mu\text{m}$ ) (see Section 1.2). There are two conceptual models [134] of the meso-scale morphology of C–S–H. On the one hand are colloidal models such as the recent one proposed by Jennings [3]. The underlying particle packings of colloidal models have been used to explain a wide range of apparently contradictory experimental results. The colloidal particles have a characteristic length of *ca.* 5 nm with a layered substructure, where the layers are considered to be chemically similar to those found in minerals like tobermorite and jennite. A hierarchy of nanoscopic pore spaces are identified ranging from the interlayer space, to small pores between disordered layers, particles in small flocs, and between large flocs [4]. An alternative viewpoint includes models such as that proposed by Feldman and Sereda (FS) [5], which describe C–S–H as quasi-continuous, but disordered, layers of sheets. A schematic contrasting the models is shown in Figure 6.1.

Particle models have received considerable attention from the community. Garrault and Nonat based their model for the formation of hydrated layers on tri- and dicalcium silicate surfaces on particle aggregation [41]. Particle-based models have also been used by the group of Ulm to successfully interpret nano indentation results [81]. Small-angle neutron scattering data of cement paste has been interpreted using particle fractal models [30], finding a mass and a surface fractal and a particle diameter of about 5 nm. Livingston proposed a fractal nucleation and growth model, which relates fit-parameters of the growth rate to the fractal structures observed in SANS experiments [191]. This view is also supported by X-ray scattering measurements of Skinner et al. They reported a vanishing pair correlation function beyond a correlation length of 3.5 nm and concluded that synthetic C–S–H has nano-crystalline regions of that size. Whilst particle models have been successfully used to fit/explain a broad range of experimental data, difficulties remain in explaining how such structures may form. Ioannidou et al. addressed this question with a hybrid Monte-Carlo-Molecular-Dynamics model, incorporating molecular features below approximately 10 nm by using an experimentally obtained interaction potential. They showed that morphologies observed in micrographs such as fibrils and columns can be formed [82]. Experimentally it is found that localised growth occurs preferentially on the surface of the cement grains [52], instead of cluster formation in the bulk. Recently, Brisard and Levitz studied the relation-

ship between different particle packings and the expected scattering curves. They conclude that C–S–H cannot be described by monodisperse particle packings and diffusion-limited aggregation. They suggest an Apollonian sphere packing with a power-law distribution of particle sizes, or alternatively a power-law distribution of pore sizes [61]. However, recent NMR experiments by Muller et al. [40] indicate a rather narrow, bi-model distribution of pores in C–S–H, consisting of the interlayer and the gel pore space.

Nevertheless, even in the light of the wide acceptance of particle models, doubts remain. Chiang et al. developed a fit for SANS data based on particles consisting of cylindrical stacks of discs and a fractal pair correlation function. Interestingly, they inferred cylinder heights ranging from 5 nm to 10 nm and diameters between 13 nm and 19 nm for a synthetic C–S–H system equilibrated with different water contents. Such extended sheet regions could also, as they point out, be interpreted as evidence for a quasi-continuous sheet structure [60]. Certainly, this result argues against the idea of 5 nm building blocks. Dolado et al. conducted molecular dynamics (MD) simulations of the polymerisation of silicic acid in the presence of water-solvated calcium hydroxide to study "a prejudice-free" structure formation. They observed the formation of a three-dimensional branched structure with building blocks of similar size to Jennings' particles [134]. They suggest that such a structure may integrate elements, similarly sized as the colloidal bricks in Jennings' model, into a continuous structure.

Phenomenological evidence for the existence of extended sheet-structures can be taken from micrographs of C–S–H both from synthetic systems as well as from cement paste, which often can be described as showing a sheet-like or crumpled-foil morphology [27, 54, 192, 193]. Brisard et al. used transmission X-ray microscopy and associated nanotomography techniques to study cement paste. They showed that the scattering curves can be related to the nano-structures observed [194]. The images could be interpreted both as a quasi-continuous sheet structure or a colloidal aggregate. McDonald et al. used a sheet-model to interpret their NMR results of drying cement paste [6]. Scrivener et al. suggested nano-crystalline regions of sheets, partly linked by other sheets, as a C–S–H structure and suggest that such structures may have a behaviour mechanically similar to a granular material [7]. According to Gartner, such structures could form by two-dimensional-growth of sheets in three-dimensional space; consequently, this results in a quasi-continuous sheet structure [8]. The ideas proposed by Gartner have never been studied numerically and the resultant material properties of quasi-continuous FS-models have never been investigated in three dimensions due to the difficulty of representing such inherently complex structures.

The literature review above demonstrated that colloidal models have received considerable attention, and have been successfully applied to interpret experimental data. In contrast,

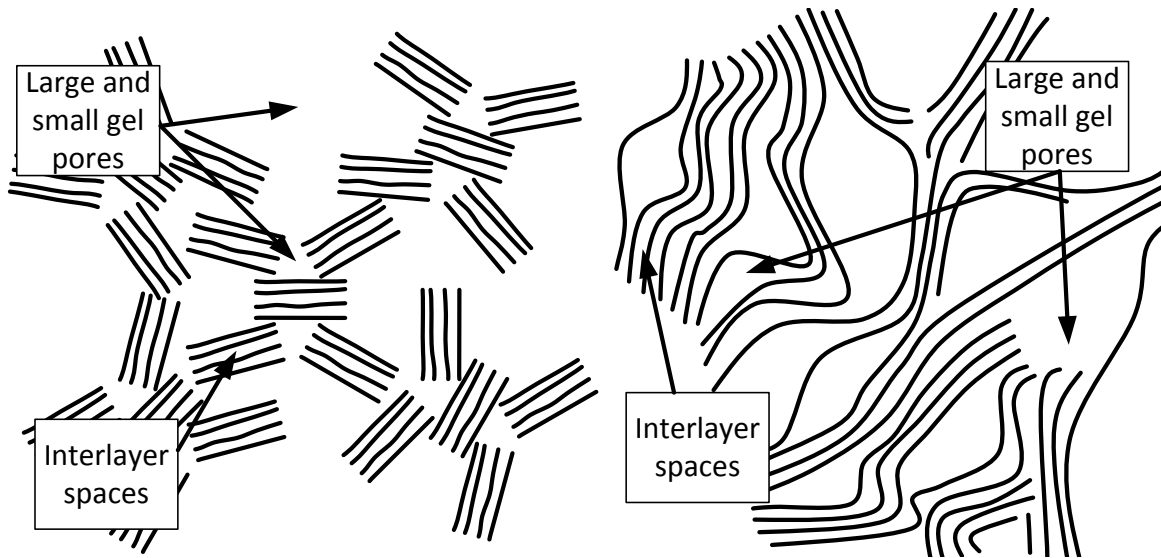


Fig. 6.1 Schematic of the two dominant C–S–H models: **left:** the Jennings model is a hierarchical packing of nano-sized layered particles. **right:** the FS model describes C–S–H as disordered quasi-continuous sheets. Recreated from [4, 5].

quasi-continuous sheet structures have never been theoretically investigated. In this work, we introduce a methodology to numerically generate three-dimensional amorphous structures that have the core-structural properties of quasi-continuous FS sheet models. These can be tested against experimental results for C–S–H. Initial structures are compared to experimental data obtained with small-angle scattering, isothermal calorimetry, nuclear magnetic resonance (NMR)-porosimetry and permeability data.

## 6.2 Application of the sheet growth model to C–S–H

In contrast to the precipitation and aggregation of particles, as modelled by Ioannidou et al. [82], this work is based on a different idea. It is assumed that sheet nuclei form instantaneously at time  $t = 0$  on the surface of the cement grains, before the growth acceleration.

The cement grains dissolve, and C–S–H precipitates at active growth sites on the C–S–H structure. This precipitation is the basis for the model. The motivation for the present work is that C–S–H is assumed to be a sheet due the chemical similarity with tobermorite. This is modelled by assigning the edges of sheets as growth sites. In addition to the planar growth of the sheets, new sheets are assumed to form aligned with existing ones. The modelling idea is similar to the concepts suggested by Gartner [8]. The model adopts a framework to describe arbitrarily shaped surfaces in space based on triangulation. A kinetic sheet growth model with the following seven key elements, based on the hypotheses given above for

cement, as shown in Figure 6.2.

1. Sheets of thickness  $h$  grow within a confined space. Outside of this space, sheets cannot grow.
2. Growth starts from a fixed number of initial nucleation sites  $N_S$ . Nucleation sites are modelled as randomly oriented triangles (prisms) placed on the surface of the confinement space.
3. Planar growth is modelled by adding material to the perimeter of an existing sheet. New triangles are added with a rate  $k_S$ .
4. Layer formation occurs by inserting a triangle a distance  $d$  from existing sheets with a rate  $k_L$ .
5. The pore space sandwiched between aligned layers is called the *interlayer space* and is of width  $d_{il} = d - h$ . It is formed both by layering and growth from previous layering sites.
6. Sheets are not allowed to intersect. Sheets are surrounded by an exclusion zone, which is sketched in Figure 6.2. The exclusion zone of different segments is not allowed to overlap. It prevents triangles from different sheets to be closer than the layer repeat distance  $d$  and prevents growth in the interlayer space.
7. Defects in the structures occur due to the exclusion zone and the triangle side length when sheets collide. Additionally, defective layering events, leading to the insertion of triangles tilted by an angle  $\gamma_T$  with a rate  $3k_T$ , enable control of the number of defects<sup>1</sup>.

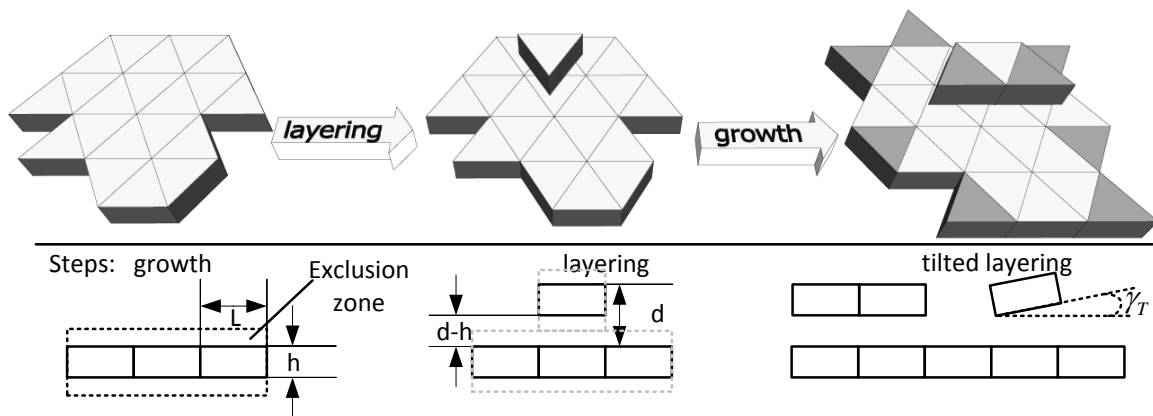


Fig. 6.2 Top: A new triangle is inserted above a layer during *layering*, and at a layer edge during *growth*. Below: definitions of the geometric measures of the model; a tilting event is also illustrated in two dimensions. The dotted grey line illustrates the exclusion zone.

<sup>1</sup>The insertion rate is  $3k_T$ , since three defective triangles are possible at each layering site. See Chapter 5 for details.

In the context of this work, the model is used to simulate the formation of C–S–H in the water-filled capillary pore space between cement grains. Thus, we model the formation of the C–S–H described by some authors as outer product [27]. For the time being, we ignore the formation of inner product and the shrinkage of the cement grains as they are consumed. The capillary space is modelled as a spherical confinement of radius  $R_c = 150$  nm, but provisions have been made to also study more complex confinements, as discussed below. The triangle side length,  $L$ , is 1.5 nm. The layer repeat distance,  $d$ , was chosen as 1.4 nm to fit tobermorite-14 [27, 28]. The sheet height was estimated as  $h = 0.65$  nm on the basis of crystallographic data for tobermorite-14 [28]. The number of initial seeds,  $N_S$ , was arbitrarily chosen as 1688, leading to a surface seed density of  $5969 \mu\text{m}^{-2}$ . This will be discussed in Section 6.5. The tilt angle was chosen as  $\gamma_T = 11^\circ$  on the basis that this leads to wedge-shaped defect pores, analogous to gel pores, with a length-to-thickness ratio of about five, as suggested by NMR data [6].

After initialisation, the structure is evolved until growth, from all growth sites, has been attempted. Intermediate structures are described via a progress variable  $\xi$ , defined as the number of deposited triangles at time  $t$  expressed as a fraction of the total number deposited,  $N_{\Delta}^{Final}$ . The progress variable is analogous to the degree of hydration of cement. Consequently, the time-derivative of  $\xi$  is analogous to the reaction rate measured as a heat-flux in isothermal calorimetry or as a volume-change rate in chemical shrinkage experiments.

## 6.3 Methods

The sheet growth model is described in greater detail in Chapter 5.

### 6.3.1 Pore space characterisation

The pore space in the final structure is characterised with the assumption that all void space can be either assigned to interlayer pore space or the gel pore space. The following definitions are used:

1. interlayer pore space, labelled by the index "il", is the pore space located between two aligned layers with distance  $d$  between the centre of the backbones. The corresponding surfaces are those segment surfaces facing an aligned segment in that distance.
2. the defect or gel pore space, labelled by the index "d", is the remaining pore space which is not occupied by solids. The surface of this pore space is computed by summing up all those triangular facets which do not contribute to the interlayer surface.

The aim of this definition is to obtain values comparable to the view a  $T_2$ -proton relaxometry NMR experiment would obtain. The edges of the sheets were excluded from the definition of the gel pore surface because NMR relaxation occurs mostly at paramagnetic impurities [195], which are most-likely located in the plane of the sheets.

### 6.3.2 Prediction of small-angle scattering curves

Small angle scattering as a method has already been introduced in Chapter 3. Rather than following the described approach by Schmidt-Rohr [97], a semi-analytical procedure is used to predict the small-angle scattering curve.

The contribution of each triangular segment is computed separately. These are added to obtain the scattering intensity in a certain direction, which is then radially averaged. Equation 3.11 specifies that the amplitude of the scattered radiation  $A(\mathbf{q})$  with a scattering vector  $\mathbf{q}$  is the Fourier transform (FT) of the scattering length density distribution. Actual values for the scattering length are ignored here, and the scattering length density distribution is replaced by the indicator function  $I(\mathbf{r})$  [95], which is one if  $\mathbf{r}$  belongs to the solid and zero if  $\mathbf{r}$  belongs to the pore space.

$$A(\mathbf{q}) = \int_V I(\mathbf{r}) \exp(-i\mathbf{r} \cdot \mathbf{q}) d\mathbf{r} \quad (6.1)$$

Since the indicator function is zero outside the sheets, one can write

$$\begin{aligned} A(\mathbf{q}) &= \int_{\text{Sheets}} I(\mathbf{r}) \exp(-i\mathbf{r} \cdot \mathbf{q}) d\mathbf{r} \\ &= \sum_i^N \int_{V \in T_i} I(\mathbf{r}) \exp(-i\mathbf{r} \cdot \mathbf{q}) d\mathbf{r}, \end{aligned} \quad (6.2)$$

where the sum is over all triangles  $T_i = \{\mathbf{V}_i^0, \mathbf{V}_i^1, \mathbf{V}_i^2\}$ . The nomenclature within the triangle is also shown in Figure 6.3.  $\mathbf{V}_i^j$  denotes the  $j$ th vertex of triangle  $i$ . The integral can be evaluated if its coordinates are transformed into the coordinates of the triangle, namely  $\mathbf{r} = \mathbf{O}_i + \mathbf{u}_i s + \mathbf{v}_i t + \hat{\mathbf{n}}_i H$ ,  $s, t$  and  $H$  are parameters. The origin is set as  $\mathbf{O}_i = \mathbf{V}_i^0$ , the three vectors are  $\mathbf{u}_i = \mathbf{V}_i^0 - \mathbf{V}_i^1$ ,  $\mathbf{v}_i = \mathbf{V}_i^2 - \mathbf{V}_i^0$  and  $\hat{\mathbf{n}}_i = \frac{\mathbf{u}_i \times \mathbf{v}_i}{|\mathbf{u}_i \times \mathbf{v}_i|}$ .

The following constraints give the points included in the triangle:

$$\begin{aligned} 0 &\leq s, t \\ s + t &\leq 1 \\ -\frac{1}{2}h &\leq H \leq \frac{1}{2}h \end{aligned} \quad (6.3)$$

$d\mathbf{r}$  is transformed as  $d\mathbf{r} = \det(J_{\mathbf{r}}) ds dt dH$ , where  $\det(J_{\mathbf{r}})$  denotes the determinant of the

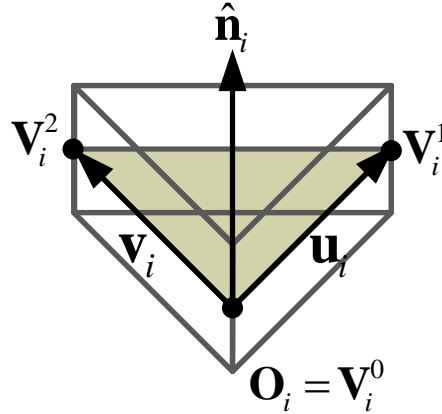


Fig. 6.3 Nomenclature within a triangular segment with height  $h$ . The positions of the vertices of the backbone triangle (dark area) are the black dots and labelled as  $V_i^j$ , where  $j$  is the vertex index within the triangle and  $i$  denotes the  $i$ th triangle. The normalised normal-vector of the backbone triangle is denoted  $\hat{\mathbf{n}}_i$ .

Jacobian of  $\mathbf{r}$ , which reads  $J_{\mathbf{r}} = [\mathbf{u}, \mathbf{v}, \hat{\mathbf{n}}]$ . This leads to:

$$\begin{aligned}
 & \int_{V \in T_i} I(\mathbf{r}) \exp(-i\mathbf{r} \cdot \mathbf{q}) d\mathbf{r} \\
 = & \exp(-i\mathbf{q} \cdot \mathbf{O}_i) \det(J_{\mathbf{r}}) \\
 & \int_0^H \exp(-i\mathbf{q} \cdot \hat{\mathbf{n}}_i h) dh \int_0^1 \exp(-i\mathbf{q} \cdot \mathbf{u}_i s) \int_0^{1-s} \exp(-i\mathbf{q} \cdot \mathbf{v}_i t) dt ds
 \end{aligned} \tag{6.4}$$

The integral can be evaluated, leading to an expression for the the amplitude of the scattered radiation by the complete structure in direction  $\mathbf{q}$ :

$$\begin{aligned}
 A(\mathbf{q}) = & \sum_i \exp(-i\mathbf{q} \cdot \mathbf{O}_i) \det(J_{\mathbf{r}}) \\
 & \left( -\frac{i(1 - \exp(-i\mathbf{q} \cdot \hat{\mathbf{n}}_i H))}{\mathbf{q} \cdot \hat{\mathbf{n}}_i} \right) \\
 & \left( -\frac{\mathbf{q} \cdot \mathbf{u}_i (1 - \exp(-i\mathbf{q} \cdot \mathbf{v}_i)) + \mathbf{q} \cdot \mathbf{v}_i (\exp(-i\mathbf{q} \cdot \mathbf{u}_i) - 1)}{(\mathbf{q} \cdot \mathbf{u}_i)^2 \mathbf{q} \cdot \mathbf{v}_i - \mathbf{q} \cdot \mathbf{u}_i (\mathbf{q} \cdot \mathbf{v}_i)^2} \right).
 \end{aligned} \tag{6.5}$$

This expression enables one to simulate scattering in a single direction  $\mathbf{q}$ .

### Radial averaging

Small-angle experiments measure averaged intensity of the radiation at a set length of the scattering vector over all directions. Thus, the intensity calculated from equation 6.5 was averaged over 200 points on the surface of a sphere for each scalar value for  $q$  in the spectrum.

#	Figure	Domain	$k_S/k_L$	$3k_T/k_L$
0	6.4a,b	sp	$10^4$	0
1	6.4c,d	sp	1	0
2	6.4e,f	sp	$10^{-4}$	0
3	6.5a,b, 6.8	sp	$10^3$	0
4	6.8	sp	$10^3$	0.1
5	6.5c,d, 6.8	sp	$10^3$	0.2
6	6.8	sp	$10^3$	0.3
7	6.5e,f, 6.8	sp	$10^3$	0.4
8	6.8	sp	$10^3$	0.5
9	6.5g,h, 6.8, 6.6,6.7, 6.9	sp	$10^3$	0.36
10	6.6	cub	$10^3$	0.36

Table 6.1 Summary of all the parameters used for simulations of the model included in this work. The abbreviations *cub* and *sp* refer to the domain shapes *cubic array of spheres* and *hollow sphere* respectively. The parameters in row #9 are those used to generate the structure investigated further as a model for C–S–H.

These points were determined using the STEP method proposed by Edén [196].

## 6.4 Results

The sheet growth model was used to generate a range of different structures. The parameters used are summarised in Table 6.1.

### 6.4.1 Growth morphologies

In Figure 6.4, three-dimensional structures are shown which have been grown with different model parameters. The first two rows show cross sections through the structures. Those shown in the first row evolved to about 50 %, and the second row shows final structures which were unable to grow further. The last row provides three-dimensional visualisations of the fully evolved structures. Across the columns, the ratio between the primary growth parameters  $k_S/k_L$  is varied from  $10^{-4}$  to  $10^4$ . As previously discussed in Section 5, this affects the aspect ratio of the forming sheet crystal. When planar growth dominates layering ( $k_S \gg k_L$ ), the pore wall is covered by an open network of sheets, as seen in the cross section. The orientation of each sheet is set during the random placement of the initial seeds. Occasionally one can observe sheets growing around each other. As the structure evolves further, the large gaps between the initial sheets are filled in by aligned sheets. This picture changes considerably if growth and layering are balanced ( $k_S \approx k_L$ ). This is seen in

the second column of Figure 6.4. These crystals form a dense layer on the surface, whose thickness increases radially inwards. These crystals are also visible as individual, almost circular patches in the three-dimensional visualisation, in Figure 6.4f. The third column shows a situation where layering dominates sheet growth,  $k_L \gg k_S$ . Initially, thin stacks of sheets are formed. Some of these can be seen penetrating the cross section close to the centre of the cavity. It can be observed that strong anisotropy ( $k_S \neq k_L$ ) in the growth leads to two-staged space filling. An open structure is formed first, which densifies as the structure evolves. Such densification of C–S–H has been measured by NMR [40] and proposed previously by other authors [46, 47]. Note that two-staged space filling is a general feature of anisotropic growth due to mutual blocking of growing objects [180, 183, 183].

In Figure 6.5, the first three columns demonstrate the gradual effect of tilting is seen for structures grown with  $k_S/k_L = 1 \times 10^3$ . The last column shows a structure grown with an intermediate likelihood of tilted layering events, which was used to fit the NMR data, as explained below. The first row contains scenarios grown without tilt, whilst tilting is gradually introduced. The ratio  $3k_T/k_L$  gives the relative probability of a tilted to an aligned layering event at a given growth site. The resultant structures become gradually less ordered and dense. More defects and, hence, more gel pores are formed. Figure 6.5h and 6.4b are similar to the micrograph of Portland cement shown in Figure 6.7. Considering the scaling in the figure, the morphology shown has similarly-sized features. However, other micrographs such as Fig. 12 in [54] (reproduced in Figure 2.7d) show coarser features. It should be noted that preliminary results indicate that the feature size in the generated structures depends on the size of the confinement. Finally, the different morphologies seen in columns one and three of Figure 6.4 may be thought analogous to the two distinct morphologies seen in micrographs of cement pastes that are commonly called foil-like and fibrillar C–S–H [27]. However, it should be noted that the sheet orientation in fibrillar micrographs appears orthogonal to that in the simulation. The closing of larger pores as seen in the sequence 6.4a–b can mechanistically explain the densification of C–S–H proposed by Bishnoi and Scrivener from simulations using the modelling platform  $\mu ic$  [46]. The structure shown in Figure 6.5h is taken as the structure whose properties are compared for the rest of this chapter against experimental data for cement.

## 6.4.2 Model kinetics

Figure 6.6 shows the progress variable and growth rate as a function of time during the evolution of the structure shown in Figure 6.5h. The growth rate reaches a maximum after about 30 units of dimensionless time and a progress variable of about 0.35. It shows similarity to the experimentally observed heat flux for the hydration of tricalcium silicate, a major com-

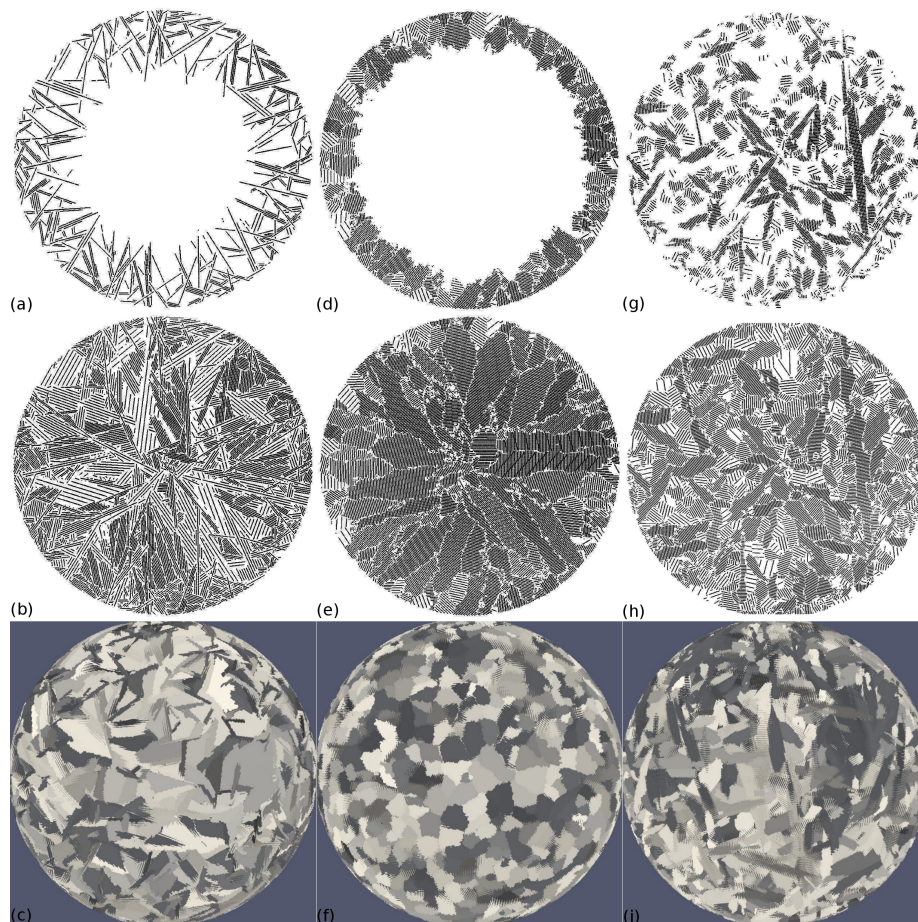


Fig. 6.4 Visualisations of structures obtained with different ratios between the planar growth and the layering growth rate. The first row shows cross sections through structures evolved about 50 %, and the second row through completely evolved structures, the last row contains 3D renderings. The parameters are shown in Table 6.1. In the first column, planar growth dominates layering (parameters #1), which leads to a diffuse and open growth front. In the second column, layering and planar growth occur with equal rates (parameters #2), which leads to a dense layer and a sharp growth front. In the third column, layering is much faster than planar growth (parameters #3). Columns of sheets are formed, which expand radially as the structure evolves further. Note that this is particularly evident in the 3D view.

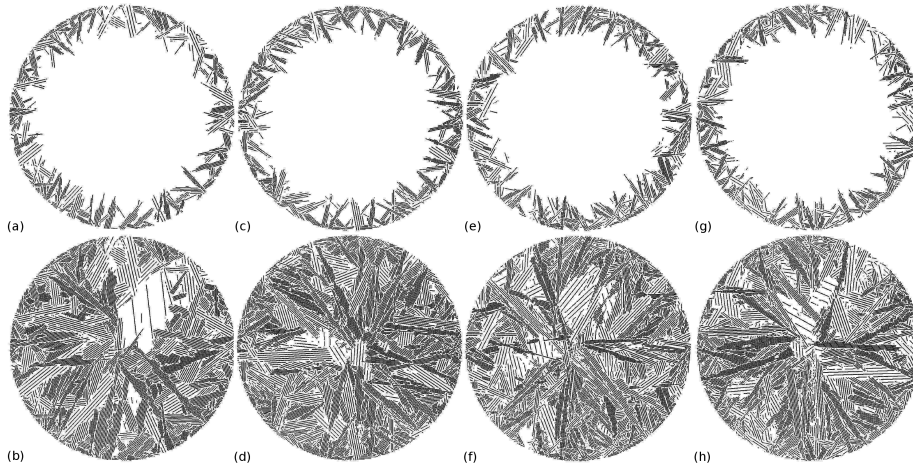


Fig. 6.5 Cross sections through structures grown with  $k_S/k_L = 10^3$  and varying tilt probability. The first row shows intermediate structures evolved to about 50%; the second row shows final structures. The structures in the first column, (a) and (b), are grown without tilt. The structures in the second column, (c) and (d), have a tilt probability of  $3k_T/k_L = 0.2$ . Structures (e) and (f), in the third column, of  $3k_T/k_L = 0.4$ . The fourth column, (g) and (h), contains structures with the pore space fitted to the NMR results. The tilt probability was  $3k_T/k_L = 0.36$ .

ponent of commercial cements, which is often used as a model system. An acceleration and deceleration period are observed as seen in hydrating cement paste [38]. This supports the feasibility of the suggested growth mechanism. However, careful comparison between the curves suggests a shorter deceleration period for the model compared to tricalcium silicate. The structure was grown in a sphere. One criticism of this geometry is that the growth rate is necessarily reduced as material always grows radially inwards in a concave space. In the real system, the outer product of C–S–H grows between packed, approximately spherical cement grains. Hence, at least in the early stages, it grows into a convexly-bound space. To exemplify the difference, Figure 6.6 also shows the growth rate for a structure, with the same parameters, grown in the interstitial space between a cubic array of spheres of radius 150 nm. Only a slight difference is observed for the kinetics curve. The implications of this result for different confinement geometries will be discussed below.

### 6.4.3 Model porosity

The gel or defect porosity in the model has already been defined in Section 6.3.1 and can also be measured by NMR in cement paste. For a given seed density and primary kinetic parameters, the composition of the pore space can be controlled using the tilt rate  $k_T$ . Figure 6.8 shows the volume fractions for the two types of pore spaces for the structures shown in

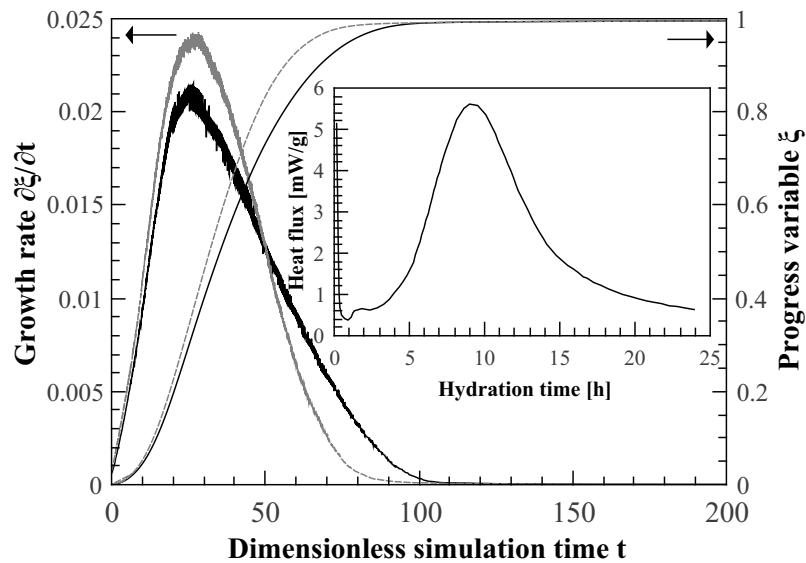


Fig. 6.6 Black lines: progress variable and growth rate ( for the structure shown in Fig. 6.5g. Grey lines: the same but for a structure grown between a cubic array of spheres. The inset (reproduced from [197]) shows experimental data for tricalcium silicate paste with a monomodal particle size.

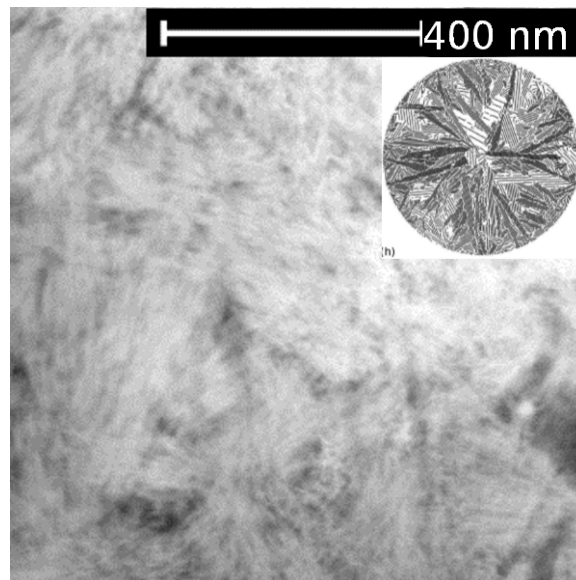


Fig. 6.7 TEM Micrograph of a white Portland cement after 28 days of hydration. The inset shows a correctly scaled cross section through the structure shown in Figure 6.5h. The micrograph was provided by J. Rossen, EPFL.

Figure 6.5h as a function of the tilt rate. The tilt probability for the favoured structure in this work,  $3k_T/k_L = 0.36$  was found by choosing a value which leads to the experimentally-derived ratio of defect volume fraction  $\varphi_d$  to interlayer volume fraction  $\varphi_{il}$ .

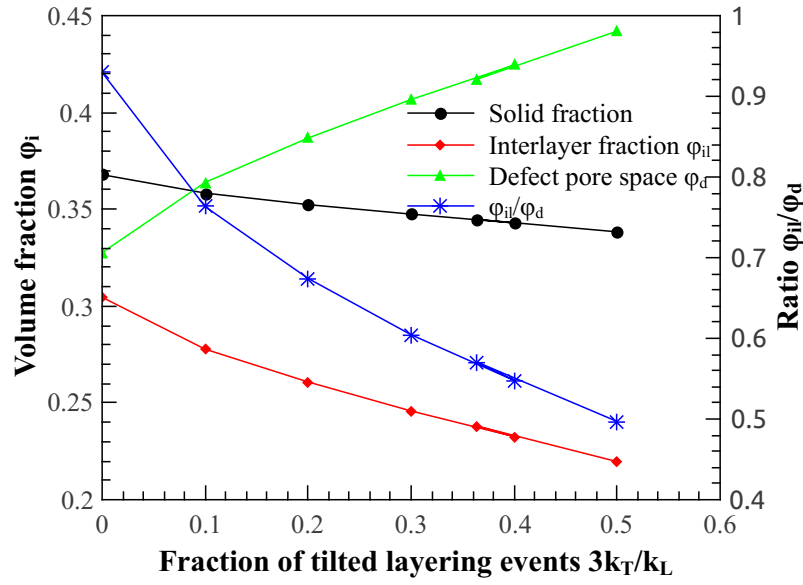


Fig. 6.8 Plot of the solid volume fraction  $\varphi_s$ , the interlayer volume fraction  $\varphi_{il}$  and the defect or gel volume fraction  $\varphi_d$  for the structures shown in Figure 6.5 as a function of the tilt probability  $3k_T/k_L$ . With an increasing tilt probability, additional defect pore space is created by reducing the interlayer and the defect volume fraction. The ratio between the two pore volume fractions is also plotted.

Table 6.2 compares the interlayer space volume fraction,  $\varphi_{il}$ , the defect or gel porosity  $\varphi_d$ , and the surface-to-volume ratios of the two pore types for each of the evolved structures in Figures 6.4 and 6.5h alongside values calculated from published pore sizes and water volume fractions in a white Portland cement measured by NMR [67]. To convert water mass fractions into volume fractions, a water density of  $1 \text{ g cm}^{-3}$  was assumed. Good agreement is seen between the surface-to-volume ratios of the two pore volumes in the tilted structure when compared to experiment. After fitting, both the ratio  $\varphi_d/\varphi_{il}$  and the absolute numbers themselves are in good agreement with the experiment. This demonstrates how the space distribution between defect (gel) and interlayer porosity can be tuned using the tilt-probability. A better agreement could have been obtained by tuning the thickness of the individual sheets, because the detailed porosities and the surface-to-volume ratios of the model depend on the sheet height  $h$  and the layer repeat distance  $d$ .

Table 6.2 Volume fractions ( $\varphi_i$ ) and surface-to-volume ( $S/V$ ) ratios of interlayer ( $il$ ) and defect ( $d$ ) pore spaces of the structures shown in Figure 6.4 and in 6.5 and of a white cement paste calculated from NMR experimental data.

	Fig. 6.4b	Fig. 6.4d	Fig. 6.4f	Fig. 6.5h	NMR [67]
$k_S/k_L$	$10^4$	1	$10^{-4}$	$10^3$	n/a
$\varphi_{il}$	0.27	0.42	0.40	0.24	0.27
$\varphi_d$	0.38	0.18	0.23	0.42	0.47
$S_{il}/V_{il}$ [nm <sup>-1</sup> ]	2.67	2.67	2.67	2.67	2.13
$S_d/V_d$ [nm <sup>-1</sup> ]	0.99	0.6	0.45	1.02	0.65

#### 6.4.4 Scattering

Cement morphologies have been investigated by small-angle scattering [30], the literature is reviewed to some extent in Chapter 2. The computational method used in this chapter has been described in Section 6.3.2. In this study, removal of domain size effects was not considered as discussed, for example, by Brisard and Levitz [61]. The surface of the confinement in the model is, in the real system, the interface between the outer product and the inner product C–S–H. Thus, the scattering arising from the domain boundary is not an artefact because its equivalent in the real system is certainly also seen by experimental small-angle scattering. Figure 6.9 shows the calculated scattering pattern for the tilted structure together with the pattern for the same structure, assuming no scattering contrast between the solid and interlayer space. The former is the scattering from the entire pore surface area whereas the latter is scattering from the gel pore surfaces only. Both curves show identical fringes for small  $q$ -vectors, which correspond to the form factor of the spherical confinement. This is demonstrated by the bottom curve in Figure 6.9, which is the analytical scattering pattern of a solid sphere of radius 150 nm [94]. The first simulation exhibits a distinct peak at  $4.467 \text{ nm}^{-1}$ , which is not seen in the second. This corresponds to the interlayer spacing  $d$ . For large  $q$ -vectors, both curves show a  $q^{-4}$  dependence which corresponds to the experimentally observed Porod regime. The simulated data is compared to experimental small-angle neutron scattering data for cement from Allen et al. (dashed) [9]. For large and intermediate  $q$ , and in the case of no contrast between solid and interlayer water, the curves are in general agreement. For small scattering vectors, the form factor of the confinement is seen in the simulation. In experiments, the spaces between cement particles are highly irregular in size and shape, so any confinement contribution would be smeared out. As can be seen in Figure 6.9, for  $q < 0.4 \text{ nm}^{-1}$ , the slope of the experimental curve is slightly less

steep than in the simulations. This is interpreted as the surface fractal property of the C–S–H nano-structure [9, 198]. The simulation domains are not sufficiently large to verify this.

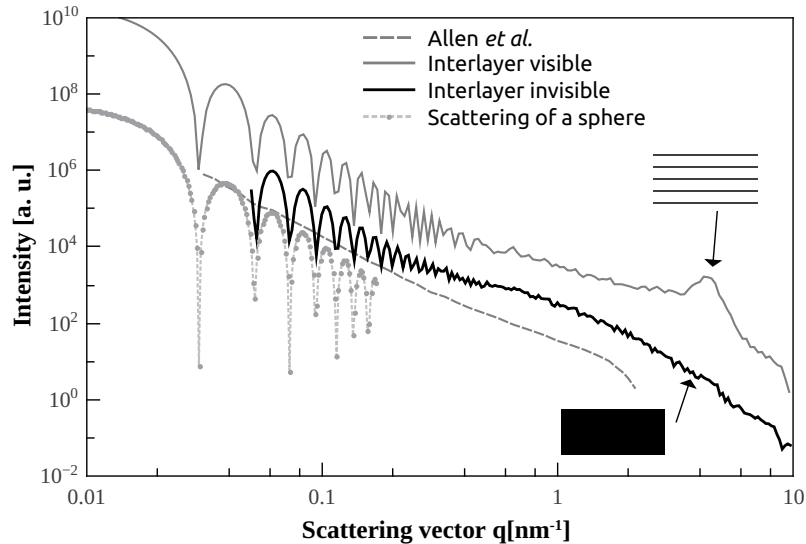


Fig. 6.9 Example scattering curves obtained for structure (h) in Figure 6.5 together with small-angle neutron scattering literature data taken from Allen *et al.* [9]. For clarity, each curve is offset from the next by an intensity factor of 10. From top: the experimental data and then simulated scattering of the tilted structure; the structure without solid-interlayer contrast and the spherical confinement.

### 6.4.5 Permeability

A standard single-relaxation time lattice Boltzmann permeability scheme has been implemented to calculate the permeability of the structure with and without flow through the interlayer space. The structure was grown within a cylinder with diameter and length of 50 nm and with 31 seeds placed on the surface, using the kinetic parameters of the structure shown in Figure 6.5h. The results yield a permeability of  $3.5 \times 10^{-20} \text{ m}^2$  with fluid flow enabled in all spaces and  $2.5 \times 10^{-20} \text{ m}^2$  with flow in the gel spaces only (i.e. no flow in the interlayer). These values suggest that flow through the interlayer is not as important as flow through the remaining pore space. Experimental results for the permeability of cement paste vary widely in the range  $10^{-18}$  to  $10^{-22} \text{ m}^2$ , depending on sample preparation and measurement method [100, 199]. The permeability of the C–S–H within the cement is thought to be lower and has been estimated as  $7 \times 10^{-23} \text{ m}^2$  [200], a value which is over 100 times less than the simulations here. This discrepancy may be due to the spaces at the edges of

sheets. In fully evolved structures, these spaces arise from the exclusion zone of neighbouring sheets and create connectivity of the gel porosity. The chemistry, and hence structure, surrounding sheet edges remains uncertain and such connectivity may not be present. Using the well-known Carman-Kozeny equation for a particle packing with a radius of 5 nm, as suggested for colloidal models [3, 9], and a gel porosity of 0.47 as measured by NMR, gives a permeability of  $5 \times 10^{-20} \text{ m}^2$  for a non-hierarchical colloidal model. Even if the packing density in the colloid model is assumed to be higher, the permeability of such packings remains far higher than the experimental values of C–S–H (see Chapter 4). This result indicates that, even if the new model cannot yet explain the low permeability of cement paste and C–S–H, it is equally as good as the colloidal model. Further exploration of the transport properties are needed.

## 6.5 Discussion of the model

In the previous sections it has been demonstrated that the new algorithm leads to structures whose porosity can be matched to NMR porosimetry data and whose morphology and scattering curves are in general agreement with experimental data. Comparison between the structures generated by the model and experimental C–S–H systems can be made only if the following simplifications are accepted: in all experimental systems, the cement grain size and shape are expected to be polydisperse, and the confinement size of *ca.* 150 nm will only cover the smaller end of the capillary pore space. Furthermore, the structures were grown with a seed density of almost  $6000 \mu\text{m}^{-2}$ . This is about 600 times larger than that suggested by Figure 3(a2) in Alizadeh et al. [52], and 300 times larger than counted by Bazzoni et al. on electron microscopy after 2 h [50]<sup>2</sup>. However, to the best of this author's knowledge, reliable quantitative data about the seed density on cement grains does not exist.

The influence of the initial seed density is twofold: fewer seeds lead to a reduced number of growth sites and, thus, to slower growth. More critically, without the tilt mechanism, each sheet gives rise to a crystalline layered structure. The long-range disorder in the structures modelled in this work is thus generated by the complex interplay of the sheets growing from different seeds. Microscopic evidence, e. g. by Gartner or Alizadeh [51, 52] suggests that open, expanding structures grow from relatively few nuclei. For the model as it is, the high number of seeds is necessary to induce sufficient disorder into the non-tilted systems. Ongoing work indicates that disorder can also be introduced by a tilt mechanism, either during layer formation, as presented here, or during the planar growth step. This can replace the randomness induced by the large number of seeds, so that only a few seeds would be

---

<sup>2</sup>The data of Bazzoni et al. was published after the work in this chapter had been completed.

required for anisotropic structures. This is currently the primary aim for the further development of the model. The second aspect concerns the seed density and requires refinement of the location of the defect or gel pore space. As shown in Table 6.2, the structures without tilt exhibit considerable non-interlayer pore space, located between stacks of sheets and caused by the exclusion zone between sheets. NMR indicates the formation of the gel pore space as the nano-structure develops [40], whilst the porosity located between stacks of sheets only closes as stacks expand.

The confinement shape (see Figure 6.6) as well as its size, affects the characteristic parameters, namely time of peak growth rate and the corresponding progress variable of the growth rate curve. The extension of the model to include a polydisperse pore space is currently being pursued. However, due to the space filling nature of the algorithm, properties such as the porosity do not depend on the domain shape, as long as the domain is considerably larger than the structural features. Whilst the kinetic curve outlines the applicability of the model to hydrating cement paste, its value must be limited to investigations of the growth order, such as proposed by Gartner [8, 22] because the model currently neither includes any reactant transport information nor represents the complex capillary pore space. The model presented in this work is intended to be as simple as possible because its parameters, such as the growth rates, are currently unknown. Thus, it was decided against considering further aspects such as introducing a preferred growth direction in the plane of the sheets, as could be expected due to the crystal structure of tobermorite and microscopic evidence. It is anticipated that the model will be appropriately extended as soon as such information, as the relative growth rates in tobermorite or C-S-H, becomes available from other techniques.

## 6.6 Conclusion

In this chapter, an algorithm is presented simulating the growth of amorphous sheet structures in confinements. It has been applied to the formation of C-S-H in hydrating cement paste. Both the evolution and morphology of the simulated structures correspond with a range of experimental observations. The emerging picture is qualitatively consistent. The results suggest that a systematic exploration of the parameter space of the model combined with further development of the branching sequence will lead to structures with properties that quantitatively match experimental systems. We anticipate that this development will allow progress to be made towards a better understanding of the nature and formation of cement's hydration products, a debate benefiting from quasi-continuous sheet models in three dimensions.

## **Note on publication**

The text in this chapter is based on the paper by Etzold et al. published in *Cement and Concrete Research* [168]. The simulations contained in this chapter are new; due to the developments made of the algorithm since the paper had been submitted.

## **Acknowledgements**

The author thanks John Rossen of EPFL, Switzerland, for providing the micrograph 6.7.



# Chapter 7

## Conclusions and future work

### 7.1 Conclusion

The key conclusions of this thesis can be summarised chapter-wise:

1. The cement community has a poor understanding of the meso-structure of the calcium-silicate-hydrates (C–S–H), such as that found in Portland cement. Modern authors tend to describe the meso-structure either as an aggregate of colloidal particles or as a sheet structure. Arguments can be found in support for either of the hypotheses (Chapter 2).
2. Simple particle packings were taken as a model structure for a colloidal aggregate. The transport properties of the packings were calculated and compared against data for mature cement paste, which is assumed to be controlled by the properties of C–S–H. The colloidal model was not able to explain the extraordinarily low transport properties of mature cement paste (Chapter 4).
3. A new Monte-Carlo algorithm to describe growing sheet structures was successfully developed. The abstract problem of a growing sheet structure was rationalised in a hierarchy of growth models which were characterised using the new algorithm. Some of the growth models are of interest for cement. The author anticipates that the algorithm is of general interest to study anisotropic growth problems as those that occur readily in material science or geology (Chapter 5).
4. The sheet growth model developed previously was used to grow C–S–H structures. It was shown how their properties could be compared against experimental data from literature. The properties of the model structures are in general agreement with observations made on hydrating cement paste (Chapter 6).

The key result of this thesis, from a cement perspective, is the application of the growth model towards C–S–H in cement. It was released for the first time to a wider audience in November 2013 and was positively received. In the subsequent discussions it emerged that the large number of seeds, from which growth originates, is probably unrealistic (see Chapter 2). A closer scrutiny of micrograph also shows that complex clusters of C–S–H emerge from isolated seeds on the surface of the cement grains (see also Chapter 2). The disorder in the first model was controlled by the number of initial seeds, from each of which a single sheet evolved.

## 7.2 Future work

In Chapter 5, it was shown that the potential refinement may exist already. It was shown that the combination of sheet growth with occasional bifurcation events can lead to complex and disordered structures, originating from a single nucleus. With this mechanism, structures may be developed which fit the experimental data better.

It turned out that simulating complex growing structures with the current program is very memory demanding, which may also limit the investigation of new structures. Since the proposed model is off-lattice, the methods of computational geometry may allow one to reduce the number of triangles per sheet by re-meshing the sheets [188], which should drastically increase the memory efficiency of the algorithm.

In the current version of the sheet growth code, a gap of the order of half the triangle side length remains when sheets collide. It would be desirable to control the size of these gaps, since they have a major effect on the properties of these resultant structures. This was attempted during the course of this thesis but not satisfactorily completed.

The idea of the off-lattice growth model has attracted the interest of other researchers, such as Holness et al., who are interested in the precipitation of bulky plagioclase crystals from Magma [201]. An important aspect of this work is to understand the interaction of the crystals and the effect of impingement between crystals on the average aspect ratio. The model presented here is ideal for this task. The simulations of fluid-flow conducted in this thesis always assumed macroscopic fluid behaviour, for example, that the Navier-Stokes equation with macroscopic velocities holds. It would be interesting to understand the effect of the pore surface on the fluid behaviour. Botan et al. [159] and Rotenberg et al. [158] show how molecular dynamics methods can be used to study the fluid behaviour and even hydrodynamics in nano-pores found in clays. Analogous studies could also be conducted on calcium-silicate-hydrate surfaces or clays to develop understanding about the fluid movement in these fine cement pores.

# Nomenclature

## Cement chemistry

$\alpha$  Degree of hydration

$\bar{S}$  Cement chemistry shorthand for sulphur trioxide

$Ca/Si$  Calcium-to-silicon atomic ratio.

$w/c$  Water-to-cement ratio by weight.

A Cement chemistry shorthand for aluminium oxide

C Cement chemist shorthand for calcium

F Cement chemistry shorthand for iron oxide

H Cement chemist shorthand for water

S Cement chemist shorthand for silicon dioxide

## Glossary

alite Abundant calcium silicate clinker phase. Main chemical composition is  $C_3S$

belite Second most important calcium silicate clinker phase. Chemical composition is  $C_2S$

BET Brunnauer-Emmet-Teller method to measure surfaces of porous materials.

Capillary pores Large pores found in cement paste in the range of micrometres.

CDE Convection diffusion equation.

CFD Computational fluid dynamics.

D-Drying D-drying refers to equilibrating the sample with the water vapour pressure at  $-79^\circ\text{C}$ , which is about  $6.7 \times 10^{-2}$  Pa [73].

- ESEM Electron scanning electron microscope
- Gel pores Small pores found within the calcium-silicate-hydrate formed during cement hydration. They are in the lower nanometre range.
- HD-C-S-H High density C-S-H in Jennings' model
- Interlayer space Water filled spaces between sheets of tobermorite/C-S-H. The water is likely to be part of the structure.
- ip Short for inner product. The inner product is the hydration product of cement forming within the cement grain.
- ITZ Interfacial transition zone. Region in concrete in the vicinity of aggregates
- LBE Lattice Boltzmann equation.
- LD-C-S-H Low density C-S-H in Jennings' model
- More Much more German expression for discontent
- NMR Nuclear magnetic resonance - in this thesis it usually refers to  $T_2$  NMR on protons.
- NSE Navier-Stokes equation.
- op Short for outer product. The outer product is the hydration product of cement forming within the capillary pore space.
- SANS Small-angle neutron scattering
- SAS Small-angle scattering
- SAXS Small-angle X-ray scattering
- SCM Supplementary cementitious materials.
- SEM Scanning electron microscopy
- TEM Transmission electron microscopy
- Kinetic Monte Carlo**
- $\bar{P}(\tau)$  Probability that no event occurs in the interval  $t, t + \tau$ .
- $\delta t$  Short time interval.

- $\sigma$      Something I am not sure about
- $\tau$      Point in time at which next process will occur.
- $f(\tau)$    Probability for any process to occur in the time interval  $(t + \tau, t + \tau + d\tau)$ .
- $f(\tau, i)$  Process probability density function (PPDF)
- $k_i$      Rate of process  $i$ .
- $N$      Number of possible processes in a system.
- $n_i$      Number of instances of a given process which can occur at a given time.
- $P_i(d\tau)$  Probability that an event  $i$  will occur in time interval  $d\tau$ .
- $R_i$      Variable name for a process.
- $t$      Time
- $X$      Uniformly distributed random number,  $X \in [0, 1)$ .

### **Transport property prediction**

- $\delta t$      Time step in a lattice Boltzmann algorithm.
- $\delta x$      Lattice spacing.
- $\delta$      Constrictivity of a porous medium.
- $\mathbf{c}_i$      Lattice velocity.
- $\mathbf{g}$      A body force acting on a fluid such as gravity.
- $\mathbf{j}_e$      Effective mass flux through a porous medium per unit area.
- $\mathbf{j}$      Mass flux of the diffusive species per unit area
- $\mathbf{n}$      Surface normal vector for the domain boundary.
- $\mathbf{q}$      Volume flux vector per unit area.
- $\mathbf{r}$      Position vector.
- $\mathbf{r}_w$      Position of boundary.
- $\mathbf{u}$      Fluid velocity.

- $\mathbf{u}_B$  Bulk fluid velocity.
- $\mu$  Dynamic viscosity.
- $\Omega(\mathbf{r}, t)$  Collision operator.
- $\omega_i$  Lattice weight for direction  $i$ .
- $\rho$  Density of the lattice gas.
- $\rho$  Fluid density.
- $\tau_c$  Tortuosity of a porous medium.
- $\varphi$  Solid volume fraction of a porous medium.
- $A$  Geometric constant given by Cubaud.
- $b_1, b_2, b_3$  Coefficients for generalised boundary condition.
- $c_e$  Effective concentration of a diffusing species in a porous medium.
- $c_f$  Fluid concentration close to a wall node.
- $c_s^2$  Lattice speed of sound.
- $c_{wi}$  Fictitious wall concentration for channel  $i$ .
- $D$  Diffusion coefficient of the lattice gas in the diffusion model.
- $D_0$  Bulk or self-diffusion coefficient.
- $D_1, D_2$  Diffusion coefficients in the two pipe segments of the problem used to verify the diffusion lattice Boltzmann code.
- $D_e$  Effective diffusion coefficient in a porous medium.
- $F$  Collision frequency.
- $f(\mathbf{v})$  Boundary homogenisation factor for the two pipe problem, defined in the paper of Berezhkovskii *et al.*.
- $f^+(\mathbf{r}_f, t)$  Velocity distribution streamed in the wall.
- $f_i(\mathbf{x}, t)$  Amplitude of scattered radiation in direction  $q$

- $f_i(\mathbf{x}, t)$  Probability to find a particle at position  $\mathbf{r}$  moving in direction  $\mathbf{c}_i$
- $f_i^{eq}(\mathbf{u}(\mathbf{r}), \rho(\mathbf{r}, t))$  Equilibrium particle velocity probability for direction  $i$ .
- $f_i^-$  Velocity distribution functions streamed into the simulation domain at a generalised boundary condition.
- $h$  Channel height for the channels used to verify the permeability scheme.
- $k$  Fluid permeability.
- $L_1, L_2$  Lengths of the pipe segments in the problem used to verify the diffusion lattice Boltzmann code.
- $N$  Number of velocities in space.
- $p$  Pressure.
- $R_1, R_2$  Radii in the two-pipe problem used to verify the diffusion lattice Boltzmann code.
- $T$  Average life time of tracer in the two-pipe problem.
- $V_1, V_2$  Volume of the pipe segments used to verify the diffusion lattice Boltzmann code.

### Sheet Growth

- $\alpha, \beta$  Proportionality constants.
- $\bar{G}_i^x$   $i$ th blocked event of type  $x$ .
- $\bar{l}_i$  Number of blocked events of type  $i$  which can occur.
- $\bar{L}_x$  List containing blocked events of type  $x$ .
- $\delta(t)$  Dirac symbol.
- $\gamma_b$  Bifurcation angle.
- $\gamma_T$  Tilt angle.
- $\hat{G}_i^x$   $i$ th allowed event of type  $x$ .
- $\hat{l}_i$  Number of allowed events of type  $i$  which can occur.
- $\hat{L}_x$  List containing allowed events of type  $x$ .

---

$\bar{\mathbf{r}}$	Average position vector.
$\mathbf{r}$	Position vector.
$\mathbf{u}_i, \mathbf{v}_i, \hat{\mathbf{n}}_i$	Vectors of the coordinate system of the $i$ th triangle.
$\mathbf{V}_i^j$	Position of the $j$ th vertex of the $i$ th triangle. The vertices are indexed clockwise.
$\varphi(t)$	Solid volume fraction.
$\varphi_d$	Volume fraction of gel pore space.
$\varphi_{il}$	Volume fraction of interlayer pore space.
$A$	Surface area of Eden cluster.
$A_{\Delta}$	Surface area of triangular segment.
$A_N$	Element prefactor.
$A_r$	Radial prefactor.
$C_2$	Proportionality constant for finding the characteristic time of impingement.
$D$	Dimensionality of a structure.
$d$	Layering distance.
$D_H$	Hausdorff dimension of a structure.
$d_{il}$	Height of the interlayer space.
$G_i^x$	$i$ th event of type $x$ .
$h$	Sheet height.
$J_{\mathbf{r}}$	Jacobian of the coordinate system of the triangle.
$k$	Kinetic constant in the Avrami model.
$k_B$	Bifurcation rate.
$k_L$	Layering rate.
$k_N$	Nucleation rate per unit volume.
$k_S$	Sheet growth rate.

---

$k_T$	Tilt rate.
$L$	Triangle side length.
$l_i$	Number of events of type $i$ which can occur.
$L_P$	Length of the perimeter of an Eden cluster.
$L_x$	List containing events of type $x$ .
$N$	Sites or elements in a cluster.
$n$	Growth exponent.
$n$	Growth exponent
$N(t, t')$	Number of triangular segments in a cluster formed at $t'$ .
$N_E$	Elements or sites in Eden cluster.
$n_r$	Radial growth exponent.
$N_S$	Number of initial nucleation sites in cavity.
$P_L$	Number of triangular facets on which layering and tilted layering can occur.
$P_P$	Number of perimeter sites of an Eden cluster where sheet growth and bifurcation can occur.
$r$	Radius of a cluster
$R_C$	Radius of the confinement.
$r_g$	Radius of gyration of a cluster.
$S$	Number of surface sites.
$S_E$	Perimeter of Eden cluster.
$t$	Time.
$t^*$	Characteristic time of impingement for space filling by growing sheets.
$T_i$	$i$ th Triangle.
$V(t, t')$	Volume of a cluster nucleated at $t'$ .

$x_i$  Progress variable.

### **Packing algorithm**

$\alpha, \beta$  Weight parameters for rotational and angular displacement.

$\bar{\delta}$  Average overlap of all spherocylinders.

$\Delta \mathbf{r}_i$  Change of particle position of particle  $i$  during an iteration.

$\delta_{ij}$  Overlap between two spherocylinder.

$\hat{\mathbf{q}}$  Quarternion.

$\mathbf{C}_{ij}$  Points of closest contact on the particle's backbone between two spherocylinders.

$\mathbf{D}_i$  Displacement vector during an iteration for spherocylinder  $i$ .

$\mathbf{D}_{ij}$  Displacement vector between two overlapping spherocylinders.

$\mathbf{M}_{ij}$  Rotational displacement vector during an iteration for spherocylinder  $i$ .

$\mathbf{M}_{ij}$  Rotational displacement between particles  $i, j$ .

$\mathbf{O}_i$  Orientation of spherocylinder  $i$

$\mathbf{r}_i$  Position of spherocylinder  $i$ .

$\theta_i$  Angular displacement of spherocylinder  $i$  during one iteration.

$\varphi$  Solid volume fraction in spherocylinder packing.

$d_{min}$  Minimal distance between two spherocylinders' backbones.

$L$  Length of a spherocylinder excluding the spherical cap.

$P_i s_i$  Symbol used for parameter equation for the backbone of spherocylinder  $i$ .

$q_1, q_2, q_3, q_4$  Components of quarternions.

$R$  Radius of a spherocylinder.

$R(\hat{\mathbf{q}})$  Rotation matrix derived from quarternions.

$s_i$  Parameter of parameter equation for spherocylinder  $i$ 's backbone.

$s_{cij}$  Critical parameter for the closest point on the backbone between two overlapping spherocylinders.

$w$  Aspect ratio of a spherocylinder, defined as  $w = L/(2R)$ .

### Scattering Curve Prediction

$\delta x$  Voxel size of a voxelised representation of a structure.

$\Gamma_{\rho_S}(\mathbf{r})$  Autocorrelation function of the scattering length density function.

$\lambda$  Wavelength of radiation.

$\mathbf{q}$  Scattering vector

$\mathbf{r}$  Position vector

$\rho_S(\mathbf{r})$  Scattering length density function.

$A(\mathbf{q})$  Amplitude of scattered radiation in direction  $q$

$A(\mathbf{q})$  Amplitude of scattered radiation.

$A_{disc}$  Fourier transform of a voxelised representation of a structure.

$I(\mathbf{q})$  Intensity of scattered radiation.

$I(\mathbf{r})$  Indicator function.

$I(q)$  Spherically averaged intensity.

$q_i$  Component of the scattering vector  $\mathbf{q}$ .

$q_{max}$  Maximum accessible scattering vector in the Schmidt-Rohr method.

$q_{min}$  Minimal accessible scattering vector in the Schmidt-Rohr method.



# References

- [1] K. L. Scrivener and R. J. Kirkpatrick. Innovation in use and research on cementitious material. *Cem. Conc. Res.*, 38(2):128–136, 2008.
- [2] T. C. Powers. Structure and physical properties of hardened Portland cement paste. *J. Am. Ceram. Soc.*, 41(1):1–6, 1958.
- [3] H. M. Jennings. A model for the microstructure of calcium silicate hydrate in cement paste. *Cem. Conc. Res.*, 30(1):101–116, 2000.
- [4] H. M. Jennings. Refinements to colloid model of C-S-H in cement: CM-II. *Cem. Conc. Res.*, 38(3):275–289, 2008.
- [5] R. F. Feldman and P. J. Sereda. New model for hydrated Portland cement and its practical implications. *Eng. J. – Canada*, 53(8/9):53–59, 1970.
- [6] P. J. McDonald, V. Rodin, and A. Valori. Characterisation of intra- and inter-C-S-H gel pore water in white cement based on an analysis of NMR signal amplitudes as a function of water content. *Cem. Conc. Res.*, 40(12):1656–1663, 2010.
- [7] K. L. Scrivener. Hydration of cementitious materials, present and future. *Cem. Conc. Res.*, 41:651–665, 2011.
- [8] E. M. Gartner. A proposed mechanism for the growth of C–S–H during the hydration of tricalcium silicate. *Cem. Conc. Res.*, 27:665–672, 1997.
- [9] A. J. Allen, J. J. Thomas, and H. M. Jennings. Composition and density of nanoscale calcium-silicate-hydrate in cement. *Nature Mater.*, 6:311–316, 2007.
- [10] E. Gartner. Industrially interesting approaches to “low-CO<sub>2</sub>” cements. *Cem. Conc. Res.*, 34(9):1489 – 1498, 2004.
- [11] M. Schneider, M. Romer, M. Tschudin, and H. Bolio. Sustainable cement production – present and future. *Cem. Conc. Res.*, 41:642–650, 2011.
- [12] Eine Milliarde für 78 Autobahnbrücken. *Frankfurter Allgemeine Zeitung*, 20.09.2014.
- [13] Federal Government of Germany. Bundeshaushalt 2013, 2013.
- [14] American Society of Civil Engineers. 2013 Report card for america’s infrastructure, 2013. URL <http://www.infrastructurereportcard.org/a/documents/2013-Report-Card.pdf>.

- [15] *An Economic Analysis of Transportation Infrastructure Investment*, 2014. The White House. URL [http://www.whitehouse.gov/sites/default/files/docs/economic\\_analysis\\_of\\_transportation\\_investments.pdf](http://www.whitehouse.gov/sites/default/files/docs/economic_analysis_of_transportation_investments.pdf).
- [16] C. Hein. Der Kontinent hat ein Infrastrukturproblem. *Frankfurter Allgemeine Zeitung*, 03.06.2014.
- [17] K. L. Scrivener, A. K. Crumbie, and P. Laugesen. The interfacial transition zone (ITZ) between cement paste and aggregate in concrete. *Interface Sci.*, 12(4):411–421, 2004.
- [18] A. J. Allen, R. C. Oberthur, D. Pearson, P. Schofield, and C. R. W. Wilding. Development of the fine porosity and gel structure of hydrating cement systems. *Philos. Mag. B*, 56(3):263–288, 1987.
- [19] O. Bernard, F.-J. Ulm, and E. Lemarchand. A multiscale micromechanics-hydration model for the early-age elastic properties of cement-based materials. *Cem. Conc. Res.*, 33(9):1293 – 1309, 2003.
- [20] J.S. Damtoft, J. Lukasik, D. Herfort, D. Sorrentino, and E.M. Gartner. Sustainable development and climate change initiatives. *Cem. Conc. Res.*, 38(2):115 – 127, 2008.
- [21] L. Basheer, J. Kropp, and D. J. Cleland. Assessment of the durability of concrete from its permeation properties: a review. *Construction and Building Materials*, 15 (2–3):93–103, 2001.
- [22] E. M. Gartner and J. M. Gaidis. *Hydration Mechanisms, I*, chapter 4, pages 95–126. The American Ceramic Society, Inc, 1989.
- [23] M. L. Mansfield and L. I. Klushin. A generalized Eden model of polymer crystallization. *POLYMER*, 35(14):2937–2943, 1994.
- [24] F. W. Locher. *Zement - Grundlagen der Herstellung und Verwendung*. Verlag Bau und Technik, 2000.
- [25] Verein Deutscher Zementwerke e. V., editor. *Zement-Taschenbuch 2002*. Verlag Bau+Technik GmbH, 2002.
- [26] Stark J. and B. Wicht. *Zement und Kalk: Der Baustoff als Werkstoff (BauPraxis)*. Birkenhäuser Verlag, kindle edition, 1999.
- [27] I. G. Richardson. Tobermorite/jennite- and tobermorite/calcium hydroxide-based models for the structure of C-S-H: applicability to hardened pastes of tricalcium silicate, [beta]-dicalcium silicate, Portland cement, and blends of Portland cement with blast-furnace slag, metakaolin, or silica fume. *Cem. Conc. Res.*, 34(9):1733–1777, 2004.
- [28] E. Bonaccorsi, S. Merlino, and A. R. Kampf. The crystal structure of tobermorite 14 Å (plombierite), a C–S–H phase. *J. Am. Ceram. Soc.*, 88(3):505–512, 2005.
- [29] K. L. Scrivener. Hydration and microstructure. Lecture during 1. TRANSCEND training course, February 2011.

- [30] A. J. Allen and J. J. Thomas. Analysis of C–S–H gel and cement paste by small-angle neutron scattering. *Cem. Conc. Res.*, 37:319–324, 2007.
- [31] I.G. Richardson and G.W. Groves. Models for the composition and structure of calcium silicate hydrate (C–S–H) gel in hardened tricalcium silicate pastes. *Cem. Conc. Res.*, 22(6):1001–1010, 1992.
- [32] I.G. Richardson and G.W. Groves. The incorporation of minor and trace elements into calcium silicate hydrate (C–S–H) gel in hardened cement pastes. *Cem. Conc. Res.*, 23(1):131–138, 1993.
- [33] H. Manzano, E. Masoero, I. Lopez-Arbeloa, and H. M. Jennings. Shear deformations in calcium silicate hydrates. *Soft Matter*, 9(30):7333–7341, 2013.
- [34] R. J. M. Pellenq, A. Kushima, R. Shahsavari, K. J Van Vliet, M. J Buehler, S. Yip, and F. J Ulm. A realistic molecular model of cement hydrates. *P. Natl. Acad. Sci. U.S.A.*, 2009.
- [35] Ian G. Richardson. The importance of proper crystal-chemical and geometrical reasoning demonstrated using layered single and double hydroxides. *Acta Crystallogr. Sect. B-Struct. Sci.*, 69(2):150–162, Apr 2013.
- [36] A. Gmira, M. Zabat, R. Pellenq, and H. Van Damme. Microscopic physical basis of the poromechanical behavior of cement-based materials. *Mat. Struct.*, 37:3–14, 2004.
- [37] E. Gartner, J. F. Young, D. A. Damidot, and I. Jawed. *Structure and Performance of Cements*, chapter Structure and Performance of Cements, pages 57–113. Spon Press - Taylor & Francis Group, 2002.
- [38] J. W. Bullard, H. M. Jennings, R. A. Livingston, A. Nonat, G. W. Scherer, J. S. Schweitzer, K. L. Scrivener, and J. J. Thomas. Mechanisms of cement hydration. *Cem. Conc. Res.*, 41(12):1208 – 1223, 2011.
- [39] K. L. Scrivener. *The Microstructure of Concrete*, chapter 5, pages 127–161. The American Ceramic Society, Inc, 1989.
- [40] A. C. A. Muller, K. L. Scrivener, A. M. Gajewicz, and P. J. McDonald. Densification of C–S–H measured by  $^1\text{H}$ -NMR relaxometry. *J. Phys. Chem. C*, 117(1):403–412, 2013.
- [41] S. Garrault and A. Nonat. Hydrated layer formation on tricalcium and dicalcium silicate surfaces: Experimental study and numerical simulations. *Langmuir*, 17:8131–8138, 2001.
- [42] S. Garrault, E. Finot, E. Lesniewska, and A. Nonat. Study of C–S–H growth on  $\text{C}_3\text{S}$  surface during its early hydration. *Mat. Struct.*, 38:435–442, 2005.
- [43] S. Garrault, T. Behr, and A. Nonat. Formation of the C–S–H layer during early hydration of tricalcium silicate grains with different sizes. *J. Phys. Chem. B*, 110: 270–275, 2006.

- [44] S. Garrault, N. Luc, and A. Nonat. Tricalcium silicate hydration modeling and numerical simulations. In *Conmod*, 2010.
- [45] J. S. Dolado and K. van Breugel. Recent advances in modeling for cementitious materials. *Cem. Conc. Res.*, 41(7):711–726, 2011.
- [46] S. Bishnoi and K. Scrivener. Studying nucleation and growth kinetics of alite hydration using  $\mu$ c. *Cem. Conc. Res.*, 39:849–860, 2009.
- [47] G. W. Scherer, J. Zhang, and J. J. Thomas. Nucleation and growth models for hydration of cement. *Cem. Conc. Res.*, 42(7):982–993, 2012.
- [48] G. W. Scherer. Models of confined growth. *Cem. Conc. Res.*, 42(9):1252 – 1260, 2012.
- [49] P. C. Fonseca and H. M. Jennings. The effect of drying on early-age morphology of C–S–H as observed in environmental SEM. *Cem. Conc. Res.*, 40:1673–1680, 2010.
- [50] A. Bazzoni, S. Ma, Q. Wang, X. Shen, M. Cantoni, and K. L. Scrivener. The effect of magnesium and zinc ions on the hydration kinetics of  $C_3S$ . *J. Am. Ceram. Soc.*, pages 1–10, 2014.
- [51] E. M. Gartner, K.E Kurtis, and P. J. M. Monteiro. Proposed mechanism of C-S-H growth tested by soft X-ray microscopy. *Cem. Conc. Res.*, 30(5):817–822, 2000.
- [52] Rouhollah Alizadeh, Laila Raki, Jon M. Makar, James J. Beaudoin, and Igor Moudrakovski. Hydration of tricalcium silicate in the presence of synthetic calcium-silicate-hydrate. *J. Mater. Chem.*, 19:7937–7946, 2009.
- [53] F. Bellmann, T. Sowoidnich, H.-M. Ludwig, and D. Damidot. Analysis of the surface of tricalcium silicate during the induction period by X-ray photoelectron spectroscopy. *Cem. Conc. Res.*, 42:1189–1198, 2012.
- [54] I. G. Richardson. The nature of the hydration products in hardened cement pastes. *Cem. Concr. Compos.*, 22(2):97–113, 2000.
- [55] C Rößler, J. Stark, F. Steiniger, and W. Tichelaar. Limited-dose electron microscopy reveals the crystallinity of fibrous C–S–H phases. *J. Am. Ceram. Soc.*, 89:627–632, 2006.
- [56] J. E. Pearson. Complex patterns in simple systems. *Science*, 261:189–192, 1993.
- [57] J.J Thomas, H.M Jennings, and A.J Allen. The surface area of cement paste as measured by neutron scattering: evidence for two C–S–H morphologies. *Cem. Conc. Res.*, 28(6):897–905, 1998.
- [58] A. J. Allen and R. A. Livingston. Relationship between differences in silica fume additives and fine-scale microstructural evolution in cement based materials. *Adv. Cem. Based Mater.*, 8(3–4):118–131, 1998.
- [59] J. J. Thomas, Allen. A. J., and H. M. Jennings. Structural changes to the calcium-silicatehydrate gel phase of hydrated cement with age, drying, and resaturation. *J. Am. Ceram. Soc.*, 91:3362–3369, 2008.

- [60] W.-S. Chian, E. Fratini, P. Baglioni, D. Liu, and S.-H. Chen. Microstructure determination of calcium-silicate-hydrate globules by small-angle neutron scattering. *J. Phys. Chem. C*, 116:5055–5061, 2012.
- [61] S. Brisard and P. Levitz. Small-angle scattering of dense, polydisperse granular porous media: Computation free of size effects. *Phys. Rev. E*, 87:013305, 2013.
- [62] P. S. Dodds and D. A. Weitz. Packing-limited growth. *Phys. Rev. E*, 65:056108, 65.
- [63] K. R. Brownstein and C. E. Tarr. Importance of classical diffusion in NMR studies of water in biological cells. *Phys. Rev. A*, 19(6):2446–2453, 1979.
- [64] D. Bytchenkoff and S. Rodts. Structure of the two-dimensional relaxation spectra seen within the eigenmode perturbation theory and the two-site exchange model. *J. Mag. Reson.*, 208:4–19, 2011.
- [65] D. A. Faux, P. J. McDonald, N. C. Howlett, J. S. Bhatt, and S. V. Churakov. Nuclear magnetic resonance relaxometry of water in two and quasi-two dimensions. *Phys. Rev. E*, 87:062309–1–18, 2013.
- [66] A. Valori, P.J. McDonald, and K.L. Scrivener. The morphology of C–S–H: Lessons from  $^1\text{H}$  nuclear magnetic resonance relaxometry. *Cem. Conc. Res.*, 49(0):65–81, 2013.
- [67] A.C.A. Muller, K.L. Scrivener, A.M. Gajewicz, and P. J. McDonald. Use of bench-top NMR to measure the density, composition and desorption isotherm of C—S—H in cement paste. *Micropor. Mesopor. Mat.*, 178(0):99–103, 2013.
- [68] L. Monteilhet, J.-P. Korb, J. Mitchell, and P. J. McDonald. Observation of exchange of micropore water in cement pastes by two-dimensional  $t_2$ - $t_2$  nuclear magnetic resonance relaxometry. *Phys. Rev. E*, 74(6):061404, 2006.
- [69] H. le Chatelier. Crystalloids against colloids in the theory of cements. *Trans. Faraday Soc.*, 14:8–11, 1919.
- [70] R. F. Feldman. Density and porosity of hydrated Portland cement. *Cement Technology*, 3(1):5–1, 1972.
- [71] M. Daimon, S. A. Abo-El-Enein, G. Rosara, S. Goto, and R. Kondo. Pore structure of calcium silicate hydrate in hydrated tricalcium silicate. *J. Am. Ceram. Soc.*, 60(3-4):110–114, 1977.
- [72] F. H. Wittmann. Surface tension shrinkage and strength of hardened cement paste. *Mater. Struct.*, 1:547–552, 1968.
- [73] H. J. Jennings and J. Thomas, 14.10.2014. URL <http://iti.northwestern.edu/cement/index.html>.
- [74] R. F. Feldman and P. J. Sereda. A model for hydrated Portland cement paste as deduced from sorption-length changes and mechanical properties. *Mater. Struct.*, 1(1):509–520, 1968.

- [75] H. M. Jennings and P. D. Tennis. Model for the developing microstructure in Portland cement pastes. *J. Am. Ceram. Soc.*, 77(12):3161–3172, 1994.
- [76] P. D. Tennis and H. M. Jennings. A model for two types of calcium silicate hydrate in the microstructure of Portland cement pastes. *Cem. Conc. Res.*, 30(6):855–863, 2000.
- [77] S. Torquato and F. H. Stillinger. Jammed hard-particle packings: From Kepler to Bernal and beyond. *Rev. Mod. Phys.*, 82:2633–2672, 2010.
- [78] H.M. Jennings. Colloid model of C–S–H and implications to the problem of creep and shrinkage. *Mat. Stuct.*, 37(1):59–70, 2004.
- [79] H. M. Jennings, J. J. Thomas, J. S. Gevrenov, G. Constantinides, and F.-J. Ulm. A multi-technique investigation of the nanoporosity of cement paste. *Cem. Conc. Res.*, 37(3):329 – 336, 2007.
- [80] M. Vandamme, F.-J. Ulm, and P. Fonollosa. Nanogranular packing of C–S–H at substoichiometric conditions. *Cem. Conc. Res.*, 40(1):14 – 26, 2010.
- [81] E. Masoero, E. Del Gado, R. J.-M. Pellenq, F.-J. Ulm, and S. Yip. Nanostructure and nanomechanics of cement: Polydisperse colloidal packing. *Phys. Rev. Lett.*, 109:155503, 2012.
- [82] K. Ioannidou, R. J.-M. Pellenq, and E. Del Gado. Controlling local packing and growth in calcium-silicate-hydrate gels. *Soft Matter*, 10:1121–1133, 2014.
- [83] M. P. Allen and D. J. Tildesley. *Computer Simulation of Liquids*. Oxford Sciences Publications, 1989.
- [84] K. Binder. Applications of Monte Carlo methods to statistical physics. *Rep. Prog. Phys.*, 60:487–559, 1997.
- [85] D. Frenkel and B. Smit. *Understanding Molecular Simulation: From Algorithms to Applications*. Academic Press Inc, 2nd revised edition, 2001.
- [86] W. M. Young and Elcock. Monte Carlo studies of vacancy migration in binary ordered alloys: I. *Proc. Phys. Soc.*, 89:735–746, 1966.
- [87] A. B. Bortz, M. H. Kalos, and J. L. Lebowitz. A new algorithm for Monte Carlo simulation of ising spin systems. *J. Comput. Phys.*, 17:10–18, 1975.
- [88] B. Meng and W. H. Weinberg. Monte Carlo simulations of temperature programmed desorption spectra. *J. Chem. Phys.*, 100:5280–5289, 1994.
- [89] B. Meng and W. H. Weinberg. Dynamical Monte Carlo studies of molecular beam epitaxial growth models: interfacial scaling and morphology. *Surface Science*, 364:151–163, 1996.
- [90] D. J. Srolovitz, G. S. Grest, and M. P. Anderson. Computer simulation of recrystallization—I. homogeneous nucleation and growth. *Acta Metall.*, 34(9):1933–1845, 1986.

- [91] D. T. Gillespie. A general method for numerically simulating the stochastic time evolution of coupled chemical reactions. *J. Comp. Phys.*, 22:403–434, 1976.
- [92] A. Chatterjee and D. G. Vlachos. An overview of spatial microscopic and accelerated kinetic Monte Carlo methods. *J. Computer-Aided Mater. Des.*, 14:253–308, 2007.
- [93] A. Voter. Introduction to the kinetic Monte Carlo method. In *Radiation Effects in Solids*. Springer, NATO Publishing Unit, 2005.
- [94] R.-J. Roe. *Methods of X-ray and Neutron Scattering in Polymer Science (Topics in Polymer Science)*. OUP USA, 2000.
- [95] S. Torquato. *Random heterogeneous materials*, volume 16. Springer, 2nd printing edition, 2006.
- [96] P. Debye and A. M. Bueche. Scattering by an inhomogeneous solid. *Journal of Applied Physics*, 20(6):518–525, 1949.
- [97] K. Schmidt-Rohr. Simulation of small-angle scattering curves by numerical Fourier transformation. *J. Appl. Crystallogr.*, 40(1):16–25, 2007.
- [98] R. B. Bird, W. E. Stewart, and E. N. Lightfoot. *Transport phenomena*. Wiley, 2nd edition, 2002.
- [99] J. van Brakel and P.M. Heertjes. Analysis of diffusion in macroporous media in terms of a porosity, a tortuosity and a constrictivity factor. *International Journal of Heat and Mass Transfer*, 17(9):1093–1103, 1974.
- [100] W. Vichit-Vadakan and G. W. Scherer. Measuring permeability of rigid materials by a beam-bending method: III, cement paste. *J. Am. Ceram. Soc.*, 85(6):1537–1544, 2002. ISSN 1551-2916.
- [101] G. Karniadakis, A. Beskok, and N. Aluru. *Microflows and Nanoflows*. Springer Science + Business Media, New York, 2005.
- [102] D. A. Wolf-Gladrow. *Lattice-Gas Cellular Automata and Lattice Boltzmann Models: An Introduction*. Springer, 2000.
- [103] S. Succi. *The Lattice Boltzmann Equation*. Numerical Mathematics and Scientific Computation. Oxford University Press, 2001.
- [104] D. Raabe. Overview of the lattice Boltzmann method for nano- and microscale fluid dynamics in materials science and engineering. *Modelling Simul. Mater. Sci. Eng.*, 12:R13–R46, 2004.
- [105] F. M. Sani. *Aspects of LBGK Development: Simulations of Hydrodynamics and Mass Transfer*. PhD thesis, University of Cambridge, April 2002.
- [106] M. A. A. Spaid and F. R. Phelan. Lattice Boltzmann methods for modeling microscale flow in fibrous porous media. *Phys. Fluids*, 9:2468–2474, 1997.
- [107] W. J. Bosl, J. Dvorkin, and A. Nur. A study of porosity and permeability using a lattice Boltzmann simulation. *Geophys. Res. Lett.*, 25:1475–1479, 1998.

- [108] R. S. Maier, D. M. Kroll, Y. E. Kutsovsky, H. T. Davis, and R. S. Bernard. Simulation of flow through bead packs using the lattice Boltzmann method. *Phys. Fluids.*, 10(1): 60–74, 1998.
- [109] D. S. Clague, B. D. Kandhai, R. Zhang, and P. M. A. Slood. Hydraulic permeability of (un)bounded fibrous media using the lattice Boltzmann method. *Phys. Rev. E*, 61: 616–625, 2000.
- [110] Z. Guo, C. Zheng, and B. Shi. Discrete lattice effects on the forcing term in the lattice Boltzmann method. *Phys. Rev. E*, 65:046308, 2002.
- [111] Q. Kang, D. Zhang, S. Chen, and X. He. Lattice Boltzmann simulation of chemical dissolution in porous media. *Phys. Rev. E*, 65:036318–1–8, 2002.
- [112] S.P. Sullivan, F.M. Sani, M.L. Johns, and L.F. Gladden. Simulation of packed bed reactors using lattice Boltzmann methods. *Chemical Engineering Science*, 60(12): 3405–3418, 2005.
- [113] A. Narvaez and J. Harting. Evaluation of pressure boundary conditions for permeability calculations using the lattice-Boltzmann method. *Adv. Appl. Math. Mech.*, 2: 685–700, 2010.
- [114] Y. H. Qian and S. A. Orszag. Lattice BGK models for the Navier-Stokes equation: Nonlinear deviation in compressible regimes. *Europhys. Lett.*, 21(3):255, 1993.
- [115] T. Zhang, B. Shi, Z. Guo, Z. Chai, and J. Lu. General bounce-back scheme for concentration boundary condition in the lattice-Boltzmann method. *Phys. Rev. E*, 85: 016701, 2012.
- [116] M. C. Sukop and D. T. Thorne. *Lattice Boltzmann Modeling. An Introduction for Geoscientists and Engineers*. Springer Verlag Berlin Heidelberg, 2010.
- [117] Q. Zou and X. He. On pressure and velocity boundary conditions for the lattice Boltzmann BGK model. *Phys. Fluids.*, 9(6):1591–1598, 1997.
- [118] M. Hecht and J. Harting. Implementation of on-site velocity boundary conditions for D3Q19 lattice Boltzmann simulations. *J. Stat. Mech.-Theory. E*, (01):P01018, 2010.
- [119] Q. Kang, P. C. Lichtner, and D. R. Janecky. Lattice Boltzmann method for reacting flows in porous media. *Advances in Applied Mathematics and Mechanics*, 2(5):545–563, 2010.
- [120] E. G. Flekkoy. Lattice Bhatnagar-Gross-Krook models for miscible fluids. *Phys. Rev. E*, 47(6), 1992.
- [121] S. Ponce Dawson, S. Chen, and G. D. Doolen. Lattice Boltzmann computations for reaction-diffusion equations. *J. Chem. Phys.*, 98(2):1514–1523, 1993.
- [122] J. Alvarez-Ramírez, S. Nieves-Mendoza, and J. González-Trejo. Calculation of the effective diffusivity of heterogeneous media using the lattice-Boltzmann method. *Phys. Rev. E*, 53:2298–2303, 1996.

- [123] Y. Xuan, K. Zhao, and Q. Li. Investigation on mass diffusion process in porous media based on lattice Boltzmann method. *Heat Mass Transfer*, 46:1039–1051, 2010.
- [124] G. Wellein, T. Zeiser, G. Hager, and S. Donath. On the single processor performance of simple lattice Boltzmann kernels. *Comput. Fluids*, 35(8–9):910 – 919, 2006.
- [125] T. Zeiser. *Simulation und Analyse von durchströmten Kugelschüttungen in engen Rohren unter Verwendung von Hochleistungsrechnern*. PhD thesis, Universität Erlangen-Nürnberg, 2008.
- [126] T. Zeiser. Efficient implementation of lattice Boltzmann flow solvers. In *ICMMES 2009 Tutorial*, <http://www.konwih.r.uni-erlangen.de/projekte/workshop-lattice-Boltzmann-methods/>, 2009.
- [127] T. Cubaud and C.-M. Ho. Transport of bubbles in square microchannels. *Phys. Fluids.*, 16(12):4575–4585, 2004.
- [128] M. Zalzale and P.J. McDonald. Lattice Boltzmann simulations of the permeability and capillary adsorption of cement model microstructures. *Cem. Conc. Res.*, 42(12): 1601 – 1610, 2012.
- [129] R. E. Larson and J. J. L. Higdon. A periodic grain consolidation model of porous media. *Phys. Fluids. A*, 1(1):38–46, 1989.
- [130] A. Sengupta, P. S. Hammond, D. Frenkel, and E. S. Boek. Error analysis and correction for lattice Boltzmann simulated flow conductance in capillaries of different shapes and alignments. *J. Comp. Phys.*, 231(6):2634 – 2640, 2012.
- [131] A. M. Berezhkovskii, A. V. Barzykin, and V. Y. Zitserman. One-dimensional description of diffusion in a tube of abruptly changing diameter: Boundary homogenization based approach. *J. Chem. Phys.*, 131(22):224110, 2009.
- [132] S. V. Churakov and T. Gimmi. Up-scaling of molecular diffusion coefficients in clays: A two-step approach. *J. Phys.Chem. C*, 115:6703–6714, 2011.
- [133] M. Zalzale, P. J. McDonald, and K. L. Scrivener. A 3D lattice Boltzmann effective media study: understanding the role of C–S–H and water saturation on the permeability of cement paste. *Model. Simul. Mater. Sci. Eng.*, 21(8):085016, 2013.
- [134] J. S. Dolado, M. Griebel, and J. Hamaekers. The nano-branched structure of cementitious calcium-silicate-hydrate gel. *J.Mater.Chem.*, 21:4445–4449, 2011.
- [135] R. Mills. Self-diffusion in normal and heavy water in the range 1-45.deg. *The Journal of Physical Chemistry*, 77(5):685–688, 1973.
- [136] R. Alizadeh, J. J. Beaudoin, and L. Raki. C–S–H(I) – a nanostructural model for the removal of water from hydrated cement paste? *J. Am. Ceram. Soc.*, 90:670–672, 2007.
- [137] E. Tajuelo Rodriguez, I. G. Richardson, L. Black, A. Nonat, J. Skibsted, and E. Boehm-Courjault. Chemical structure and morphology of C–S–H synthesized by silica-lime reaction and by the controlled hydration of C<sub>3</sub>S. In *Proceedings of 34<sup>th</sup> Cement and Concrete Science Conference*, number 166, 2014.

- [138] M. Sahimi. Flow phenomena in rocks: from continuum models to fractals, percolation, cellular automata, and simulated annealing. *Rev. Mod. Phys.*, 65:1393–1534, 1993.
- [139] D. Stauffer and A. Aharony. *Introduction to PERCOLATION THEORY*. CRC Press, revised second edition, 1994.
- [140] Kertész, J. Percolation of holes between overlapping spheres : Monte Carlo calculation of the critical volume fraction. *J. Physique Lett.*, 42(17):393–395, 1981.
- [141] P. Halamickova, R. J. Detwiler, D. P. Betnz, and E. J. Garboczi. Water permeability and chloride ion diffusion in Portland cement mortars: Relationship to sand content and critical pore diameter. *Cem. Conc. Res.*, 25(4):790–802, 1995.
- [142] A. S. El-Dieb and R. D. Hooton. A high pressure triaxial cell with improved measurement sensitivity for saturated water permeability of high performance concrete. *Cem. Conc. Res.*, 24(5):854–862, 1994.
- [143] B. K. Nyame and J. M. Illston. Relationships between permeability and pore structure of hardened cement paste. *Mag. Conc. Res.*, 33:139–146(7), 1981.
- [144] I. Odler and H. Köster. Investigation on the structure of fully hydrated Portland cement and tricalcium silicate pastes. III. Specific surface area and permeability. *Cem. Conc. Res.*, 21(6):975 – 982, 1991.
- [145] L. Cui and J. H. Cahyadi. Permeability and pore structure of C–S–H. *Cem. Conc. Res.*, 31:277–282, 2001.
- [146] Z. C. Grasley, G. W. Scherer, D. A. Lange, and J. J. Valenza. Dynamic pressurization method for measuring permeability and modulus: II. cementitious materials. *Mat. Struct.*, 40:711–721, 2007.
- [147] J. Tits, A. Jakob, E. Wieland, and P. Spieler. Diffusion of tritiated water and  $^{22}\text{Na}^+$  through non-degraded hardened cement pastes. *J. Contam. Hydrol.*, 61(1–4):45–62, 2003.
- [148] A. Delagrave, J. Marchand, and M. Pigeon. Influence of microstructure on the tritiated water diffusivity of mortars. *Adv. Cem. Based Mater.*, 7(2):60–65, 1998.
- [149] T. Yamaguchi, K. Negishi, S. Hoshino, and T. Tanaka. Modeling of diffusive mass transport in micropores in cement based materials. *Cem. Conc. Res.*, 39(12):1149–1155, 2009.
- [150] S. Numata, H. Amano, and K. Minami. Diffusion of tritiated water in cement materials. *J. Nucl. Mater.*, 171(2–3):373–380, 1990.
- [151] P. A. Monson and M. Rigby. Hard spherocylinder fluids: a Monte Carlo study. *Che. Phys. Lett.*, 58(1):122–126, 1978.
- [152] S. R. Williams and A. P. Philipse. Random packings of spheres and spherocylinders simulated by mechanical contraction. *Phys. Rev. E*, 67:051301, 2003.

- [153] J. Zhao, S. Li, R. Zou, and A. Yu. Dense random packings of spherocylinders. *Soft Matter*, 8:–, 2012.
- [154] I. N. Bronstein, K. A. Semendjajew, G. Musiol, and H. Mühlig. *Taschenbuch der Mathematik*. Verlag Harri Deutsch, 7 edition, 2008.
- [155] W. Man, A. Donev, F. H. Stillinger, M. T. Sullivan, W. B. Russel, D. Heeger, S. Inati, S. Torquato, and P. M. Chaikin. Experiments on random packings of ellipsoids. *Phys. Rev. Lett.*, 94:198001, 2005.
- [156] A. Donev, F. H. Stillinger, P. M. Chaikin, and S. Torquato. Unusually dense crystal packings of ellipsoids. *Phys. Rev. Lett.*, 92:255506, 2004.
- [157] I. Bitsanis, S. A. Somers, H. T. Davis, and M. Tirrel. Microscopic dynamics of flow in molecularly narrow pores. *J. Chem. Phys.*, 93(5):3427, 1990.
- [158] B. Rotenberg, V. Marry, N. Malikova, and P. Turq. Molecular simulation of aqueous solutions at clay surfaces. *J. Phys. Condens. Matter*, 22:1–8, 2010.
- [159] A. Botan, B. B. Rotenberg, V. Marry, P. Turq, and B. Noetinger. Hydrodynamics in clay nanopores. *J. Phys. Chem. C*, 115:16109–16115, 2011.
- [160] J. Neyman, editor. *A two-dimensional growth process*, volume IV Biology and problems of health of *Proceedings of the Fourth Berkely Symposium on Mathematical Statistics and Probability*, 1961.
- [161] T. Williams and R. Bjerknes. Stochastic model for abnormal clone spread through epithelial basal layer. *Nature*, 236:19–21, 1972.
- [162] T. A. Witten and L. M. Sander. Diffusion-limited aggregation, a kinetic critical phenomenon. *Phys. Rev. Lett.*, 47:1400–1403, 1981.
- [163] P. Meakin. The Vold-Sutherland and Eden models of cluster formation. *Journal of Colloid and Interface Science*, 96:415–424, 1983.
- [164] M. Avrami. Kinetics of phase change. I general theory. *J. Chem. Phys.*, 7(12):1103–1112, 1939.
- [165] A. Kolmogorov. A statistical theory for the recrystallization of metals. *Izv. Akad. Nauk SSR. Ser. Mat.*, (3):367–368, 1937.
- [166] F. Liu, F. Sommer, C. Bos, and E. J. Mittemeijer. Analysis of solid state phase transformation kinetics: models and recipes. *Int. Mater. Rev.*, 52(4):193–212, 2007.
- [167] I. H. Hillier. Modified Avrami equation for the bulk crystallization kinetics of spherulitic polymers. *J. Polym. Sci. A*, 3:3067–3078, 1965.
- [168] M. A. Etzold, P. J. McDonald, and A. F. Routh. Mesoscopic kinetic model for the formation and the morphology of calcium-silicate-hydrates in cement paste. *Cem. Conc. Res.*, 63:137–142, 2014.
- [169] R. Jullien and R. Botet. Scaling properties of the surface of the Eden model in  $d=2, 3, 4$ . *J. Phys. A-Math. Gen.*, 18(12):2279, 1985.

- [170] M. T. Batchelor and B. I. Henry. Limits to Eden growth in two and three dimensions. *Physics Letters A*, 157(4,5):229–236, 1991.
- [171] M. T. Batchelor and B. I. Henry. Diffusion-limited aggregation with Eden growth surface kinetics. *Physica A*, 203:566–582, 1994.
- [172] H.P. Peters, D. Stauffer, H. P. Höllers, and K. Loewenich. Radius, perimeter, and density profile for percolation clusters and lattice animals. *Z. Physik B*, 34:399–408, 1979.
- [173] F. Leyvraz. The 'active perimeter' in cluster growth models: a rigorous bound. *J. Phys. A-Math. Gen.*, 18(15):L941, 1985.
- [174] W. A. Johnson and R. F. Mehl. Reaction kinetics in processes of nucleation and growth. *Trans. AIME*, 135(12):416, 1939.
- [175] M. Avrami. Kinetics of phase change. II transformation-time relations for random distribution of nuclei. *J. Chem. Phys.*, 8:212–223, 1940.
- [176] J. W. Cahn. The time cone method for nucleation and growth kinetics on a finite domain. In *Symposium C – Thermodynamics and Kinetics of Phase Transformations*, volume 398 of *MRS Proceedings*, 1995.
- [177] E. Villa and P. R. Rios. Transformation kinetics for surface and bulk nucleation. *Acta Mater.*, 58:2752–2768, 2010.
- [178] J. Farjas and P. Roura. Numerical model of solid phase transformations governed by nucleation and growth: Microstructure development during isothermal crystallization. *Phys. Rev. B*, 75:184112, 2007.
- [179] E. Pineda and D. Crespo. Microstructure development in kolmogorov, johnson-mehl, and avrami nucleation and growth kinetics. *Phys. Rev. B*, 60:3104 – 3112, 1999.
- [180] M. P. Shepilov and D. S. Baik. Computer simulation of crystallization kinetics for the model with simultaneous nucleation of randomly-oriented ellipsoidal crystals. *J. Non.-Cryst. Solids*, 171:141–156, 1994.
- [181] T. Pusztai and L. Gránásy. Monte Carlo simulation of first-order phase transformations with mutual blocking of anisotropically growing particles up to all relevant orders. *Phys. Rev. B*, 57:14110–14117, 1998.
- [182] R. B. Godiksen, P. R. Rios, R. A. Vandermeer, S. Schmidt, and D. J. Jensen. Three-dimensional geometric simulations of random anisotropic growth during transformation phenomena. *Scripta Mater.*, 2008:279–282, 58.
- [183] B. J. Kooi. Extension of the Johnson-Mehl-Avrami-Kolmogorov theory incorporating anisotropic growth studied by Monte Carlo simulations. *Phys. Rev. B*, 73:054103–1 –13, 2006.
- [184] P. S. Dodds and J. S. Weitz. Packing limited growth of irregular objects. *Phys. Rev. E*, 67:016117, 2003.

- [185] S. A. Serebrinsky. Physical time scale in kinetic Monte Carlo simulations of continuous-time markov chains. *Phys. Rev. E*, 83:037701–1–3, 2011.
- [186] CGAL, Computational Geometry Algorithms Library. <http://www.cgal.org>.
- [187] M. E. Muller. A note on a method for generating points uniformly on n-dimensional spheres. *Commun. ACM*, 2(4):19–20, 1959. ISSN 0001-0782.
- [188] M. J. Laszlo. *Computational Geometry and Computer Graphics in C++*. Pearson Education, 1996.
- [189] C. Ericson. *Real Time Collision Detection*. CRC Press, 2004.
- [190] E. G. Gilbert, D. W. Johnson, and S. S. Keerthi. A fast procedure for computing the distance between complex objects in three-dimensional space. *IEEE T. Robot. Autom.*, 4(2):193–203, 1988.
- [191] R. A. Livingston. Fractal nucleation and growth model for the hydration of tricalcium silicate. *Cem. Conc. Res.*, 30(12):1853–1860, 2000.
- [192] E. Henderson and J.E. Bailey. Sheet-like structure of calcium silicate hydrates. *J. Mater. Sci.*, 23(2):501–508, 1988.
- [193] I.G. Richardson, J. Skibsted, L. Black, and R.J. Kirkpatrick. Characterisation of cement hydrate phases by TEM, NMR and Raman spectroscopy. *Adv. Cem. Res.*, 22: 233–248(15), 2010.
- [194] S. Brisard, R. S. Chae, I. Bihannic, L. Michot, P. Guttman, J. Thieme, G. Schneider, P. J. M. Monteiro, and Pierre Levitz. Morphological quantification of hierarchical geomaterials by x-ray nano-ct bridges the gap from nano to micro length scales. *Am. Mineral.*, 97(2-3):480–483, 2012.
- [195] A. Valori, V. Rodin, and P.J. McDonald. On the interpretation of 1h 2-dimensional {NMR} relaxation exchange spectra in cements: Is there exchange between pores with two characteristic sizes or fe<sup>3+</sup> concentrations? *Cem. Conc. Res.*, 40(9):1375 – 1377, 2010. ISSN 0008-8846. doi: <http://dx.doi.org/10.1016/j.cemconres.2010.03.022>. URL <http://www.sciencedirect.com/science/article/pii/S0008884610000918>.
- [196] M. Edén. Computer simulations in solid-state NMR. III. powder averaging. *Concept. Magn. Reson. A*, 18A:24–55, 2003.
- [197] M. M. Costoya Fernandez. *Effect of Particle Size on the Hydration Kinetics and Microstructural Development of Tricalcium Silicate*. PhD thesis, EPF Lausanne, 2008.
- [198] D. Winslow, J. M. Bukowski, and J. F. Young. The fractal arrangement of hydrated cement paste. *Cem. Conc. Res.*, 25(1):147–156, 1995.
- [199] H. S. Wong, M. Zobel, N. R. Buenfeld, and R. W. Zimmerman. Influence of the interfacial transition zone and microcracking on the diffusivity, permeability and sorptivity of cement-based materials after drying. *Mag. Concrete. Res.*, 61:571–589, 2009.
- [200] T. C. Powers, L. E. Copeland, J. C. Hayes, and H. M. Mann. Permeability of Portland cement paste. *J. Am. Concrete. I.*, 51:285, 1955.

- [201] M. B. Holness. The effect of crystallization time on plagioclase grain shape in dolerites. *Contrib. Mineral. Petr.*, 168(5), 2014.